PRACA DOKTORSKA

IChF
Institute of Physical Chemistry PAS

PhD Dissertation

Contrast enhancement in optical coherence angiography for brain imaging

Mounika Rapolu

IChF
Institute of Physical Chemistry PAS

PhD Thesis

Contrast enhancement in optical coherence angiography for brain imaging

Mounika Rapolu

Supervisor: Prof. dr hab. Maciej Wojtkowski

IChF
Institute of Physical Chemistry PAS

Thesis title: Contrast enhancement in optical coherence angiography for brain imaging

Author: Mounika Rapolu

Supervisor: Prof. dr hab. Maciej Wojtkowski

This dissertation was prepared within the International Doctoral Studies of the Institute of Physical Chemistry of the Polish Academy of Sciences in Warsaw, Kasprzaka 44/52, 01-224.

Warsaw, August 2021

Dedicated to my mom, Aruna and father, Chakradhar

and my late grandmother Kousalya

Acknowledgements

Many people have helped, directly or indirectly, to shape this thesis, and I personally want to acknowledge them for their contribution and support.

First, Prof. Maciej Wojtkowski, for giving me the opportunity to join the Physical optics and Biophotonics (POB) group to pursue a PhD degree and providing a very healthy work environment. He always supported my ideas being an excellent guide with great scientific discussions around the chalkboard, constant support, and mentorship althroughtout my during my PhD studies. I

I also thankful to Karol Karnowski, Dawid Borycki for navigating through a lot of unknowns and difficulties, technical or otherwise. I thank all the POB group memembers for their chats and discussions during the coeffe breaks made me refreshed.

I am incredibly debted to my parents, grandparents, aunt, uncle and cousins for all of their love and support throughtout my life. I chersish the memories I had during the PhD studies and I thankful to Arun, Idara, Sandhya, Ranju, Karthika, Ankita, Ganesh for the strong frienship, the laughter and memories we had. I specially thank to my friend Vineeth and grateful for being their for me in difficult times and he constantly encouraged, supported and motivated when I had low times. I also thank Anna pawlus and Anna jozewiskigo, for their support. My old friends Manju, Srivani, Sravya, Preeti, Sandhya and Vineesh who are far away, but were always their for me and thanks to whatsapp for it.

Special and heartful thanks to Paweł, Asia, Władysław, Iza, Marian, Tosia, Janek, Sławek, Adam and Patrycja for my found new home and made me feel like a family. I am indebted for their love and support throughout the PhD times. I really enjoyed the birthdays, summer, christamas, Easter, Barbeques and the holidays we spent together and I am glad that they became an integral part of my life. I am also thankful for the conferences that I had attended, which helped me connect my network of research intreset, meet peers in the field, had great dicussions and have chance to visit the nature around.

List of Publications

1. E. Auksorius, D. Borycki, P. Węgrzyn, B. Sikorski, I. Žičkienė, K. Liżewski, **M. Rapolu**, K. Adomavičius, S. Tomczewski and M. Wojtkowski "Spatio-temporal optical coherence tomography provides advanced imaging of the human retina and choroid", submitted to Nature medicine (2021) (Reference no. : NMED-A113115).

2. **M. Rapolu**, D. Borycki, K. Karol, and M. Wojtkowski "Bessel and Gaussian beam optical coherence microscopy angiography for in-vivo cerebrovascular imaging", under submission for Journal of Biomedical Optics (2021).

3. **M. Rapolu**, K. Karol, D. Borycki, and M. Wojtkowski "Contrast enhancement for in-vivo brain imaging using optical coherence microscopy angiography", under preparation for Journal of optics (2021).

4. **M. Rapolu**, H. Dolezyczek, P. Niedźwiedziuk, D. Borycki, M. Malinowska, G. Wilczynski and M. Wojtkowski, "Longitudinal in-vivo OCM imaging of glioblastoma development in mouse brain" Biomedical Optics Express 11, 5003-5016 (2020) https://doi.org/10.1364/BOE.400723

5. **M. Rapolu**, P. Niedźwiedziuk, D. Borycki, P. Wnuk and M. Wojtkowski,"Enhancing microvasculature maps for Optical Coherence Tomography Angiography (OCT-A)" in Photonics Letters of Poland, VOL.10 (3), 61-63 (2018) https://doi: 10.4302/plp.v10i3.841

6. **M. Rapolu**, H. Dolezyczek, S. Tamborski, M. Malinowska, G. Wilczynski, M. Szkulmowski, and M. Wojtkowski, "Bessel Beam OCM for analysis of Global Ischemia in Mouse Brain," in Optical Coherence Imaging Techniques and Imaging in Scattering Media II, M. Wojtkowski, ed., Vol. 10416 of SPIE Proceedings (Optical Society of America, 2017), paper 1041609 https://doi.org/10.1117/12.2287740

Oral Presentations and Posters

Oral presentation:

1. Oral presentation on "Potential advantages and disadvantages of contrast enhancement in OCT using large gold nanorods and intralipids for in-vivo longitudinal imaging of mouse brain" at **Photonics Asia, Digital Forum, China** in October 2020.

2. Oral presentation on "Effect of contrast agents and enhancement of cerebrovascular on mouse brain microvasculature studies using 800 nm Gaussian and Polarization sensitive (PS) OCT system" at **SPIE Photonics West, San Francisco, USA** in February 2020.

3. Oral presentation on "Longitudinal growth and progression studies of in-vivo mouse brain Glioblastoma (GBM) tumour microvasculature using OCT" at **Photonics Asia, Hangzhou, China** in October 2019.

4. Oral presentation on "In-vivo longitudinal imaging of glioblastoma (GBM) tumor in mouse brain microvasculature using 800nm OCT system" at **Be-Optical Final conference** at Max Planck Institute for Dynamics and Self-Organization in August 2019, **Göttingen, Germany.**

5. Oral presentation on "Imaging of cortical vessels of mouse brain: Bessel vs Gaussian beams" at **EOS Biennial Meeting (EOSAM) Delft, the Netherlands** in October 2018.

6. Oral Presentation on "Bessel Beam OCM for analysis of Global Ischemia in Mouse Brain" at **European Conferences on Biomedical Optics ECBO at Munich, Germany** in June 2017.

Poster presentation:

7. Poster presentation on "Contrast enhancement in optical coherence angiography for brain imaging" at **The Siegman International School on Lasers, University of Rochester**, New York, United States in August 2019.

8. Poster on "Glioblastoma (GBM) tumor of mouse brain microvasculature studies using OCT and enhancement of cerebrovascular with contrast agents using 800nm and 1300nm OCT system" at **The European Conferences on Biomedical Optics (ECBO), Munich, Germany** in July 2019.

9. Poster presentation for "Multifractal, Fractal and Lacunarity analysis of the three-dimensional cerebral vasculature of the mouse brain in vivo" at **Fractal Geometry and Stochastics 6 (FGS 6), Bad Herrenalb (Black Forest), Germany** in September 2018.

10. Poster presentation on "Enhanced Image processing of OCT data for Global Ischemia and Glioblastoma" at **VII International Conference on Speckle Metrology – SPECKLE at Janów Podlaski**, Poland in September 2018.

Abstract

Monitoring of treatments of brain traumas and brain diseases requires continuous control of quantitative parameters describing the state of rodent brain vascularization. The introduction of new biomarkers allowing objective evaluation of progression or regression of development of new pathological vessels or atrophy of existing vessels requires to optimize imaging conditions. In particular, it is important to achieve high contrast for all capillaries located throughout the sub-cranial layer. The contrast improvement in angiographic imaging of the rodent brain vasculature in the presence of pathological changes by Optical Coherence Microscopy (OCM) can be accomplished by varying the physical experimental conditions affecting any of parameters such as: amplitude of light scattered from blood, geometry of illuminating beam, timing and settings of raster scan. The Bessel beam OCM promises to overcome the problem of the penetration depth and offers better extended focus to be applied to image the turbid tissue medium. It is a potential candidate in providing the information of the dynamics of blood circulation and gives a better new perspective for the monitoring the key parameter in activation of these stroke in brain in pathophysiological pathway. We introduced a system based on a Bessel beam and performed a comparison with a classical system illuminating the sample with a Gaussian beam. We have analyzed the advantages and disadvantages of this solution for a very specific application - to brain imaging by Optical Coherence Microscopy Angiography (OCM-A).

The contrast agents like intralipids or Large Gold Nanorods (LGNRs) are used to increase the imaging sensitivity for ex-vivo and in-vivo studies. They help to increase the contrast of the OCM signal and observe fine details in the deeper regions within intact tissue. But there are only quite a few groups working on LGNRs for biomedical studies despite their advantage of increasing the contrast of the OCM signal. We studied whether the introduction of nanoparticles enhance the infrared scattering using plasmon resonance enables OCM-A signal enhancement. We also studied if the introduction of nontoxic scattering enhancement agent intralipids in blood to improve the OCM-A contrast.

Finally, we evaluated the impact of proper selection of OCM-A scanning protocols on the quality of angiographic imaging in the presence of lesions and proposed a new method to improve the OCM-A contrast without contrast agents.

Contents

List of Figures

Acknowledgements

Many people have helped, directly or indirectly, to shape this thesis, and I personally want to acknowledge them for their contribution and support.

First, Prof. Maciej Wojtkowski, for giving me the opportunity to join the Physical optics and Biophotonics (POB) group to pursue a PhD degree to capitalise on my experience. Thanks David for mentoring me, providing and leading an excellent research facility, with high-profile international collaborations and a very healthy work environment that promotes work-life balance. I also feel very grateful to my other supervisors, Karol Karnowski, Dawid Borycki, and, who have taught me a great deal of knowledge and helped me manage this research project effectively, navigating through a lot of unknowns and difficulties, technical or otherwise. I am also very thankful to the CREATE and MAESTRO for supporting me through an scholarship.

I am incredibly debted to my late grandmother, for all her love and support throughtout my life. I chersish the memories and I thankful to Arun, Idara, Sandhya, Ranju, Karthika, Ankita , Ganesh for the strong frienship, memories and for supporting me during difficult times,

KAIST - Wangyuhl Oh, Shin Paul

Nencki - Hubert, Monika malinowska

POB - Paulina,

Paulina, Ranju, Idara, Karthika, Arun,

Vineeth supported me in difficult times, encourgaed me

Anna pawlus, Anna jozewiskigo, Anna Salamończyk,

Manju, Srivani, Sandhya, Vineesh,

Special thanks to Paweł, Asia, Władysław, Iza, Marian, Tosia, Janek, Sławek, Adam and Patrycja my found new home and made me feel like a family. I am indebted for their love and support I really enjoyed the birthdays, summer, christamas, Easter, Barbeques and holidays and they became an integral part of my life. It helped me connect my work with the places and nature around me through countless and beautiful examples of the ubiquity of the topics being studied in this thesis. These awe-inspiring optical and physical phenomena might take a different form from those researched, but they are all related: light scattering by the west coast

pristine sky in enchanting sunsets, refraction by water droplets in Perth's winter rainbows, reduced visibility by stormy and foggy clouds over the river, wave interference patterns in Freshwater bay, summer light attenuation by sunscreen at Floreat Beach.

My professional development and research creativity have greatly benefitted from in-depth discussions and guidance by colleagues and high-calibre researchers Timothy Hillman, Brendan Kennedy, Maciej Wojtkowski and Martin Villiger. Without their input and our exchange of ideas, the richness of this research would have suffered.

I want to thank for having been, not only peers providing the biggest continuing support and having shared their research experience with me, but also for being true friends.

Other colleagues and fellow PhD candidates have been a source of knowledge and inspiration throughout the duration of this research: Bryden with his fearless "can do" attitude, Philip with his humbleness and wit, Kelsey with her positive work ethics, Lixin with his competence and diligence, Robert with his focus and drive and the rest of the team and collaborators with their unique characteristics.

I cannot forget the moral support and keen interest from Cibele in my research and my career development, which strengthened my confidence in the pursuit of this achievement. Roberta, Laurent, Monica, Seon, Danila, Uros, Cris, Valerio and Jana, you are all good friends and I am fortunate to have you in my life, and I am sure you are all delighted by this accomplishment. Through your smiles, our laughs and the good times together, you have helped me strike the right balance, and tackle the intricacies of research with a positive attitude. Thanks to my housemates and friends, especially Kat, Lana, Dario and Jon who have been supportive and understanding at all times.

Thanks to all the SPIE and OSA student chapter for having created something fun and valuable in warsaw for the young and upcoming optics and photonics community, through professional development and scientific outreach efforts.

Mens sana in corpore sano. A very true Latin statement, and for me a healthy body comes from the sporting activity that I enjoy the most: volleyball. So thanks to all my volleyball and beach volleyball mates.

Heather and Chris, you have been like family to me here in Perth. From the very beginning, you helped me settle in the very best of ways, and I will always be grateful to you for that and the warmth you gave me.

Last, but not least, thanks to my friends and family back home in Italy. Thanks to Francesca, Chino and Andrea. Your affection has travelled through continents. Grazie to my close relatives, my cousins, my late grandparents, my brother Marco and my parents Lucia and Roberto. Your unconditional encouragement and love has provided, at the same time, a safe haven to reflect upon my values and interests, and a springboard that strengthened my motivation to look ahead and to reach new grounds.

Chapter 1 Introduction

1.1 Brain imaging highlighting blood vessels

Brain the most important delicate, sophisticated, highly perfused complex organ and the centre of the nervous system (CNS), with billions of cells interlinked through trillions of neuronal connections [1]. It is the primary organ that controls all the essential biological and primary functions in the body. In most vertebrates, the brain vasculature made of endothelial cells and mural cells composed of large vessels and small vessels or capillaries. The blood vessels transmit oxygen and nutrients to the whole body and are responsible for the normal function of glial cells in the brain and neurons [2-4]. They are tightly organized in the brain and support the blood-brain barrier (BBB) between the brain tissue and blood. The brain vasculature consists of an arterial input (arteries), an intervening capillary, and also a venous drainage system (veins) which play an essential role in carrying the blood [4-6]. The CNS does not have lymphatic vessels. The alterations of any vascular structure in the brain could lead to brain pathologies such as a tumor, stroke, and other neurological disorders [4, 7, 8]. The preclinical imaging studies allow bridging the translational gap between small animal studies and human research. The assessment of the brain's morphological, functional, and structural anatomy could potentially unravel the understanding of brain function and different pathological conditions. The microvasculature information, such as blood flow and vascular network, is an indicator of the progression or onset of various brain diseases. The in-vivo brain studies of the small animal models developed recently provides valuable insights and assist with the potential to translate for human therapies [9]. The Figure 1 represents the different regions of the human brain such a dura mater, arachnoid mater, and pia mater of the upper regions of the brain. Whereas the lower regions of the brain such as thalamus, hypothalamus, pituitary gland, corpus collasum, cerebellum, medulla, pons, and brain stem are represented.

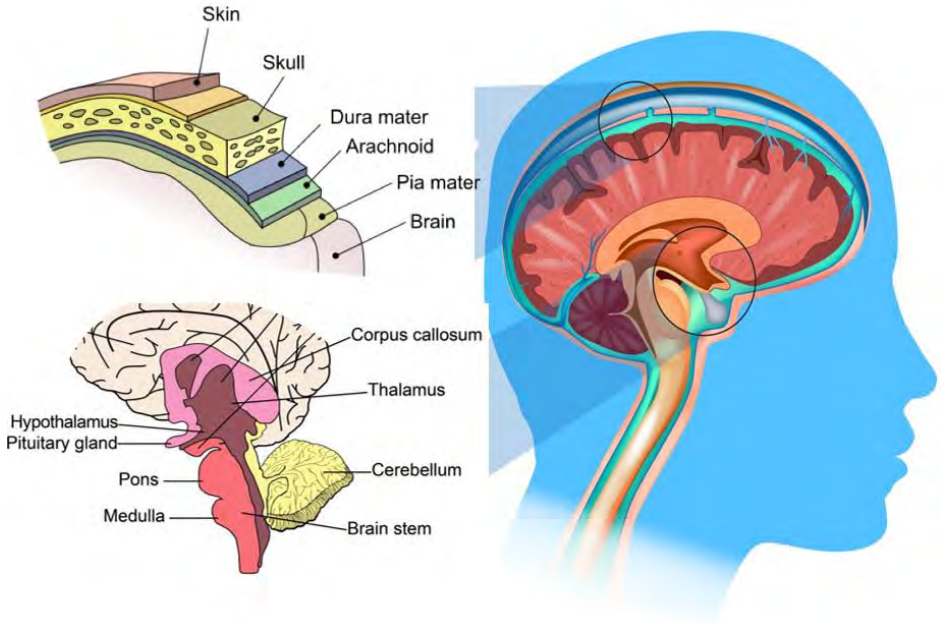

Figure 0-1 The different regions represented in the human brain. Copied from from Sakurra / Getty Images

1.2 Brain imaging technologies with a cranial window

The main blood vessel system supplying the brain is located subcranially and was isolated by the meningeal layers. The removal of the dura affects the biological process and disrupts the brain's natural physiological and metabolic mechanisms. The major advances in in-vivo real-time brain imaging were through the development of cranial window imaging [10-12]. This technique provides an insight into cytoarchitecture and has no wound manipulation as only the skin was removed from the brain. The cranial window implantation has overcome the limitations of imaging resolution and depth in optical technologies to a certain extent and has opened up a new exciting area for in-vivo imaging of the brain research [13]. This method provides the possible conditions to have a natural biological environment that does not interfere with brain function [13]. It also allows visualizing, evaluating, and tracking the changes in cerebral microvascular response to various pathologies, treatments, and longitudinal studies [13-26]. The cranial window imaging was applied for in-vivo brain imaging with two-photon laser scanning microscopy [13, 21], near-infrared spectroscopy (NIR) [27], intravital microscopy [21], optical intrinsic imaging [11, 25, 27, 28]. The NIR lacks sufficient spatial resolution and whereas the optical intrinsic imaging signal suffers from poor depth resolving capability. The other modalities among these have a disadvantage of using external contrast agents such as dye for imaging. The multiphoton microscopy (MPM): two-photon (2P) microscopy and 3-photon (3P) microscopy were also used for cranial window imaging [29-41]. The application of 2P microscopy for cranial window in-vivo brain imaging facilitates a high

clarity and has optical access to provide deep brain structures (500–700 μm). Nevertheless, it has a small field of view (<1 mm) [42-44] making it less attractive for brain imaging. The development of new imaging technologies such as 3P microscopy has achieved an imaging depth of around 600-1000 μm using a transcranial window and a glass coverslip [40, 41, 45, 46]. However, the disadvantage of the MPM techniques is that it demands either the transgenic mouse models or the external contrast agents for imaging [38]. The chronic optical access after transcranial window implantation for the longitudinal imaging of the mouse brain can be extended from 90 days to > 300 days [47, 48]. This period could vary and depend on opacification, thickening, and regrowth of the dura matter around the craniectomy region [11, 13, 49, 50].

1.3 OCT and OCM for structural brain imaging

Optical coherence tomography (OCT) is an optical imaging technique capable of providing structural information of the biological tissue and is extensively used in the clinical, diagnostic, and biomedical imaging fields [51]. Clinical evaluation of this technology is still in the early stages for human brain imaging. However, most of the published results point to a promising future through continued improvements in technology, algorithms and signal analysis enhancements [52-54]. Several other modalities are available for in-vivo imaging that are able to penetrate through the skull, including computed tomography (CT), magnetic resonance (MRI) and positron emission tomography (PET) [55]. However, they still lack the spatial resolution for the in-vivo analysis in scale of micrometer resolution scale events. The OCT uses interferometry to achieve high resolution, axial sectioning based on the principle of capturing time of flight of photons [56]. It occupies a niche in terms of reaching optimal balance between imaging resolution and imaging depth. The first reports of brain morphology in animal models using OCT are in Xenopus laevis to study organ development [57, 58]. The anatomical features of rodent brain such as pyramidal cell bodies, individual axons, and the laminar architecture of cerebral cortical layers were revealed by in-vivo OCT imaging after reducing the speckle noise [59-62]. The conventional time domain (TD-OCT) can only produce structural images and aid the visualization of anatomical changes. The Fourier-domain or spectral domain OCT (SD-OCT) can be used to obtain the depth-resolved information of the capillary velocity mapping for the cerebral regions [63, 64]. The label-free in-vivo neuroimaging and the tumour margin detection was achieved using speckle-modulating OCT (SM-OCT) [59]. Whereas the time-domain full-field OCT (FF-OCT) is used for the signal contrast enhancement to visualise the

cellular and subcellular structures in the excised brain tissue [65, 66]. The advancements in swept-source OCT (SS-OCT) enabled the detection of brain tumour margins [67-71]. The white and grey matter are differentiated using the attenuation coefficient of the light emitted from the brain tissue and provided with a contrast similar to Nissl staining [72]. Moreover, many tools are used to differentiate the various structures in brain tissue and obtain functional information [73-77]. The optical coherence microscopy angiography (OCM-A) is an extension of OCT when a high numerical aperture is used in the sample or the imaging arm to obtain high-resolution images of the vasculature. It uses postprocessing algorithms and scanning protocols to obtain the microvasculature information [53]. It allows the identification of microvascular abnormalities using intrinsic contrast. OCM-A is a preferable tool for brain imaging in mice.

1.4 Angiography by OCM for brain imaging

The likelihood of successful detecting, monitoring, and treating the disease at various stages is related to the detection of changes in the microcirculation. The dynamic change in light scattering when the light passes through the turbid medium yields the contrast. The potential of OCM-A to visualize the microcirculation without exogenous contrast agents has been recognized and progressed in different branches of physics, biomedical and clinical research over the past decade. This has resulted in extensive applications, especially in the field of ophthalmology [78-84] and other fields like developmental biology [85-88], gastroenterology [89-91], neuroscience [18, 19, 92-95], and tumour biology [96-99].

From the optical viewpoint, the brain is a highly scattering medium with a relatively homogeneous distribution of the refractive index $n(r)$. The anatomical details of the brain structure do not differentiate well when the source of contrast is a change in refractive index n. Fortunately, moving erythrocytes located in blood vessels can be differentiated and separated from the static tissue of the other brain layers using OCM-A. Thus, the OCM-A can also enhance the contour of blood vessels and visualize the entire 3-D vascular system on the brain surface [100-102]. The quantitative and qualitative information can be obtained from OCM-A data. Although OCM-A was widely recognized as a qualitative method with a wide range of applications in basic, clinical, diagnostic, and biomedical sciences to visualize the lumen perfusion of blood vessels [103]. There is sporadic work pointing to the quantitative aspect in OCM-A analyses [104-106]. OCM-A has satisfied the need to identify pathological microvascular changes such as angiogenesis, neovascularization, ischemia, changes in capillary morphology, and other biological functional abnormalities in the brain [53, 75]. It can

differentiate the tissue layers and morphological abnormalities of the vascular system caused by disease [81, 107]. It also helps to monitor the morphological, structural, and perfusion changes of the cerebral microvasculature over a period of time [101, 108]. The OCM-A was used for the extensive studies of the brain imaging of the laminar structure of the isocortex [72], visualizing the cerebral cortex [109], single myelin fibres [110], neuronal cell bodies [111, 112], and the tumorous tissue [66]. The polarization-sensitive OCT (PS-OCT) was employed to quantify and map the myelinated fibres with a high microscopic resolution [73, 113-115]. The wide-field OCM was used to reconstruct a single brain image for delineating fibre tracts [62]. The microvasculature obtained from OCM-A plays a vital role in understanding and monitoring many disease progressions such as tumour growth, stroke, and other pathological conditions. The potential use of OCT during tumour resection as guidance [67, 69, 116, 117] and the study of neurological disorders are demonstrated [118-120]. The integration of OCT into surgical microscopes allows its advantage for intraoperative use in neurosurgery [69, 117] and microneurosurgery [116, 121, 122]. The hemodynamic, vascular, and other changes in the 3D maps of the brain microvasculature during stroke were studied using OCT-A [18, 123-125]. The ability of OCM with angiography to determine both structural and functional changes in the brain may provide insights into cytoarchitecture. It also provides with a new perspective in better understanding the pathogenesis of disorders, biological processes, neuronal, cognitive functions and brain tumours. The sensitivity of OCM-A being able to obtain more hemodynamic information encourages to detect the disease at an early stage.

1.5 Bessel and Gauss for OCM-A

OCM-A works well for the most superficial vessels, but imaging in deeper layers is hindered by stronger scattering from static tissue, resulting in loss of imaging contrast [126]. In addition, the observation of small vessels requires high magnification, but in the scanning systems such as OCM the tight focusing of high numerical objective
(NA) objectives results in a rapid loss of lateral resolution at different depths in the specimen [127]. Both effects are particularly evident in imaging structural changes in the brain, such as tumours or haemorrhages, because new tissue or fibrotic changes present increase scattering. The modification of the imaging method is one solution to address this problem that can be achieved using an axicon lens to generate the Bessel beam to increase the depth of focus (DOF) [126, 128]. Due to the increased scattering properties with depth in the turbid tissue medium, it is difficult to achieve uniform image contrast in deeper tissue regions. To resolve this problem,

Ding et al. investigated the use of an axicon lens by generating a Bessel beam for the first time in the time-domain OCT in 2002 [126]. The first application of this self-healing, self-reconstructing, self-diffracting properties [129, 130] of Bessel beam with a tighter spot size at focus have expanded the potential and capability of OCT, but it is applied for microscopy imaging in 2010 [131, 132]. In this way, the beam illuminating the sample at the focal point was shaped to maintain high lateral resolution at depths ten times greater than when using classical gaussian illumination [133]. However, the advantage and efficiency of Bessel beam over Gaussian beam for OCT imaging has continued to be debated in the scientific community over the past few years [132-134]. There are very few studies on the effect of image quality for both beams on the ex-vivo samples [134, 135]. However, presently, there are no available studies to compare the feasibility of both beams especially for longitudinal in-vivo brain imaging.

1.6 Contrast enhacement in OCM-A

The contrast agents are used to enhance the scattering coefficient of the tissue and thereby significantly increases the signal-to-noise ratio (SNR), advancing the development of OCM -A to expand its application [136]. The addition of contrast agents in OCM-A could potentially have the advantage of increasing sensitivity and resolution to target the specific region or cell types and have an extended capability for cellular and molecular imaging [59, 137-143]. They are an excellent tool for brain imaging, particularly for improving the microvascular imaging, diagnosis, and study of the tumour [144], investigating the leukocytes [145], and disease progression. Several synthetic particles such as gold nanorods (GNR's), plasmonic nanoparticles, and large gold nanorods (LGNR's) have been used recently as exogenous contrast agents and were considered as a potential for brain imaging [138, 146-152]. These contrast agents allow OCM-A to label, visualize and study the specific pathological conditions within the biological tissue medium [153-157]. They can also be bio-functionalized with different functional groups and bind to the tissue's target-specific molecules or pathological sites. The bio-functionalization could improve the advantage for accurate microvascular detection, longitudinal studies, and study of response to the treatment [98, 138, 141, 158, 159]. The contrast-enhanced OCM-A can reveal the deeper microvasculature in the tumor ($\geq 1\,mm$ below surface of the skin) which could not be detected with a conventional OCT through injection of LGNR's as intravascular contrast agents [138]. The LGNR's demonstrate 110-fold greater signal per particle than conventional GNRs and detect the individual cells in the blood

in-vivo [160]. The enhancement of lymphatic structures and the segmentation of peritumoral lymphatic networks was achieved by subcutaneous injection of contrast agents [98]. The LGNR's were used in contrast-enhanced speckle modulating OCT (SM-OCT) for longitudinal imaging of the leukocytes and detection of brain tumour margin in the orthotopic glioblastoma multiforme (GBM) mouse model [159]. However, they still lack the quantification, and furthermore, the longitudinal imaging has been performed only for two days. There is no available literature to know the potential of contrast agents for longitudinal in-vivo brain imaging studies.

The intralipids are the highly scattering and slightly less invasive method used recently to enhance the contrast in OCT for the mouse cerebral imaging studies [88, 108, 161-165]. The intravascular signal from OCT vasculature, parallel to beam axis is enhanced with the injection of intralipids, and thereby the visibility is improved [166, 167]. They can improve the OCT signal intensity, angiography and act as plasma tracer [162, 166, 168]. The intravenous injection of intralipid has a constant scattering temporally in the vessels, including the capillaries, thereby increasing the contrast in the angiography signal.

Although the use of the functional materials and intralipids as contrast agents could yield high contrast and high resolution of the microvasculature images in the OCT, their interference with the natural biological mechanisms increases the invasiveness of the imaging. They can also affect the physiology, constrain the imaging conditions (the source wavelength must match the contrast agent's absorption spectrum, limit the penetration depth), and have an adverse effect on the cellular process for longitudinal imaging studies. Their requirement for tight focal volumes reduces the total acquisition time and demands for extensive controlled experiments [161]. Therefore, it is important to rationally evaluate the advantages of using contrast agents and compare them to other less invasive techniques for contrast-enhanced angiographic imaging.

1.7 Aim of disertation

Monitoring of treatments of brain traumas and brain diseases requires continuous control of quantitative parameters describing the state of rodent brain vascularization. The introduction of new biomarkers allowing objective evaluation of progression or regression of development of new pathological vessels or atrophy of existing vessels requires to optimize imaging conditions. In particular, it is important to achieve high contrast for all capillaries located throughout the sub-cranial layer. The contrast improvement in angiographic imaging of the rodent brain

vasculature in the presence of pathological changes by OCM can be accomplished by varying the physical experimental conditions affecting any of parameters such as: amplitude of light scattered from blood, geometry of illuminating beam, timing and settings of raster scan. The Bessel beam OCM promises to overcome the problem of the penetration depth and offers better extended focus to be applied to image the turbid tissue medium. It is a potential candidate in providing the information of the dynamics of blood circulation and gives a better new perspective for the monitoring the key parameter in activation of these stroke in brain in pathophysiological pathway. We introduced a system based on a Bessel beam and performed a comparison with a classical system illuminating the sample with a Gaussian beam. We have analyzed the advantages and disadvantages of this solution for a very specific application - to brain imaging by OCM-A.

The contrast agents like intralipids, LGNRs are used to increase the imaging sensitivity for ex-vivo and in-vivo studies. They help to increase the contrast of the OCM signal and observe fine details in the deeper regions within intact tissue. But there are only quite a few groups working on LGNRs for biomedical studies despite their advantage of increasing the contrast of the OCM signal. We studied whether the introduction of nanoparticles enhance the infrared scattering using plasmon resonance enables OCM-A signal enhancement. We also studied if the introduction of nontoxic scattering enhancement agent intralipids in blood to improve the OCM-A contrast. They are the most widely used contrast agents in the clinical imaging.

Finally, we evaluated the impact of proper selection of OCM-A scanning protocol on the quality of angiographic imaging in the presence of lesions and proposed a new method to improve the OCM-A contrast without contrast agents.

The thesis of this work is following:

Introduction of new biomarkers in angiographic imaging of the rodent brain vasculature in the presence of pathological changes by optical coherence microscopy (OCM) can be accomplished by varying the physical experimental conditions affecting any of the following parameters:

1. **amplitude of light scattered from blood;**
2. **geometry of illuminating beam;**
3. **timing and settings of raster scan.**

The specific scientific questions to be addressed are defined as follows:

1. Whether the introduction of nanoparticles to enhance infrared scattering using plasmon resonance enables Angio-OCT signal enhancement?
2. Does the introduction of nontoxic scattering enhancement agents in blood help improve OCM-A contrast?
3. Does the introduction of Bessel beam illumination improve vascular visibility on OCM-A in the presence of lesions?
4. What is the impact of proper selection of OCM-A scanning protocol on the quality of angiographic imaging in the presence of lesions?

Chapter 2 Theory: Optical Coherence Microscopy -Angiography

2.1 Optical Coherence Microscopy (OCM)

Optical coherence tomography (OCT) is an imaging technique based on low coherence interferometry that enables non-invasive, non-contact, high-speed, and three-dimensional (3D) imaging of the biological specimen with a micrometer ranging axial and longitudinal resolutions. If the imaging system uses a high numerical aperture objective, such a system is defined as optical coherence microscopy (OCM) [169, 170]. For both systems, the information within the sample's internal structure is obtained from the interference fringes if the sample moderately absorbs and back-scatters the light from the sample [171, 172]. The principle of OCM is analogous to ultrasound, and here the probe beam is a back-scattered lightwave instead of the sound wave [173]. The essential components of an OCM are an optical light source, a Michelson or Mach-Zender interferometer, a detector to measure the amplitude of spectral fringes, an acquisition system, and signal processing algorithms to extract image information by measuring the optical path delay of reflected light in respect to the position of the reference mirror [174]. Thus, it is possible to attain a high resolution (2-7 μm for the direction parallel to the incident beam, and 6-20 μm for the direction transverse to the incident beam), which is much higher than the ultrasound method. However, due to light-matter interaction, the signal weakens with depth due to the absorption and scattering process, limiting the penetration depth up to 1-3 mm for near infrared radiation (NIR~ 700-1300nm). The sum of the backscattered light fields scattered by particles at a given lateral and depth position in the coherence volume was referred to as the OCM signal [175]. The inverse scattering theorem was used to confer the framework and obtain the analysis of the OCM signal [176]. In the Fourier domain OCM approach, the A-scan signal was retrieved from the spectral analysis of the interferometric signal measured as a function of intensity of spectral fringes and wavenumber k [177]. The reference mirror is not scanned axially in this approach, and the back-scattered light interface with a path difference Δz_s , reflectivity ρ_i , and wavenumber k the interference signal is given by:

$$\boldsymbol{I_{OCM}(k, \Delta z_s)} = I_s(k) + I_r(k) + 2\sqrt{I_s(k) I_r(k)}\, cos(2\Delta z_s k)\,, \qquad \textbf{2.1}$$

where $I_s(k) \sim \rho_s(k)\eta_s(k)I_0(k)$ is the measured intensity of the light spectrum for the sample, $I_r(k) \sim \rho_r(k)\eta_r(k)I_0(k)$ is the measured intensity of the reference spectrum,

$\rho_s(k)$ and $\rho_r(k)$ are the mirror/sample reflectivities of the sample and reference spectrum, respectively and,

$\eta_s(k)$ and $\eta_r(k)$ are the detection efficiencies of the sample and reference spectrum, respectively.

Eq. (2.1) represents that the sum of $I_s(k)$ and $I_r(k)$ is topped by a cosine function modulation, and its frequency is proportional to $2\Delta z_s$. The intensity across the spectrum of this modulation is proportional to the intensity of the reference spectrum, $I_r(k)$ and strength of the back-scattered light signal from the sample interface, $I_s(k)$. It shows that interferometric detection can enhance the signal from the weak sample by a strong signal from the reference arm. The depth profile or A-scan can be retrieved from Eq. (2.1) by an inverse Fourier transformation and can be rewritten as [176, 178]:

$$\boldsymbol{r(\Delta z_s) = \left|\mathcal{F}^{-1}_{k\to z}[I(k,\Delta z_s)]\right|,} \qquad \textbf{2.2}$$

where $\Gamma(\Delta z_s)$ is the coherence function envelope with several back-scattered signals from the sample interfaces $\Delta z_i \in \{\Delta z_1, \Delta z_2, \ldots\ldots \Delta z_N\}$ located at N depths. The observed total intensity is the result of the superposition of all signals $I(k, \Delta z_i)$ and given by [177]:

$$\boldsymbol{I_{total}(k) = I_s(k) + I_r(k) + \sqrt{I_r(k)}\sum_{i=1}^{N}\sqrt{I_i(k)}\,cos(2\Delta z_s k),} \qquad \textbf{2.3}$$

where $I_s(k) = \sum_{i=1}^{N} I_i(k)$ and the case similar to Eq. (2.1) and Eq. (2.2) of the single back-reflected light.

2.2 Optical Coherence Microscopy - Angiography (OCM-A)

The optical coherence microscopy angiography (OCM-A) is a functional extension of OCM, where repeated B-scans were used to detect the motion contrast and visualize the microvasculature. The additional capability of the OCM provides a detailed assessment of both structural and functional information of microvasculature networks using both intensity and phase information along with other post-processing angiography algorithms. This information enables the volumetric visualization of the blood flow by tracking the motion of the red blood cells (RBCs) without contrast agents [82, 93, 95, 179, 180]. Such motion of the RBCs in the blood vessel produces dynamic signals over time, whereas the static tissue produces only a

constant reflection. The consecutive B-scans with both signals are subtracted from each other to obtain only the signal corresponding only dynamic motion of erythrocytes in the tissue [127]. These signals were encoded as light and dark pixels for dynamic blood flow and static tissue. The angiography algorithms were used to capture and visualize the blood vessel's anatomy, such as the arteries, veins, and capillaries. They use the variation in intensity or amplitude [181-184], phase [56, 98, 185, 186], or the complex value [99, 100, 187-189] of the OCM signal. In contrast to doppler OCM methods, OCM-A techniques are independent of the orientation of blood vessels [190, 191].

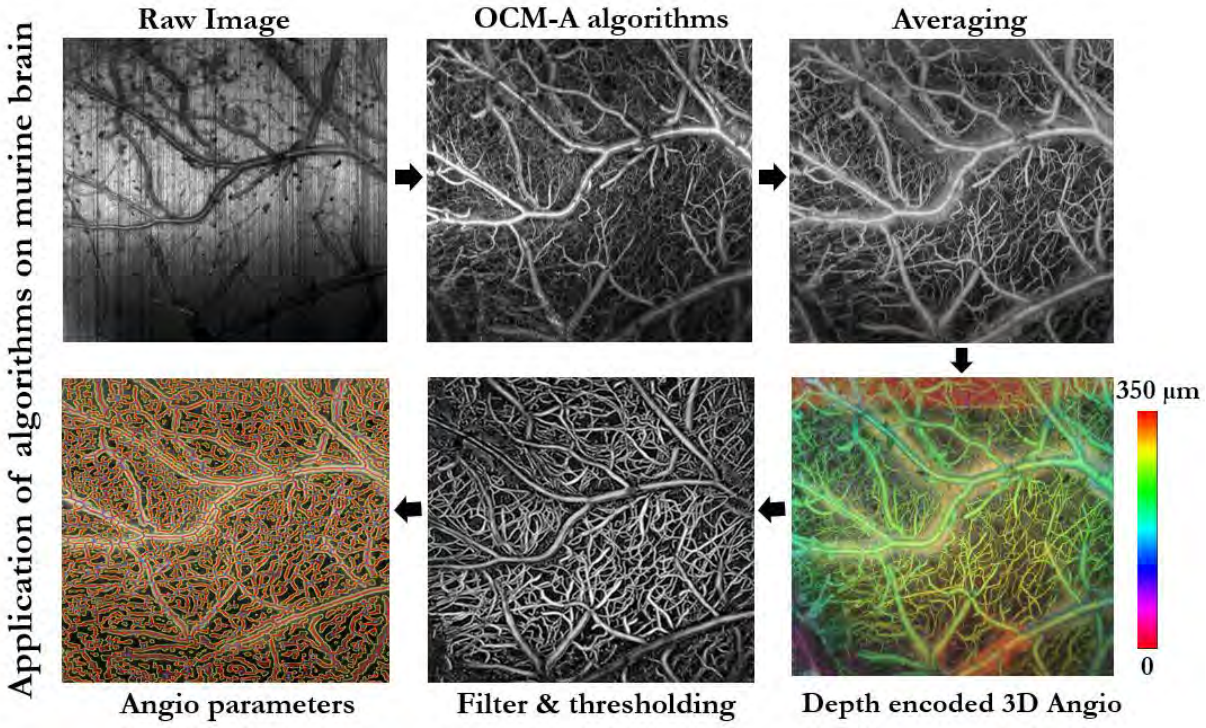

Figure 2-1 Steps of post-processing algorithms applied for mouse brain to achieve enhanced visualization of the cerebral microvasculature

The flow motion contrast requires collecting multiple A-scans or B-scans when registered at the same spatial position. The family of OCM-A methods that enables the microvasculature visualization include: intensity decorrelation [182], amplitude and intensity analysis [93, 185, 192], phase variance (circular) [98, 193], variance of phase shifts [194], absolute complex difference [93], speckle variance methods [184, 195-197], optical microangiography (OMAG) [198], spatial tomogram filtration [199], dual-beam scanning [200-202]. However, each method has a trade-off regarding noise levels, imaging speed, the field of view (FOV), microvascular visualization, and artefacts while imaging the biological tissue. There are important post-processing steps to achieve the microvasculature visualization: angiography algorithms, bulk

motion suppression or correction, and averaging algorithm applied for the murine brain imaging shown in Figure 2-1.

2.3 OCM-A algorithms for cerebral vasculature

The four efficient OCM-A algorithms that give reasonable sensitivity for detection of the flow motion contrast with minimal number of B-scans for visualization of the small capillaries inbrain imaging are: absolute intensity difference [93, 192], the absolute complex difference [93], phase variance [98, 193], and speckle variance [184]. These methods are also resistant to bulk motion and computational complexity by reducing the total acquisition time. These methods can be iteratively applied to achieve an entire three-dimensional (3D) angiographic data set. The absolute intensity difference and speckle variance are intensity-based algorithms. The phase variance and absolute complex difference are phase-sensitive algorithms, thus requiring more complex analysis than the intensity-based methods [203]. In each case, the N complex-valued OCM signals $S(x, y, z)$ are acquired from the consecutive B-scans (oversampled) to calculate the final flow of the contrasted B-scan. The value of N here is even; the variables (x, y) represent the lateral position on the tissue; the depth by z; and t denotes the time variable.

Phase variance (PV)

The phase variance (PV) algorithm is related to the variation of phase (amplitude variations were ignored) emitted by the light wave properties when it intercepts the dynamic or moving particles such as RBCs. It was used to visualize flow by calculating the variance of phase differences between B-scans [182, 204, 205]. In the PV algorithm, the complex product of consecutive B-scans for each pair is calculated and weighted by the mean signal magnitude's inverse square. Later, the circular variance over K pixels along the depth z with N number of repeated B-scans acquired at subsequent positions of the sample was calculated. The resultant average of all the B-scan pairs is given by [56, 98, 193]:

$$\boldsymbol{I_{PV,OCMA}(x,z)} = \overline{M}^2(x,z)\frac{1}{N/2}\sum_{i=0}^{\frac{N}{2}-1}\left(1-\left|\sum_{z'=0}^{K-1}\frac{S(x,z-z',t_{2i+1})S^*(x,z-z',t_{2i})}{|S(x,z-z',t_{2i})^2|}\right|\right), \qquad \textbf{2.4}$$

The averaging can also be applied either along the lateral direction(x) in addition or instead, to averaging along with the depth (z) direction, but this case results in the decrease of the lateral

resolution. The phase noise highly depends on the SNR and thus $I_{PV,OCMA}(x,z)$ is multiplied by the square of average signal amplitude ($\overline{S}$) over the same set of pixels using a simple threshold operation.

$$\overline{\boldsymbol{S}}(\boldsymbol{x},\boldsymbol{z}) = \frac{1}{N}\sum_{i=0}^{N-1}|S(x,z,t_i)|\,, \tag{2.5}$$

Absolute Complex Difference (ACD)

The absolute complex difference (ACD) algorithm is calculated as the amplitude of complex difference between two consecutive B-scan pairs and then averaged over all the acquired pairs from the same location is [93]:

$$\boldsymbol{I_{ACD,OCMA}}(\boldsymbol{x},\boldsymbol{z}) = \left(\frac{1}{N/2}\sum_{i=0}^{\frac{N}{2}-1}|S(x,z,t_{2i+1}) - S(x,z,t_{2i})|^2\right), \tag{2.6}$$

Where $I_{ACD,OCMA}(x,z)$ is the intensity of all image points acquired from corresponding A-scans in the B-scan. The complex amplitudes of S were obtained by Fourier transformation of the dispersion-compensated and wavenumber-linearized interference spectral signal. The spatial coordinates along the fast scanning axis in depth are given by (x,z), and time is t. This method's bulk motion correction was required before calculating the OCM-A signal intensity to achieve a high contrast of the capillaries [206].

Absolute Intensity Difference (AID)

The absolute intensity difference (AID) is the simplest and robust algorithm that calculates the blood flow contrast from the difference of the mean absolute intensities between each of the two consecutive B-scans [93, 192, 203] and is given by:

$$\boldsymbol{I_{AID,OCMA}}(\boldsymbol{x},\boldsymbol{z}) = \left(\frac{1}{N/2}\sum_{i=0}^{\frac{N}{2}-1}|\boldsymbol{V}(\boldsymbol{x},\boldsymbol{z},\boldsymbol{t_{2i+1}}) - \boldsymbol{V}(\boldsymbol{x},\boldsymbol{z},\boldsymbol{t_{2i}})|\right)^{\boldsymbol{2}}, \tag{2.7}$$

where $I_{AID.OCMA}(x,z)$ is the intensity difference between the acquired interframes with successive B-scan structural frames, N is the number of oversampled B-scans and here $V(x,z,t) = |S(x,z,t)|$. The AID method is computationally effective, and it allows to acquire the images faster than other methods. The motion contrasted AID allows suppressing the hyperreflective static structures and improving the image contrast [203].

Speckle variance (SV)

The speckle variance (SV) algorithm calculates the variance of fluctuations in the amplitude between B-scans over time and to visualize the microcirculation. This method enables detecting vessel size dependence on vascular shutdown and transient vessel occlusion [184]. It uses the inter-frame speckle variance based on signal intensity by scanning multiple times the same transverse position [184, 207]. The SV was calculated from standard deviation for each pixel location over time from dataset with time-varying B-scans [181, 184, 208] and was given by:

$$\boldsymbol{I_{SV,OCMA}(x,z)} = \frac{1}{N}\sum_{i=0}^{N-1}\left(V(x,z,t_i) - \overline{V}(x,z)\right)^2, \qquad \textbf{2.8}$$

Where N is the number of multiple repeated B-scans acquired at the same location in the series and, $I_{SV}(x,z)$ indicates the value of intensity at lateral location x and the depth position z. The variance is higher in the location of flow compared to the signal from the static tissue.

2.4 Motion correction algorithms for mouse brain

The OCM-A post-processing for *in-vivo* mouse brain imaging requires a bulk motion correction algorithm to effectively visualise the microvasculature. The physiological fluctuations such as cardiac and respiratory motions caused by heartbeat and breathing of the mouse are inevitable during the experiment and mainly cause the global phase fluctuations (GPF's) and bulk image shifts (BIS's) in the phase of OCM signal, respectively. The removal of phase variations will suppress the global GPFs either in the lateral or axial direction. In contrast, a method based on cross-correlation maximization is effective for the compensation of BIS's. The GPFs and BIS's were coupled to each other, and the appropriate combination of the motion correction algorithms will effectively suppress the motion artifacts [206]. The cross-correlation $\Gamma(t)$ is used as an index of tomographic image stability and is defined as:

$$\boldsymbol{\Gamma(t)} = \frac{\int S(z,x,t)S^*(z,x,t_0)\,dz\,dx}{\sqrt{\int|S(z,x,t)|^2\,dz\,dx}\,\sqrt{\int|S(z,x,t_0)|^2\,dz\,dx}}, \qquad \textbf{2.9}$$

where $S(z,x,t)$ and $S^*(z,x,t_0)$ are the complex-valued and complex-conjugate intensity signal of $S(z,x,t)$ at a given reference time t_0. The first frame was generally considered as the reference frame, $t_0 = 0$. The cross-correlation term was used to quantify the similarity between the frames acquired at a time t and the reference frame. The magnitude of the real part of the

cross-correlation $|\mathrm{Re}[\Gamma(t)]|$ is more sensitive to the variation in phase of the signals. The image decorrelation caused by the cardiac and respiratory motions was attributed to small but high-frequency dips and large and low-frequency dips.

Correction of the global phase fluctuations (GPF's)

The cardiac and respiratory motion of the mouse also causes the phase fluctuations of the OCM signal. These phase fluctuations were observed in both the lateral and axial directions across the voxels. The axial global phase fluctuations at each lateral position x and time t ($GPF_{axial}(x,t)$) is corrected by maximizing the real part of cross-correlation between the phase-shifted and reference frames and is given by:

$$Re\left[\Gamma_{phase}(x,t;GPF_{axial}(x,t)\right] = \frac{Re\left[\int S(z,x,t)e^{iGPF_{axial}(x,t)}\, S^{*}(z,x,t_0)\, dz\right]}{\sqrt{\int |S(z,x,t)|^2\, dz}\,\sqrt{\int |S(z,x,t_0)|^2\, dz}}\,, \qquad \textbf{2.10}$$

The lateral global phase fluctuations, $GPF_{lateral}(z,t)$ at each depth z and time, t defined as:

$$\boldsymbol{GPF_{lateral}(z,t)} = -arg[\int S(z,x,t)\, S^{*}(z,x,t_0)\, dx]\,, \qquad \textbf{2.11}$$

The axial global phase fluctuations, $GPF_{axial}(x,t)$ independent of depth by z is given by:

$$\boldsymbol{GPF_{axial}(x,t)} = -arg[\int S(z,x,t)\, S^{*}(z,x,t_0)\, dz]\,, \qquad \textbf{2.12}$$

When both lateral and axial global phase fluctuations were compensated, the amplitudes of the motion-oriented dips due to heartbeat were reduced remarkably, but the effect is small for respiration-oriented dips [206]. This is because the breathing or respiratory motions produce larger BIS's than the pixel size, and therefore GPFs alone cannot compensate for the supra-pixel movements.

Correction of the bulk image shifts (BIS's)

The correction of bulk image shifts (BIS's) was achieved by maximizing the cross-correlation between the shifted images to the reference frame. The cross-correlations for the various shifted frames obtained at each frame is given by:

$$\boldsymbol{\Gamma_{shift}(\Delta z,\Delta x,t)} = \frac{\int S(z+\Delta z,x+\Delta x,t)\, S^{*}(z,x,t_0)\, dz\, dx}{\sqrt{\int |S(z+\Delta z,x+\Delta x,t)|^2\, dz\, dx}\,\sqrt{\int |S(z,x,t_0)|^2\, dz\, dx}}\,, \qquad \textbf{2.13}$$

where $S(z,x,t)$ and $S^*(z,x,t_0)$ are the complex-valued and complex-conjugate intensity signal of $S(z,x,t)$ at a given reference time t_0. The initial step is to upsample the sub-pixel shifts in the images with the spline interpolation (cubic). Then the upsampled image shifts are compensated for, and the image is retrieved back to its original sampling by downsampling. This corrects lateral and axial shifts in the image by reducing the large dips in the cross-correlation due to respiration. The BIS's motion correction provides only a small enhancement to the absolute real part of the cross-correlation signal as it is susceptible to phase fluctuations.

2.5 OCM-A data structure

The OCM data structure corresponds to 3D spatial image sets $I(x,y,z)$; the lateral dimensions are given by (x,y) and axial dimension refers to (z) and it is shown in Figure.2. The three major components: A-Scan, B-scan, and C-Scan, or the three-dimension. The B-scans refer to both XZ and YZ images, while the *en-face* image is for XY slice.

Axial scan or A-scan

It is the basis for the image generation unit and was defined as the axial or depth profile of the back-scattered signal from the tissue retrieved at one scanning position. It was obtained by the inverse Fourier transform of the acquired spectral interferometric signal $\Gamma(\Delta z_s)$. The A-scan signal of the sample at position Δz_i with scattering N layers characterised by the reflectivity profile in axial direction $R(\Delta z_s)$ is given by:

$$\boldsymbol{\Gamma(\Delta z_s) = R(\Delta z_s) \otimes h(\Delta z)}\,, \qquad \textbf{2.14}$$

Where $R(\Delta z_s) = \sum_{i=1}^{N} \rho_i \delta(z - \Delta z_i)$,

$h(z) = \left|\mathcal{F}_{k\to z}^{-1}[\widetilde{I_0}(k)]\right|$ is the point spread function (PSF) in the axial direction,

$\widetilde{I_0}(k) = \sqrt{\eta_s(k)\eta_r(k)}\, I_0(k)$ and $\otimes$ represents the convolution operator.

The A-line is obtained from the magnitude of the complex part of the axial profile and then converted to a logarithmic scale. The A-scan profile retrieved is shown in Figure 2(a) as a function of intensity and depth position z for one particular corresponding position (red dotted line) of the corresponding B-scan in Figure 2(b). The OCM-A axial scan is same as the structural A-scan except that the static signals are also filtered and reduced to the noise level.

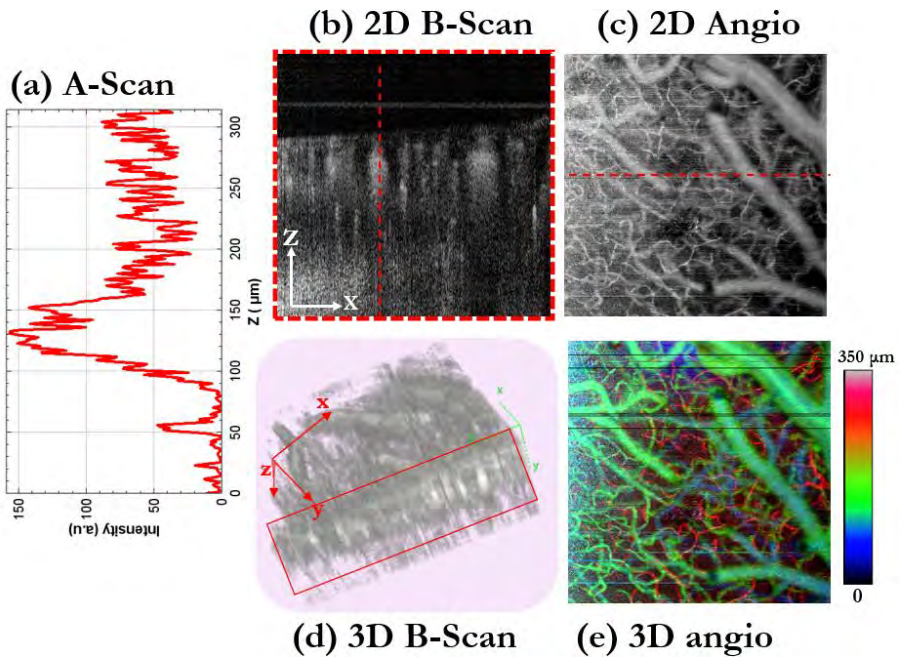

Figure 2-2 The OCM-A data structure of the in-vivo mouse brain representing: (a) 1D A-scan depth profile, (b) 2D cross-sectional B-scan,(c) 2D angiographic B-Scan, (d) the rendered three dimensional volumetric B-scan and, (e) three-dimensional angiography (colour bar shows the Z-scale). The red dotted line indicates the particular chosen position of the scan.

Cross-sectional image or B-scan or tomogram

The two-dimensional (2D) image is acquired either by scanning the beam using a deflector over the sample or when the sample was translated through the beam. The B-scan is a series of multiple adjacent positions of A-scans acquired along one transverse direction. The intensity values were displayed as a measure of the transverse and depth positions. An exemplary cross-sectional image for the in-vivo mouse brain imaging using OCM-A is displayed in Figure 2(b). White and black colours represent the highly and weakly scattered pixels of the cerebral microvasculature. Whereas the in-between back-scattered intensities are displayed as different greyscale levels in Figure 2(c). The B-scan rate is defined as the multiplication of the A-line rate, and the number of A-lines acquired per B-scan, and the speed of scanning optics sets it.

Three-dimensional reconstruction (3D)

It was achieved by acquiring consecutive B-scans in a raster scan. It composes the cross-sectional images to form a volumetric 3D reconstruction. The *en face* image was used to visualize the projection from the entire depth of the 3D dataset from the *XY* plane or at a specific depth position as shown in Figure 2(e). The rendered 3D OCM data of the mouse brain with different viewing angles was displayed in Figure 2(d).

2.6 Parameters of OCM

Longitudinal or Axial resolution

It is the shortest distance between the two back-scattered layers of the specimen, while the layers are still distinguishable along the scanning beam of the optical tomogram. For the light source intensity, where the cross-section of the emitted beam has a Gaussian distribution, the longitudinal resolution as a function of coherence length (l_s) described as:

$$\boldsymbol{\delta z} = \frac{l_s}{2} = \frac{2ln2}{\pi}\frac{\lambda_s^2}{\Delta\lambda} \quad , \qquad \textbf{2.15}$$

Where l_s - size of coherent light source round trip, λs - central wavelength of the source and, Δλ - the full width of the beam at the half maximum (FWHM) of the light source [171]. The longitudinal resolution for the femtosecond light ($\Delta\lambda$) source is ≤ 2 μm. The axial resolution of OCM is determined by the shape of the light beam, the size ~150nm of the coherence length (l_s) and the spectral bandwidth because the image information was reconstructed from interferometric signal along the A-scan in the axial direction. The z-sectioning in OCM provides the depth of focus (DOF): the region where the tomographic signal is sharp. The maximum depth range (Δz) achievable in a single A-scan defined as

$$\boldsymbol{\Delta z} \approx \frac{l_s}{n}N = \frac{\lambda_s^2}{4n\delta\lambda} \quad , \qquad \textbf{2.16}$$

where the spectrometer resolution is governed by the Nyquist theorem, $\delta\lambda = \frac{\Delta\lambda}{\mathrm{N}}$, N − the total number of pixels accumulated at the array detector and, Δλ − FWHM or spectral bandwidth of the coherent light source. The finite spectrometer resolution causes a signal dropout in-depth, thereby creating a loss of axial resolution and limiting the maximum achievable depth [209].

Lateral or transverse resolution

It is defined as the function of focused media properties and the objective placed in front of the sample. The size of the tightly focussed beam spot is inversely proportional to the numerical aperture (NA):

$$\boldsymbol{\Delta x} = \frac{4\lambda}{\pi}\frac{f}{d} = 1.27\frac{\lambda}{NA} \quad , \qquad \textbf{2.17}$$

Where f - objective lens focal length,

d - probing beam spot size and,

λ - wavelength of the source. The lateral resolution is related to the wavelength of the source and optics in the sample arm used for focusing the beam into the sample. The dependence of NA and DOF in Figure 3. shows that the higher the NA, the greater the focusing power translating into better transverse resolution and short depth of focus (DOF). At the same time, the low NA corresponds to a large DOF. The imaging depth and width of the beam affect the lateral resolution of the OCM.

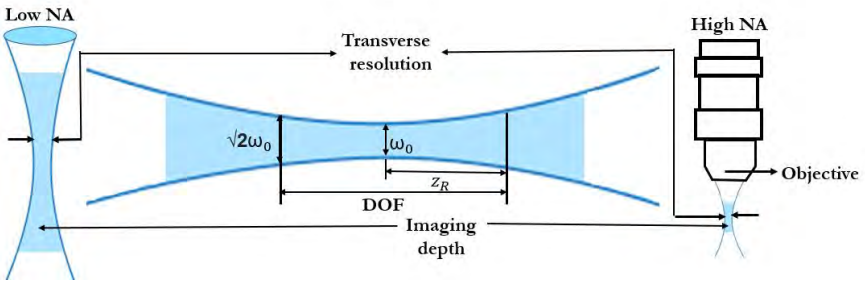

Figure 2-3 The depth of focus and transverse resolution in case of low and high numerical apertures resolution is shown for the focusing of the Gaussian beam.

Depth of Field (DOF) or Imaging Depth

Imaging depth is another critical parameter, especially for in-vivo biological tissue imaging studies. The area occupied along the axial direction of the beam in which transverse resolution was maintained called depth of field (DOF) and was represented in Figure 2-3. When designing the optical path of the object arm, the appropriate selection of aperture lens and focal length plays a vital role in determining the lateral resolution (Δx) and it also affects the DOF. The DOF scales a function of the square of the transverse resolution and is given by:

$$\boldsymbol{DOF} = 2z_R = \frac{\pi(\Delta x)^2}{4\lambda} \quad , \qquad \textbf{2.18}$$

where z_R – Rayleigh region or the confocal parameter,

λ – central wavelength of the source, and

Δλ – the full width of the beam at the half maximum of the light source (FWHM).

There is a trade-off between DOF and the transverse resolution, limiting the light penetration in the tissue to only a few millimetres depth. The major limitation of the light penetration into the tissue is scattering.

Signal to Noise Ratio (SNR)

The SNR is generally defined as the ratio of mean signal power to the noise level or power. The noise power is a statistical quantity defined by the signal-free region's variance (typically at higher depths) within the optical tomogram. The total noise variance (σ^2_N) is the sum of three predominant noise contributors: detector or receiver's noise (σ^2_{re}), shot noise (σ^2_{shot}) and excess noise (σ^2_{ex}) or also called relative intensity noise [209, 210]. The detector noise is the result of the thermal fluctuations caused by the electronics of the system. At the same time, the shot noise was caused by the photocurrent variance resulting from the arrival and detection of light photons onto the detector. The excess noise causes the intensity fluctuations, for example by self-beating of random modes in the light source cavity; air convection present in the optical system [171, 177, 211, 212]:

$$\boldsymbol{SNR} = \frac{\langle s^2 \rangle}{\sigma^2_{shot} + \sigma^2_{re} + \sigma^2_{ex}} = \frac{\langle s^2 \rangle}{\sigma^2_N} \quad , \qquad \textbf{2.19}$$

Where the total noise variation, $\sigma^2_N = \sigma^2_{shot} + \sigma^2_{re} + \sigma^2_{ex}$,
$\langle s^2 \rangle$ – integrated signal at different depths in the OCM over a period of time. The total noise power dominates the shot noise, and the sensitivity has a linear dependence on the light source power in an optimized system. For the system with low output power, the detector noise limits the sensitivity, and at a higher output power, there is no additional sensitivity gain due to the restraint of excess noise. In the optimal case, the shot noise with the variance described by the following formula is dominant:

$$\boldsymbol{\sigma^2_{shot} = \frac{P_0}{N} \frac{\rho \eta \tau}{h\nu_0} \gamma_r R_r} \, . \qquad 2.20$$

When the intensity of the sample reflectivity is assumed to be weak, $R_s \ll R_r$, then the noise contribution is mainly from the reference arm, and the SNR was defined as [209]

$$\boldsymbol{SNR} = \frac{2(\alpha)^2 P_r P_s}{\sigma^2_{shot} + \sigma^2_{re} + \sigma^2_{ex}} = \frac{\frac{1}{N}(\frac{\rho \eta \tau}{h\nu_0} P_0)^2 \gamma_r R_r \, \gamma_s R_s}{\frac{P_0}{N} \frac{\rho \eta \tau}{h\nu_0} \gamma_r R_r + \sigma^2_{re} + \sigma^2_{ex}} \quad , \qquad \textbf{2.21}$$

where α is dependent on the quantum efficiency (η) of the detector ;
N – total number of pixels on the detector ;
ρ – spectrometer efficiency ;
τ – integration time;
P_0 – source power at the input of the interferometer;
$E_0 = h\nu_0$ is the photon energy at the central wavelength.

The fractions of light power obtained from the reference arm (P_r) and sample arm (P_s) at the input of spectrometer are given by $\gamma_r R_r P_0$ and $\gamma_s R_s P_0$ respectively. In spectrometer based Fourier domain OCM when the reference arm was well adjusted to having ~75% intensity of the detector saturation, the contributions from the receiver noise and the excess noise become negligible [177]. Therefore, the SNR in the shot-noise is proportional to the integration time (τ) and power of the sample arm (P_s) and can be approximated as:

$$\boldsymbol{SNR} \approx \left(\frac{\rho\eta\tau}{E_0}\right) P_s \approx \left(\frac{\rho\eta\tau}{h\nu_0}\right) \gamma_s R_s P_0 , \qquad \textbf{2.22}$$

Sensitivity (∑)

The sensitivity is quantified as ability of system to detect even smallest amount of back-reflected light from the sample ($R_{s,min}$) to characterize the OCM setup. It is defined as the ratio of generated signal power with a perfectly reflecting mirror (R = 1) and $R_{s,min}$. When signal and inherent noise of the system are almost equal, then attenuation in signal results in an SNR of 1, such that sensitivity is:

$$\boldsymbol{\Sigma} = \frac{1}{R_{s,min}} , \qquad \textbf{2.23}$$

The signal powers generated are dependent on the corresponding reflectivity. In the shot-noise limit, the sensitivity is proportional to the probe power ($\boldsymbol{\gamma_s P_0}$) and the integration time (τ) as

$$\boldsymbol{\Sigma} = \frac{\rho}{e^-} \tau \gamma_s P_0 . \qquad \textbf{2.24}$$

2.6.1 OCM imaging parameters

The image quality is assessed quantitatively with four parameters corresponding to different image properties analyzed for Bessel and Gaussian OCM data. To optimize the performance of OCM imaging, the SNR, DR, C and CNR are evaluated.

(i) The Image signal-to-noise ratio (ISNR):

$$\boldsymbol{ISNR} = \frac{m_{sig}}{\sigma_{bkg}} , \qquad \textbf{2.25}$$

Where m_{sig} is the mean value of the signal magnitude and σ_{bkg} is the standard deviation of the background.

(ii) The speckle contrast (C):

$$\boldsymbol{C = \frac{\sigma_{sig}}{m_{sig}}} \quad , \tag{2.26}$$

Where σ_{sig} is the standard deviation of the signal magnitude

(iii) The image dynamic range (DR):

$$\boldsymbol{IDR = m_{sig} - m_{bkg}} \quad , \tag{2.27}$$

Where m_{bkg} is the mean value of the background

(iv) The contrast-to-noise ratio (CNR):

$$\boldsymbol{CNR = \frac{m_{sig} - m_{bkg}}{\sigma_{sig}^2 + \sigma_{bkg}^2}} \quad , \tag{2.28}$$

2.7 Gaussian optics vs Bessel beam illumination

The sample illumination in OCM was typically performed using a focussed optical beam with a Gaussian transverse profile, called a Gaussian beam.

$$\boldsymbol{I(r) = I_0 e^{\left(-\frac{2r^2}{w(z)^2}\right)}} \tag{2.29}$$

Where I_0 – peak irradiance at the centre of a light beam;

r – radial distance away from the axis;

$w(z)$ – radius of the beam at irradiance $1/e^2$ of I_0 ;

k – wavenumber of the light;

The transverse beam width according to the Rayleigh range criterion varies with depth [213, 214] and is given by:

$$\boldsymbol{w(z) = w_0 \sqrt{1 + \left(\frac{z}{z_R}\right)^2} = w_0 \sqrt{1 + \frac{{\lambda_0}^2 \pi^2}{{w_0}^4} z^2}} \quad , \tag{2.30}$$

Where w_0 – waist radius in focus at irradiance $1/e^2$ of peak intensity beam;

λ_0 – central wavelength;

z – axial distance;

$z_R = \frac{{w_0}^2}{\pi \lambda_0}$ is the Rayleigh range.

The Rayleigh range is defined as the distance over the region where the cross-sectional area of the beam at focus which doubles its value and is dictated by the tranverse resolution of the OCM

in biological tissue. The sample-induced scattering and aberrations governs the trade-off between the depth and transverse resolution. The objective lens used to focus the collimated Gaussian beam in a conventional OCM system and it alters the beam parameters such as the focal position and beam waist radius, but the beam profile remains Gaussian in nature. The depth of focus (DOF) of such system is twice the Rayleigh range and is given by:

$$\boldsymbol{DOF_{Gaussian}} \cong \frac{8\lambda}{\pi}\left(\frac{f}{D}\right)^2 \propto \frac{1}{NA^2}, \qquad \textbf{2.31}$$

Where λ – wavelength of collimated beam;

D – diameter of the beam;

f – focal length of lens;

NA – numerical apertuture of the objective;

The beam waist radius of the Gaussian beam ($\boldsymbol{r_G}$) at the focus is given by:

$$\boldsymbol{r_G} = \frac{4\lambda}{\pi}\left(\frac{f}{D}\right) \propto \frac{1}{NA}. \qquad \textbf{2.32}$$

Therefore the system resolution is defined by the waist radius of the beam and can be improved by using an objective with high numerical aperture but it rapidly reduces the depth of focus.

The non-diffracting beams such as Bessel beam are generated by conventional optics and are applied to OCM imaging in place of the Gaussian beams to have an advantage of extended depth of focus (DOF) while still maintaining a high lateral imaging resolution [131, 132, 170, 215, 216]. Bessel beams [215] are generated by an optically efficient method using axicon lens [128, 217, 218] to increase the extend of the depth of field (DOF) compared to Gaussian beam [170, 216, 219, 220] while simultaneously achieving a high lateral resolution with the decrease in the illumination, signal to noise ratio (SNR) penalty and sensitivity as the trade-off for OCM [133, 170]. The generated Bessel beam maintains its radial intensity profile over a large propagating distance compared to the Gaussian beam [170]. The intensity distribution of the axicon illuminated by a collimated beam with optical axis aligned along z is given by:

$$\boldsymbol{I}(\boldsymbol{r},\boldsymbol{z}) = A^2\,(R_z)\,R_z\,\frac{2\pi k\,sin(\alpha)}{cos^2(\beta)}\,j_0^2\,(kr\,sin(\alpha)), \qquad \textbf{2.33}$$

Where (r, z) – radial and axial coordinates in the region after the axicon lens respectively;

k – wavenumber of the light;

β – apex angle or angle of the surface of the axicon;

j_0 – zeroth order of Bessel function;

α – the angle of light ray after refraction propagating through axicon and parallel to the optical axis;

A^2 (R_z) – energy of the incident beam;

R_z – radius in the region before the axicon given by:

$$\boldsymbol{R_z = \frac{z\,tan(\beta)}{1-\tan(\alpha)\tan(\beta)}}\ . \qquad \textbf{2.34}$$

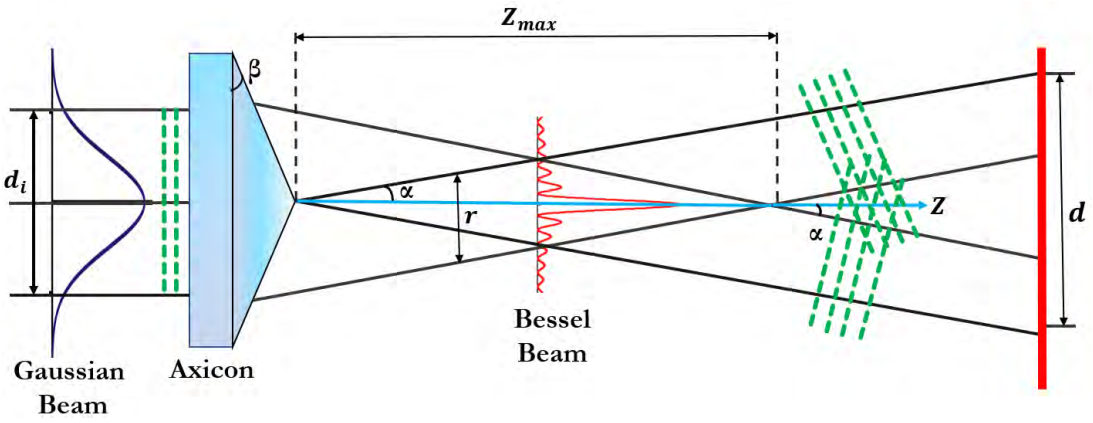

Figure 2-4 Schematic of the Bessel beam generation using an axicons lens.

The Bessel beam is generated only for a finite length, having a finite radius beyond the apex of the lens (as in Figure 2-4) using an axicon lens and illuminating beam. This region was defined as the depth of focus (DOF) of the Bessel beam given by:

$$\boldsymbol{DOF_{Bessel} \cong \frac{d_i\,(cot(\alpha)-tan(\beta))}{2}}\ . \qquad \textbf{2.35}$$

Where d_i is the incident beam diameter. From Eq. 2.24, the central peak radius r_0 at any given value of z and occurs at the first zero in the Bessel function.

$$j_0\,(kr_0\,sin(\alpha)) = 0. \qquad \textbf{2.36}$$

The position of the zero-order Bessel fringe is given by:

$$\boldsymbol{r_{0-Bessel} \approx \frac{2.4048\lambda}{2\pi\,sin(\alpha)}}\ . \qquad \textbf{2.37}$$

2.8 Optical properties of natural and synthetic scatterers

The exogenous contrast agents enhance the contrast of measured signals in OCM-A and thus increase the visibility of microvasculature [221]. The positive contrast agents that increase the local OCM signals include natural scatterers like intralipids [164, 165], synthetic scatterers like gold nanorods and nanoparticles [138, 139, 222] and other highly scattering nanoparticles [223, 224]. The contrast agents identified and suitable for brain imaging that is most efficient for improving signal contrast are intralipids and large gold nanorods (LGNRs).

2.8.1 Scattering of erythrocytes

Erythrocytes or red blood cells (RBCs) are asymmetric in shape (biconcave disk or ellipsoid without applied stress) with a short and long axis of 6.5 μm and 1.5 μm respectively in rats [225-228]. They have a high anisotropically scattering value (g ~0.95 for porcine blood at 1300 nm) [229]. The intrinsic scttering properties enables the contrast of OCM without use of external contrast agents. The motion of the scattering RBCs within the blood vessel causes the signal flucuation and thus produces the decorrelation in the OCM signal. The OCM-A signal arises by comparing the signal from the motion contrast of the dynamic scatters at different times but at the same spatial location. The intensity, phase or complex signal-based OCM-A processing algorithms are used to vizualise the perfused vessels.

2.8.2 Optical properties of natural scatter - Intralipids

Intralipids are spherically symmetric particles with fairly isotropically scattering and highly scattered lipid or fat emulsions suspended in water. They are similar to milk offering unique advantages such as low cost, non-toxic, sterile availability and high accessibility in the clinical environment [230, 231]. The diameter of lipid particles ranges from a few tens of nanometers (20 nm) to over 600 nm, with an average of around 214 nm [232]. They are highly scattering particles with low absorption, homogeneous allowing adjustable scattering and absorption coefficients. They are used as an extrinsic contrast agent for OCM-A and have been applied in various fields such as diffuse imaging, spectroscopy, clinical imaging, tissue imaging, surgery, nanomedicine and other fields of study [233-245]. They were first applied for OCM brain imaging studies on rat brain by Merkle et al. [164] to improve the OCM signal intensity and angiography of cerebral microvasculature [108, 162, 164, 165].

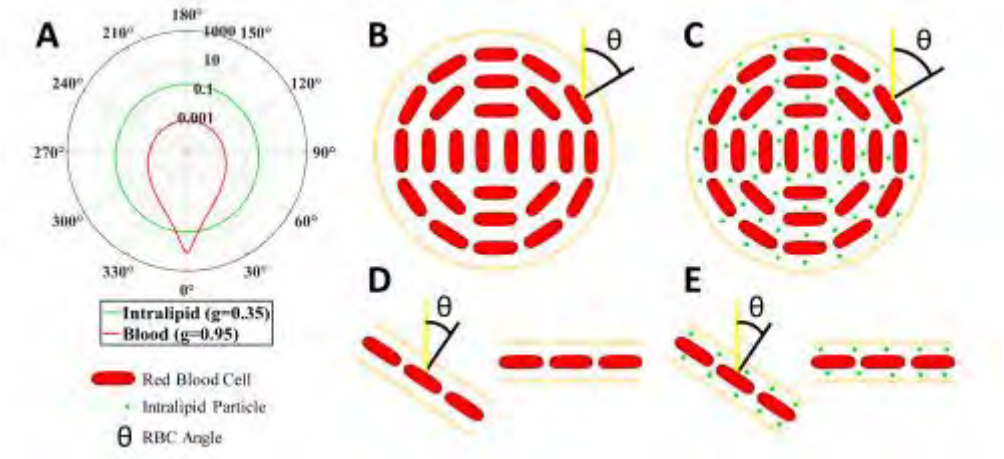

Figure 2-5 The optical properties of intralipids (a) shape and size of intralipid particles different from RBCs with scattering phase function of suspension for RBC vs intralipid scattering phase function with forward° and backscattering scattering corresponding to 0 corresponds and 180° respectively (b) The asymmetric RBCs due to shear flow orienting themselves with their flat faces, pointing outwards in vessel lumen (c) The comparison of intralipid particles and RBCs (d) The RBCs oriented away than RBCs from the incident light and are in perpendicular direction to capillaries [54-56] (e) The comparison of intralipid particles showing that they lack an intrinsic orientation. Copied from [167].

There are several assumptions are required for the dynamic contrast OCM signal (DyC-OCM) analysis based on indicator-dilution theory [246-248]:

(i) The blood and Intralipid tracer must be mixed well prior to imaging.

(ii) Due to the the small size of the Intralipid particles incomparision to RBCs (> twice larger in volume) it is assumed that intralipid acts as a blood plasma tracer [168].

(iii) The change in OCM signal at any point in time, within any given voxel, the signal relative to baseline it is assumed to be proportional to the number of Intralipid particles.

(iv) The hemodynamic parameters are assumed to be constant, and not perturbed with injection during the course of the experiment.

It is expected that Intralipid scattering increases proportionately with decrease in wavelength compared to RBC scattering due to small size of Intralipid particles relative to RBCs.

2.8.3 Basic optical properties of synthetic scatterers - LGNRs

The large gold nanorods (LGNRs, ~100 × 30 nm) are usually almost twice larger than the usual gold nano rods (GNRs, ~50 × 15 nm) and are known for their optical properties to enhance the OCM scattering signal [158]. The contrast of the spectral domain OCM (SD-OCM) can be

enhanced ~30-fold and ~110-fold greater signal intensity and spectral signal of the OCM, respectively, using LGNRs compared to conventional GNRs [138]. The LGNRs are tuned for plasmonic resonance peaks in living tissue to enhance the contrast.

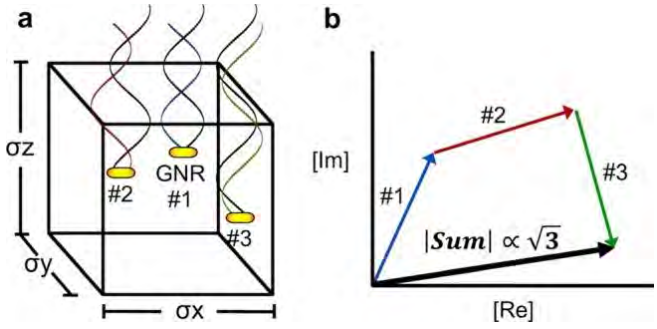

Figure 2-6 Schematic of the interference of the gold nanorods (GNRs) in an imaging voxel. (b) The vector sum of the scattered photons, each with a random phase. Copied from [249].

The physical model that predicts the OCM signal detected from the scattering particles with a size of the nanoscale was described by Winetraub et al. [250]. The advantage of this model is that it assumes the principle of ray scattering and thus do not require either the information of particle-specific parameters or the most dominating physical scattering mechanisms [249].

The following highly simplified assumptions are made:

(i) The same amount of light was reflected by all particles within the sample.

(ii) The ray optics was used to model the reflections, and

(iii) In a single voxel, the amount of multiple scattered photons are negligible.

Henceforth, this model is generally applicable to the particles with heterogeneous scattering environments independent of the particle's morphology. The electric field within the voxel is represented as the sum of reflections from the N particles in a given imaging voxel, as shown in Figure 2-6. The voxel was depicted as a cube, but in reality, it was optically determined with an ellipsoid shape. The reflections from the particles are considered vectors of equal magnitude and random phases. The mean magnitude in a voxel with speckle intensity X, is a function of N and is given by:

$$\boldsymbol{X}(\boldsymbol{N}) = \begin{cases} A & N = 1 \\ 0.89\, A\sqrt{N} & N \geq 2, \end{cases} \qquad \textbf{2.38}$$

Where A is the OCM signal intensity of a single particle,

N number of particles in an imaging voxel,

The length of the resultant mean vector obtained by the sum of the random phase vectors is proportional to A and $\sqrt{N}$ as shown in Figure 2-6(b).

Chapter 3 Methods

3.1 Experimental design and layout for OCM

The optical coherence microscopy (OCM) experimental setup is designed, aligned, characterized, and validated for in-vivo brain imaging. The Gaussian-beam OCM (G-OCM) was introduced for cerebral angiography, and Bessel-beam OCM (B-OCM) extends the capabilities of OCM for structural brain imaging. The parameters such as axial resolution, lateral resolution, depth of imaging, and sensitivity define the setup's image quality and benchmarking. Bessel beam offers more extended imaging depth but suffers from contrast degradation due to the extra side lobes in the point spread function (PSF), inherent SNR trade-off compared to Gaussian beams, and complication of the system [1]. The first sub-chapters introduce the OCM, a microscopic optical system with a Gaussian beam and an extended focusing system using axicon to maintain high lateral resolution for different imaging depths. The following sub-chapters present the motivation to build the system and a detailed description of its structure and diagnostics. We also used the commercial PS-OCM Telesto -Thorlsbs system for some experiments. Table 1 shows a summary of the basic parameters characterizing the systems used in the experiments.

3.1.1 Gaussian beam optical coherence microscopy (G-OCM)

The home-built standard Gaussian OCM setup was based on the Michelson interferometer configuration. We used ~6 femtoseconds (fs) short-pulse laser light source (Fusion Femtolasers, Austria) with 130 nm bandwidth and centred at 795 nm. A fiber beam splitter (BS) of 75:25 was used to split the output light into the reference arm and object arm, respectively. The fiber coupler is used to couple the output light reflected from both the arms and then directed into the spectrometer. The objective lens with 4x magnification and numerical aperture (NA) of 0.13 was used to focus the sample. The theoretical estimation of the Depth of Field (DOF) is ~100 μm for the transverse resolution of Δx ~4.5 μm at FWHM of the Gaussian profile; whereas the high axial resolution of the system is estimated to be ~2.2 μm. The sensitivity of the system was calculated to be 92 dB. The scanning protocol used for the OCM-A consists of 400 A-scans and 400 B-scans with 6 oversampling. A custom-made spectrometer: high-speed line scan camera (Basler Sprint, Germany) with 2048 pixels and 70 kHz acquires the interference fringe signals. The OCM system has an option of choosing the interchangeable imaging optics for microscope objectives (OBJ): 4× NA 0.13 or 10× NA 0.25 (Olympus Plan Fluorite). Most of the

experiments were performed with OBJ 4× of NA 0.13 with an equivalent full aperture width of 11.7 mm and the effective focal length = 45 mm. The average optical power used for the sample illumination is 10 mW. The light beam entering the objective lens was expanded to 6 mm using achromatic lenses (L); L3 = 30 mm and L4 = 100 mm (at $1/e^2$ of the Gaussian profile) as shown in Figure 3-1. The dedicated stand-alone software was developed using LabView to synchronize galvanometric (galvo) scanners and camera, control scanning protocols, and data processing for motion correction, averaging, and angiography. The data analysis has enabled the volumetric reconstruction for 3D visualization of mouse cerebral microvasculature for both structures and angiography mapping.

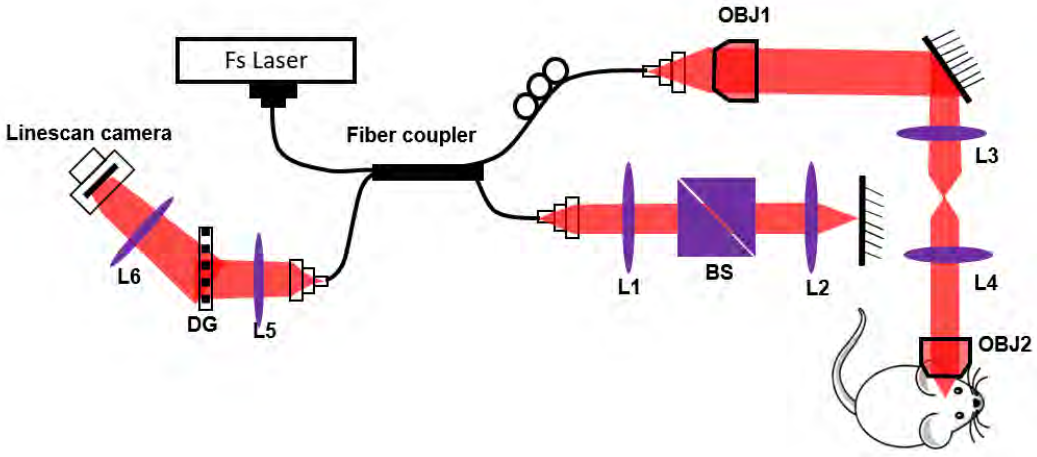

Figure 3-1 Schematic of the Gaussian beam OCM experimental setup (G-OCM): achromatic doublet lenses: L1-L5 (focal length 'f': 250 mm, 100 mm, 30 mm, 100 mm, 50 mm respectively); L6-telecentric lens (f: 80 mm); objective: OBJ- 20× with 0.4NA and OBJ2 - 4× with 0.13 NA; BS: beam splitter 75:25; DG: diffraction grating; Fs laser: femtosecond laser; M: mirror.

3.1.2 Bessel beam optical coherence microscopy (B-OCM)

The Bessel beam OCM was constructed in-house and built based on a Mach-Zehnder interferometer using an axicon lens to generate a Bessel beam with Gaussian detection [62, 170]. The output light power from the femtosecond laser source (Fusion, Femtolasers; pulse width: 6 fs, laser bandwidth: 130 nm, central wavelength: 795 nm) is divided into the sample and reference arms using a 70:30 fiber beam splitter (AC Photonics, USA). The light intensity in the reference arm was controlled using a gradient filter, and glass was used for dispersion compensation to match both arms of the interferometer. The backscattered light from the sample and the reference arms were coupled and redirected into the custom-made spectrometer with the line-scan camera (Basler Sprint, Wasatch Photonics, 70 kHz, 2048 pixels, diffraction grating: 1200 pmm). The optical path difference between both interferometric arms is adjusted using a combination of translational stage and beam splitter. The Bessel beam was generated in

the object arm by collimating the input beam diameter to ~3.47 mm and then passing through axicon lens (apex angle 176°, Thorlabs, USA). The light beam was scaled and directed to the focal plane of the tube lens using two telescopes. The tube lens was used to transform the beam to a light ring shape, and the beam was then positioned at the objective lens 10×, NA 0.3 (Olympus RMS10X-PF) aperture beam at the object position to create the actual Bessel beam. The objective lens has provided a working distance as long as 10 mm has facilitated the manipulation of the mouse. A pair of galvanic scanners are mounted between the second telescopic lenses to enable 3D imaging and scan both the axes perpendicular to the optical axis. A CCD web camera (Microsoft HD LifeCam) was used to preview and for precise positioning of the mouse. The specifications for the Bessel beam OCM are imaging depth of ~800 µm, transverse resolution 2.2 µm, axial resolution in tissue ~3 µm, the sensitivity 94 dB and, power at the sample focus 11 mW, imaging range in XY and Z direction as ~3 mm and ~2 mm respectively.

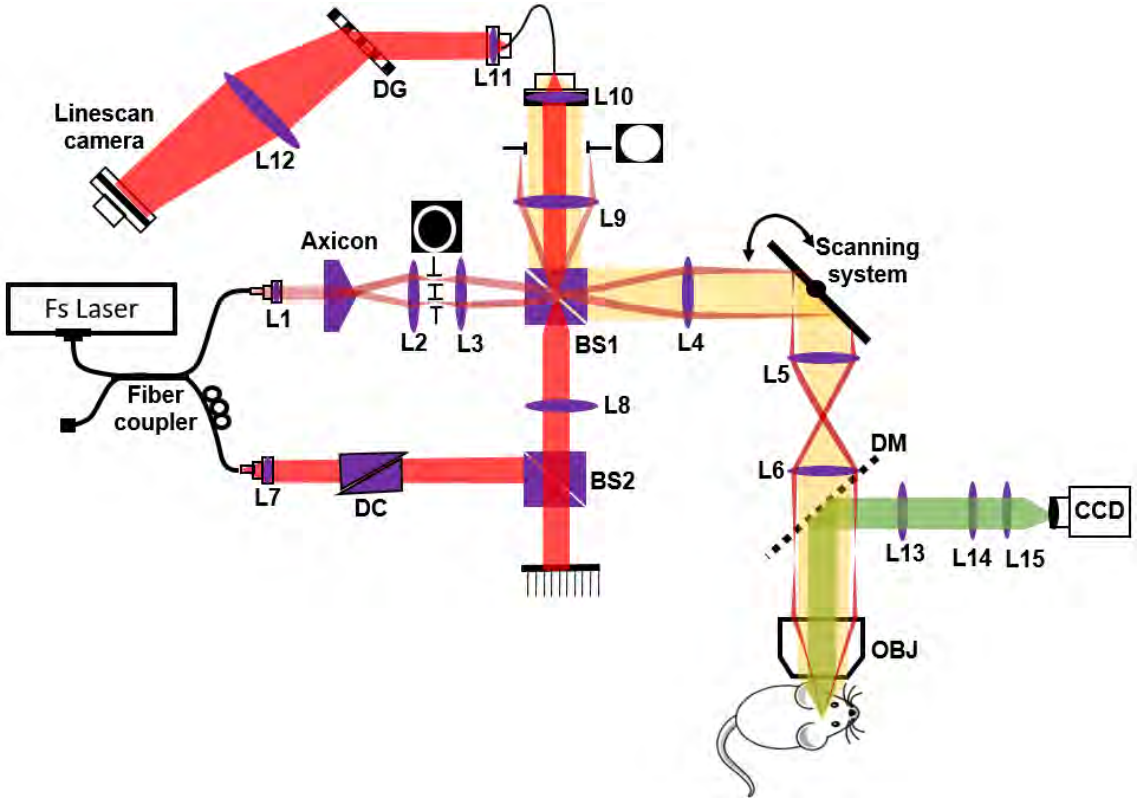

Figure 3-2 Schematic of the Bessel beam OCM (B-OCM) experimental setup; BS: beam splitter 70:30, DC: dispersion compensation; DG: diffraction grating; DM: dichroic mirror; OBJ: objective; Fs laser: femtosecond laser; collimating lens L1 (f: 16 mm; illuminating lenses L2-L3 (f: 150 mm, 100 mm respectively); lens in the front and behind the scanners lens L4-L5 (f: 100 mm, 100 mm respectively); L6-telecentric lens (f: 165 mm); collimating lens L7 (f: 16 mm); collimating lenses directed into the spectrometer L9-L12 (f: 50 mm, 100 mm, 100 mm, 80 mm respectively).

3.1.3 Polarization sensitive-optical coherence tomography (PS-OCM)

The Telesto series polarization-sensitive OCM system (TEL221PS, Thorlabs, Germany), with an open construction to enable the customization of scanning path, is used to acquire both cross-sectional (2D) or volumetric (3D) images. The single-input PS-OCM system uses a femtosecond laser source beam centred at 1300 nm wavelength consists of an interferometer (both reference arm and sample arm), scanners and, a unique dual-detector for the acquisition and imaging operated at full imaging speed for highly robust and reproducible measurements. The scanning system was housed within the interferometer, and the reference arm is placed near the sample to achieve better phase stability of both arms of the interferometer. The Telesto PS-OCM system is optimized to achieve a high-depth (~2.5 mm) with 5.5 µm axial resolution (in the air) at 1300 nm central wavelength, high-resolution and, maximum sensitivity of 109 dB at 5.5 kHz scan rate. In addition, the ThorImage® PS-OCM software package is used for the post-processing to obtain A-scans, B-scans, and angiographic data.

Parameters	Gaussian	Bessel	Telesto
Sensitivity (dB)	94	92	109
Depth of imaging (µm) (tissue)	350	800	2600
Axial resolution (µm) (tissue)	2.2	3	4.2
transverse resolution (µm)	2.5	2	13
Oversampling	6	6	6
Objective, Numerical aperture	4×, 0.13	4×, 0.13	4×, 0.13
Central Wavelenght [nm]	780	780	1300
Wavelength (nm)	800	800	1300
*axial resolution in air (µm)	4.5	2.17	5.5
*transverse resolution in the air (µm)	4.5		13

Table 1 represents the Gaussian and Bessel beam OCM system specifications and parameters.

3.1.4 Wavelength – swept-source laser OCM

The wavelength-swept source laser OCM (SS-OCM) system centred at 1300 nm was used as a light source with an A-line rate of 240 kHz [19]. The axial resolution of the system (in tissue) is 10 mm, and transverse resolution of 10 mm was achieved using 4× objective NA 0.13.

3.1.5 Critical hardware modules of OCM optical system

Camera: The Basler line scan camera was used for the acquisition of the spectral fringes, and Basler CCT+ software enables the following selection: Serial Baud Rate: 9600, Video data output mode: 4 Tap 12 Bit (CL medium configuration), CameraLink clock: 80MHz, Line acquisition mode: Line averaging, Exposure time control mode: ExSync, Edge controlled,

Shading mode DSNU: Shading correction. The light intensity in the entire range should be strong and uniform enough to be between 80% and 85% of the camera's sensitivity. The total number of camera points is 2048 pixels, and the acquisition speed is 100,000 lines/second.

Scanners: The galvanic scanners scan the reference beam and acquire the intensity values at each given scanning position of the sample. The operation of the scanners was controlled by analogue signals generated by an NI output card installed in the control computer. Triggering of the rotational motion of the mirrors in the scanners is synchronized with the detection system by a signal generated on the same output card triggering the operation of the NI frame grabber.

Light source: The described optical systems use a broadband light source (femtosecond laser, Femtolaser, Austria) with a central wavelength of 800 nm and 6fs pulse width for most of the experiments. The output power from the laser was set to be 4.5W for the laser operation. Thus, laser power is lost when travelled through optics, and final output power is optimized at resonator and measured by the power meter as 500 mW.

Gaussian and Bessel beam optical system: The essential components of the optical coherence microscope system for Gaussian and Bessel beam OCM shown in the home-built set-up in Figure 3-3 and Figure 4-4 are: broadband light source, interferometer, spectrometer, microscope, XYZ translation stage, sample mounting stage including ventilation, motion fixation for the mouse.

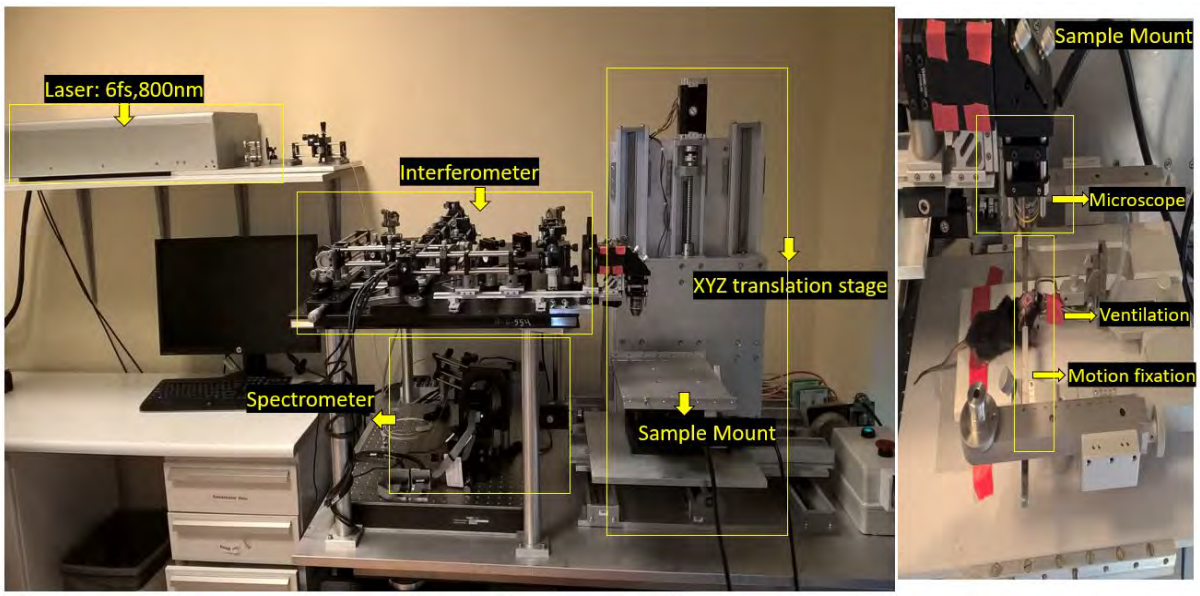

Figure 3-3 Home-built Bessel beam OCM (B-OCM): laser source, interferometer, sample mount, spectrometer, XYZ translation stage, microscope, motion fixation and, ventilation.

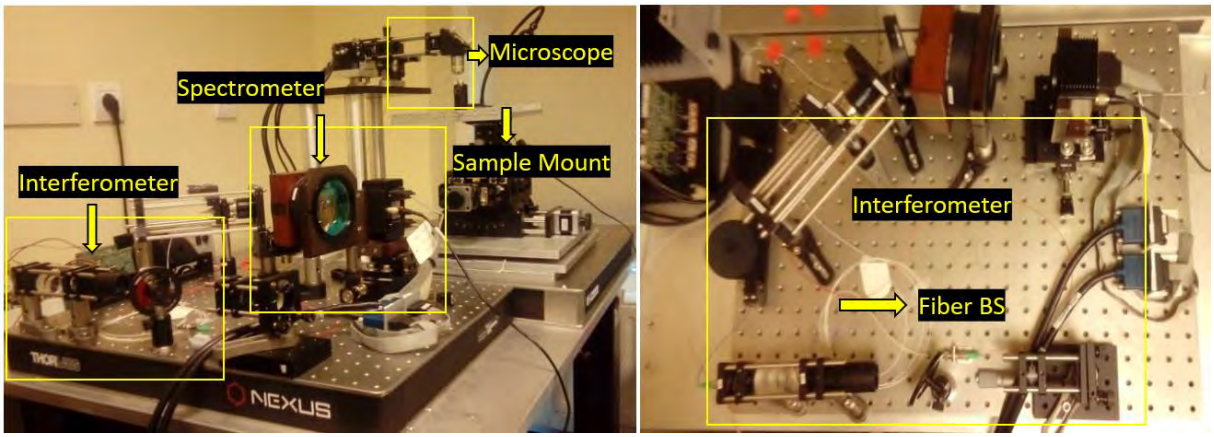

Figure 3-4 Home built Gaussian beam OCM (G-OCM): interferometer, fiber beam splitter (BS), sample mount, spectrometer, microscope.

3.1.6 Alignment and maintenance of OCM set-up

The LabView program was used to operate two modes: diagnostics and acquisition of the interferometric fringes to process, analyze, view, and save the data. It is essential to both calibrate and characterize the OCM system necessary for every measurement session. This enables to check the quality of the spectrum, interferometric fringes, signal to noise ratio (SNR) and the level of dispersion compensation. Due to the high sensitivity of both: the spectrometer and the laser to external conditions, it is necessary to adjust the system before each measurement series. For this purpose, it is first necessary to close the sample arm and check the spectrum's shape in the reference arm. The spectrum graph as a function of amplitude and pixel or distance should be smooth and wide, as shown in Figure 3-5(c), $x \in (0, 2048)$, $y \in (0, 4000)$.

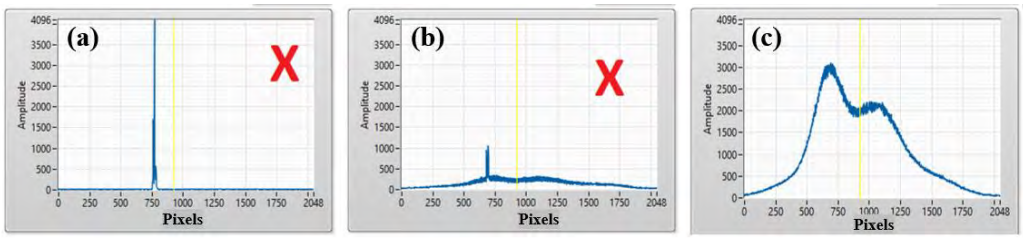

Figure 3-5 (a-b) graphs represent examples shape of the spectrum when the laser operates in non-stable mode – CW and partially mode-locked whereas (c) shows a smooth and wide optimized spectrum due to optimization camera position and mode-locking of the laser.

Finally, the object arm should be exposed, and the lens is aligned and adjusted for the maximum output intensity. The visibility of interference fringes was optimized in two ways within the sample positioned at the focal point of the lens using the LABVIEW program:

(i) Diagnostics: Raw spectrum graph, for the visible interference pattern, as shown in Figure 3-6(a) as a function of amplitude and distance and,

(ii) Acquisition: A-scans and B-scans charts as shown in Figure 3-6(b) and Figure 3-6(c), respectively, as a function of distance and amplitude for the visibility of image of the sample. The vital processing steps such as acquiring, process, control, calculations, and displaying the output of processed interference fringe data were performed.

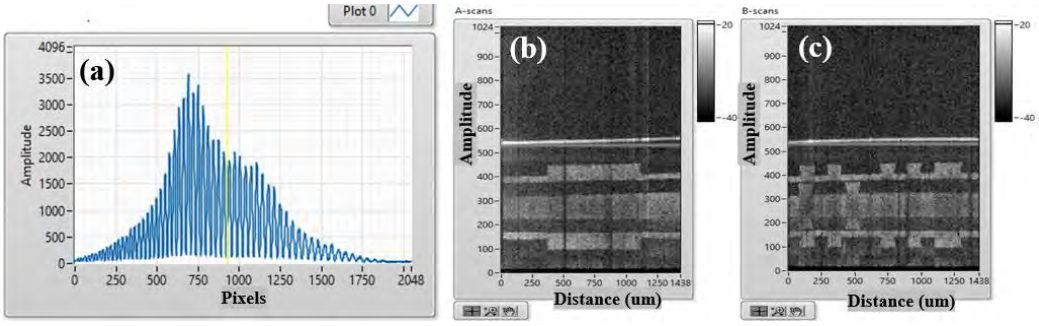

Figure 3-6 (a) The raw interferometric spectral signal obtained from the LABVIEW software by optimization of the system, (b-c) A-scans and B-scans obtained from the PDMS 3-D test phantom.

The spectrometer (line-camera) was adjusted with the use of a diagnostic part of the LABVIEW program. It enabled a real-time observation of the light spectra and interference spectra acquired from the spectrometer.

The spectrum acquired with the spectrometer was subjected to several additional steps before applying the numerical Fourier transform and consequently obtaining A-scans of the optical These steps include:

1. recalibration of the λ-k

2. removal of unbalanced dispersion in the interferometer arms,

3. numerical shaping of the spectrum,

The flow chart representing the important processing steps such as the parameters required to optimize the OCM system, the control and indicators used to calibrate the system, the acquiring the important elements for evaluating were shown in Figure 3-7 and the final computed and displayed output on the front panel were shown in Figure 3-8.

Dispersion compensation: The use of different optical components or different fiber lengths in the two arms of the interferometer results in a difference in dispersion introduced by these components. Uncompensated higher orders of dispersion (group velocity dispersion -GVD and higher orders) results in the introduction of a nonlinear frequency distribution of the spectral

fringe pattern and thus a significant broadening of the axial point spread function (PSF). Minimization of this unfavourable effect can be realized in hardware or software.

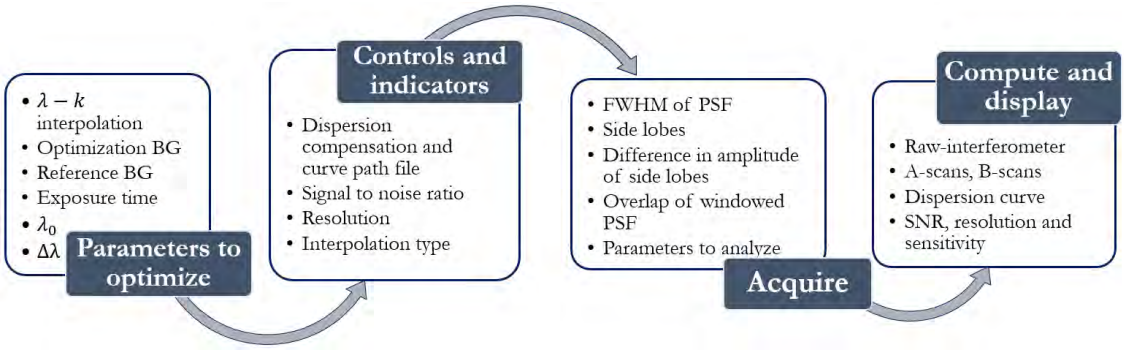

Figure 3-7 Flow chart represents the important processing steps such as parameters to optimize, control and indicators, acquire, compute, and display output for the LABVIEW software's diagnostic part.

Hardware minimizes the dispersion difference of the optical elements in the interferometer arms (by using a glass block or prisms). To conveniently observe the dispersion correction process, a dedicated functionality was introduced in software developed in LabView. For this purpose, the input fringe signal is divided into three signals by means of three Gaussian windows whose width and position on the spectral fringe signal are manually set. The overlap of the signals obtained by the Fourier transform of the windowed signals for any setting of the optical path difference (OPD) indicates a properly realized dispersion compensation.

Another way to compensate for dispersion is to numerically correct the phase of the spectral fringe signal performed in such a way as to achieve a single frequency in the benchmark fringe signal (measured for a mirror placed in the place of the object). In cases where only GVD is present, such compensation can be realized only by applying a single parameter chosen manually. In more complex cases, it is necessary to first measure the phase of the fringes with the effect of uncompensated dispersion. Then, a polynomial with a given number of orders was fitted and, after cutting off the constant and line components, the phase correction curve was obtained. [251] This curve can be saved on disk for the given interferometer system and later loaded into the data acquisition program. This correction function can be loaded, saved and accessed at any given time. This value is dynamic for every experiment, and it can be altered by measuring with respect to the experimental conditions.

Sensitivity: A Neutral Density (ND) filter was placed in front of the mirror in the object arm of the interferometer. This achieves realistic measurement conditions where the signal coming from the sample is much smaller than the signal from the reference arm. The maximum PSF

Max_{PSF} and the standard deviation σ of the noise are then identified on the A-scan. The sensitivity was calculated from the following formula:

$$\boldsymbol{Sens} = 20\,log(ND) - 20log\,(\frac{Max_{PSF}}{\sigma}) \qquad \textbf{3.1}$$

To properly interpret the determined sensitivity value, it is necessary to know the camera's exposure time and the optical power incident on the object.

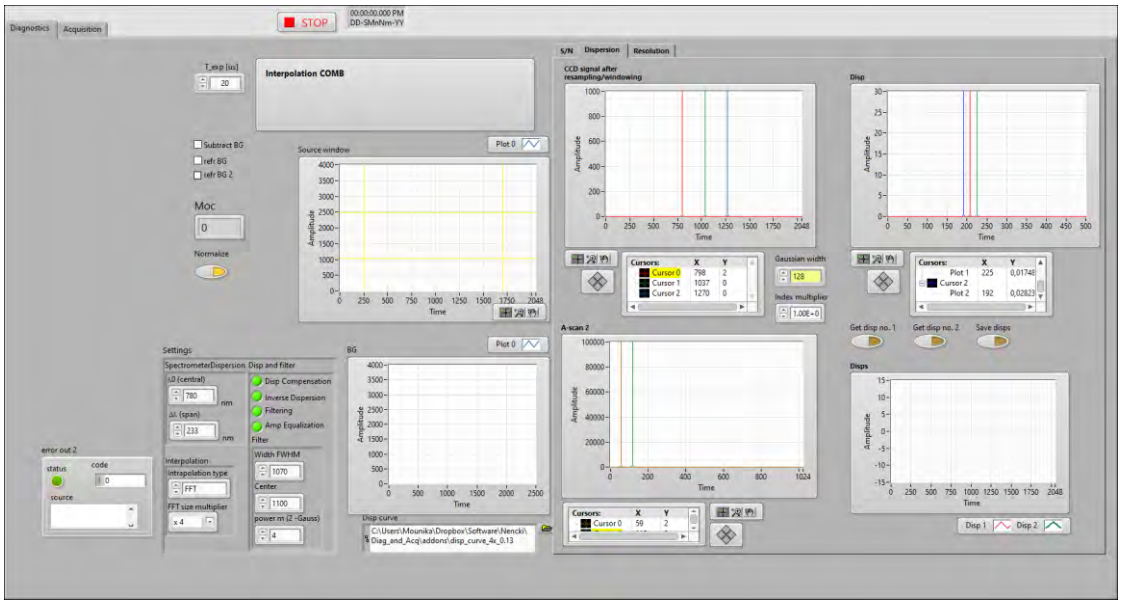

Figure 3-8 Screenshot of the diagnostic LABVIEW Program panel representing the parameters, settings and, display.

Resolution: The automatic processing tool calculates the full width at half maximum (FWHM) of the signal after Fast Fourier Transform (FFT) to determine the axial resolution of the system. This function is equivalent to the Point Spread Function (PSF). The full width at half maximum (FWHM) of PSF corresponds to the axial resolution of the OCM. The PSF should be symmetric, and the height of the side lobes should be less than -20 decibels (dB). The axial resolution of the imaging was calculated from the shape of the coherence function peak measured at the beginning and end of the measurement range. The program calculates the FWHM, the side lobes of the spectrum, the amplitude difference of the PSF side lobes. Other data processing steps such as background subtraction, spectral shaping are then applied to obtain the final results. A screenshot of the diagnostic portion of LABVIEW was shown in Figure 3-9.

3.1.7 Acquisition software

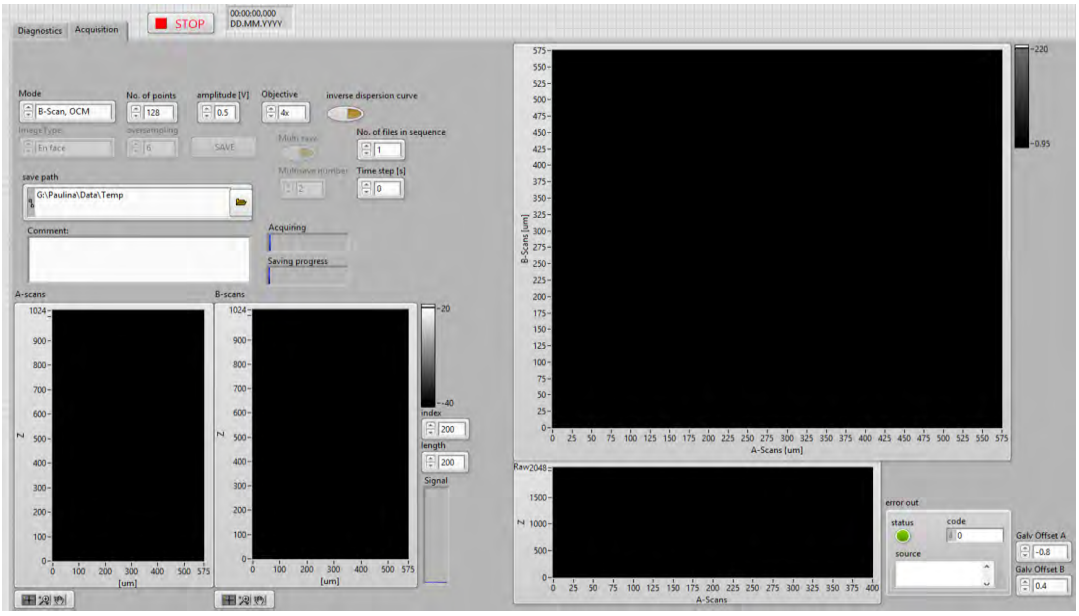

Figure 3-9 Screenshot of the diagnostic LABVIEW Program panel representing parameters data recording and of acquisition.

In addition to the maintenance software, there is also the software used to perform measurements (Figure 3-9). This software, also developed in LabView, has a minimized number of functions in the user interface in order to increase its ergonomics and facilitate the measurements. In the process of setting up the sample, it is important that the A-scan and B-scan can be displayed in real-time. The working or preview mode has a selection of four options: (i) "B-scan, OCM" mode for the cross-section preview of B-scan; (ii) "B-scan, Angio" mode for the preview of angiomap cross-section; (iii) "OCM" mode for the 3D object measurement and; (iv) "Angio" mode for the measuring and allowing to save data to the angiomap. The number of points (number of A-scans) are acquired in the X and Y axes, whereas the scans will be square. For angio functionality, the maximum number of A-scans in the B-scan are 800, when oversampling is 6. The scanning amplitude translates into the final pixel size and the scan area. Scanning amplitude is adjustable according to the lookup table linking the voltage set on galvo scanners and the physical distance travelled by the focused beam (Table 2).

Scanning amplitude and geometrical scanning span:

Amplitude [V]	10× NA 0.25 [µm]	4× NA 0.13 [µm]
0.1	58	144
0.5	288	719
1	575	1438
2	1150	2875
3	1750	4313

Table 2 Look up the table of scanning amplitude in volts (V) and their corresponding distance in microns (μm) for both 10x NA 0.25 and 4x NA 0.13 objectives.

The available important parameters displayed on the panel are: "A-scans", "B-scan, Angio", "Angio", "signals", and "raw interferometric spectrum" are described in Table 2. The number of repetitions of each B-scan (oversampling), scanning amplitude and the objective lens is the parameters set prior to the experiments. The objective lens magnification allows determining the pixel size.

Parameters	Description
A-scans	The section along the x-axis.
B-scans	Cross-section along the y axis.
Raw	Interference fringes
En-face	Illustrative image after analysis from the area declared in "Index" and "Length".
Signal	Auxiliary bar showing saturation of the camera detector

Table 2 Important parameters displayed in the LABVIEW software and their description

The image type: intensity and enface option can be chosen. The number of files to write and the "multi save" option is selected. The time steps or timestamp represents the number spacing between files. If the multi save option is selected, the time interval is between the multi save series - the auxiliary image shown in Figure 3-9.

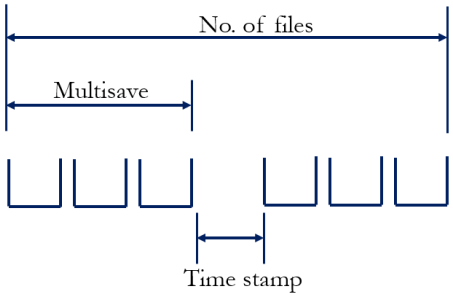

Figure 3-10 shows the representation number of files and the time stamp in multi save acquisition.

The status bar indicates the progress of the measurement process. The important processing steps, such as the preview mode options, the graphs displayed on the panel, the parameters to be adjusted, and the output image type, along with the option to save to multiple files, are shown in the flowchart in Figure 3-11.

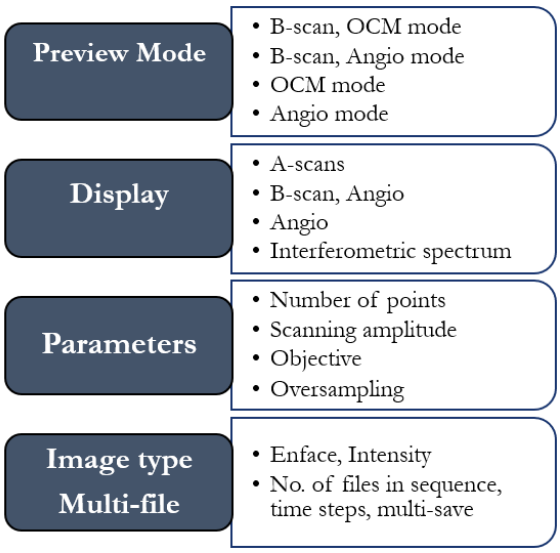

Figure 3-11 Flow chart representing the vital processing steps such as parameters for the preview mode, the display options, parameters, image type and, multifile controls.

The image parameters can be changed, and the save option allows to save of the data. The file save path will recursively check if the current date is in the path, and if not, it will create a folder with the date. A comment field will be placed in the header of the file(s).

3.1.8 Software for angio processing

The output source file with information such as A-scan, B-scan, oversampled B-scan and, pixels obtained from the acquisition software was taken as input source files for Labview software for angio processing. Important steps of angio processing such as source file input, tilt compensation type, motion correction methods, data reordering, angiographic algorithms, motion and intensity averaging, display and save options in LABVIEW software are shown as a flow chart in Figure 3-12. All these steps are to obtain an angiographic map of cerebral blood flow.

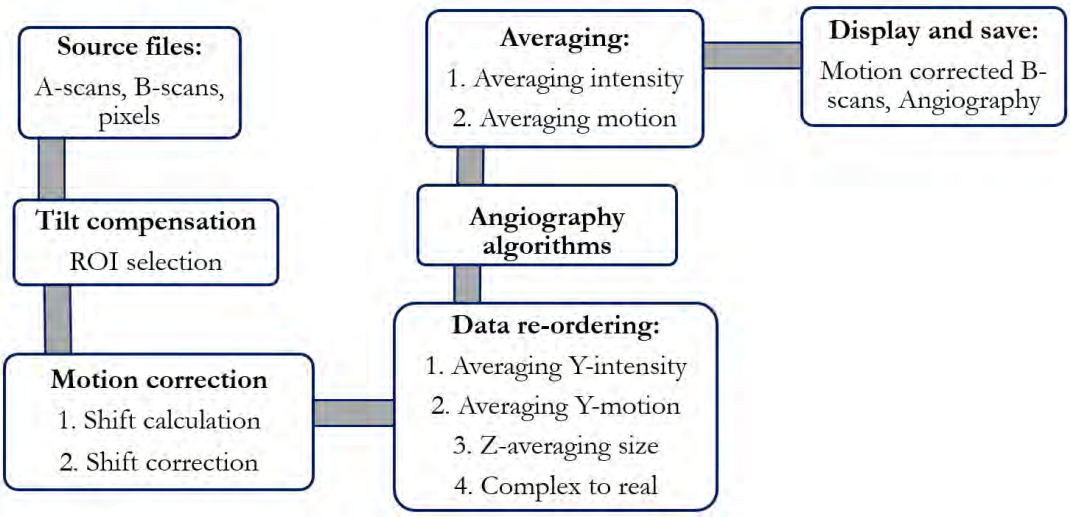

Figure 3-12 The vital processing steps are represented in the flow chart for the angio processing of LABVIEW software.

The tilt correction of the brain tissue is performed using "TiltComp" and "Reverse" (when the tilt increases instead of decreasing). The correction was optimized by changing the spacing of the yellow bars from the left graph to select the tilt region, as shown in Figure 3-13. The region of interest (ROI) for angiography was selected from the panel showing the corrected data on the right. The oversampling of the acquired B-scans can average the structural B-scans or contrast the motion in a selected ROI set using the length and index parameters. The motion correction option provides suppression of motion artefacts due to mouse heart and breathing activity using offset calculation and offsets correction methods. The motion correction algorithms use a combination of bulk image shift (BIS's) and global phase fluctuation (GPF's) methods in the axial or lateral direction [206]. The intensities of the acquired motion-corrected B-scans are normalized. Data ordering includes X and Y intensity averaging and allows the selection of one of the averaging methods: maximum, minimum, mean, variance, skewness, kurtosis, and correlation coefficient for the acquired B-scans in the scan. It also allows selecting the polynomial order, averaging Z (phase variance), and changing the signal's intensity value from the composite signal to the real signal using frame merging methods. Information on flows is obtained by means of four important angiography algorithms: absolute complex difference [93], absolute intensity difference [93, 192], phase variance [98, 193] and, speckle variance. [184]. The absolute complex difference was the best method suitable for this purpose and was chosen to process and visualize the microcirculation map in the mouse brain.

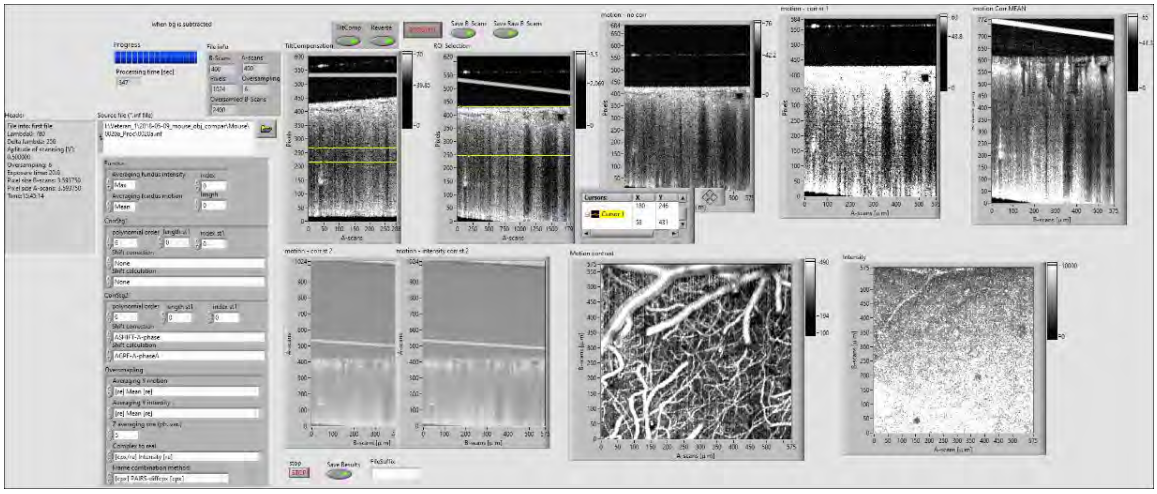

Figure 3-13 The screenshot of the user interface of the angio processing tool.

The average of all obtained B-scans with motion correction for both intensity and flow B-scans was calculated. The data analysis was defined by selecting the appropriate parameters and functions, and the program creates a file with the extension _ang. int containing the intensity information and; the final results displayed and images saved are intensity B-scans, the angiographic image of B-scans contrasted by motion, and a screenshot of the panel. The "Save Results" button allows you to save the images, while the "STOP" button allows you to stop the data analysis.

3.1.9 Software for data visualization

The entire three-dimensional (3D) angiographic data set is visualized using LABVIEW data visualization software. After starting the software, a path file was selected into which "motion B-scans" obtained from the angio software are loaded. The Save button saves the image with the "Amplitudes" and the movie with the parameters declared in the "Flight-through settings" if the "Movie" option is selected. The program collects the images and saves them to a file with the extension _movie.avi. The frame rate is 5. To select or change the file, specify the path to the source file, which this option allows, and the program will automatically load the new file. B-scan number, the current section, is displayed on the "B-scan" option. For flight through the film, parameter settings are as follows: frames created from "start index" to "stop index" with a "step", where the step averaged is the "Average length" and the number of cross-sections in the Z direction (see auxiliary x-y-z figure). For the width option, there is a possibility to change the position of cursors on "B-scan", which affects the image presented in "Amplitudes". The scale option in decibels (dB): linear scale (lin) or logarithmic scale (ll) was used to change the display of data in "B-scan" and "Amplitudes" according to the formula ln = 20 * log10 (lin). When

fixed width is selected, the distance between cursors is declared in the "Width" field and takes a fixed value. A simple stripping algorithm for reducing vertical stripes that come from animal movements.

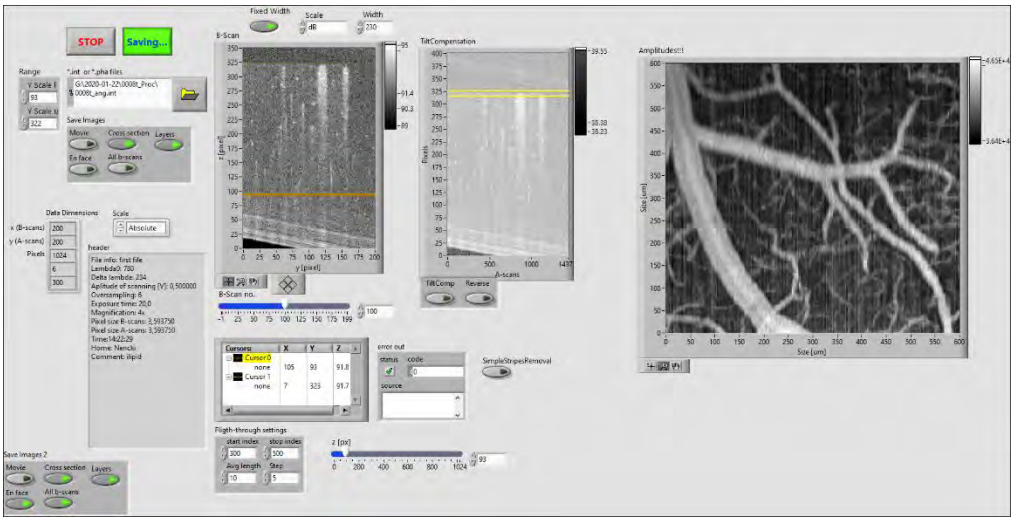

Figure 3-14 The screenshot of the LABVIEW program for the 3-D data visualization.

3.2 Scanning Protocols

The scanning protocols were used for the 3-D acquisition of angiomaps for both Bessel and Gaussian beam OCM. The X and Y scanners of the galvanic mirrors acquire voltage signals. When one of the two scanners are moved in unidirectional or bidirectional fast enough to acquire the cross-sectional OCM images or B-scans is called the fast axis or A-scan, as shown in Figure 3-16(a). When the second scanner moves slowly in the direction perpendicular to the fast axis is defined as the slow axis, as shown in Figure 3-16(a). The 3D OCM data set consists of the subsequent B-scans acquired along the slow axis. The oversampling parameter is defined as the number of repetitions of the same line, as shown in Figure 3-16(b), and the camera's speed sets the total acquisition time of the data. The scanning protocol used for the current experiments: Each B-scan was divided into segments, and each segment at a given horizontal position was scanned several times, and then the segmented B-scans are acquired for all the vertical positions of the ROI of the brain tissue (similar to raster scanning). The number of A-scans acquired per segment, and the number of segments in a B-scan (oversampling) can be adjusted and varied in the scanning protocol depending on the image ROI.

In the case of Gaussian beam OCM, three-dimensional volumes with a maximum field of view (FOV) of 2.8 × 2.8 × 2 mm^3 containing 800 × 800 × 2048 pixels sampling density with X, Y, and Z-axis, respectively. For the better visualization of ROI, the FOV with 1.7 mm x 1.7 mm

x 0.4 mm with a sampling density of 400 × 400 × 400 pixels was selected. The B-scan oversampling of 6 is used to average and improve the quality of calculating the OCM B-scan angiographic images with a repetition time of 8.2 ms. The time for the acquisition of full 3D volumes collected is 19.2s, but the total measurement time (including both data transfer and saving) was 94s. The stand-alone LabView software allows to control the scanning protocols, synchronization of camera and scanners, and data pre and post-processing.

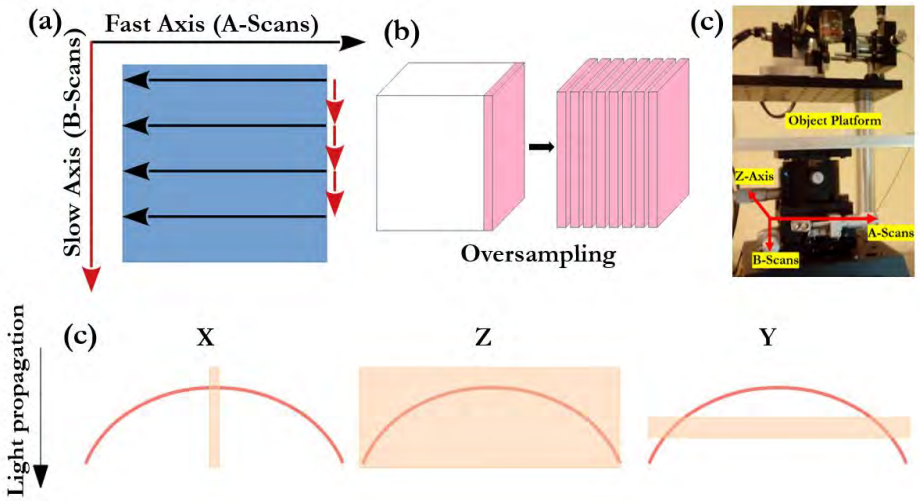

Figure 3-15 Scanning protocols representing (a) fast axis and slow axis (b) oversampling (c-d) sample platform with X, Y, Z degrees of freedom.

In the case of Bessel beam OCM, the scanning protocol includes 300 A-scans × 300 B-scans × 2048 pixels with a maximum field of view (FOV) of 1.1 × 1.1 mm^2. The number of repeated B-scans of 6 with a repetition time of 20 µs for every A-scan. The speckle decorrelation analysis was used to obtain angiographic images. The time for the acquisition scanning of the sample is 9.7s, but the total measurement time (including both data transfer and saving) was 184s. The stand-alone LabView software allows to control the scanning protocols, synchronization of camera and scanners and, both data pre and post-processing.

3.3 Post-processing methods

The series of adjacent motion B-scans images (stack) acquired in the scanned area of the brain tissue are used as the input file for further post-processing to achieve a high-quality enhanced microvasculature for further quantitative and qualitative analysis. The small de-correlation between the motion B-scans is corrected using automatic registration: rigid body transformation method, where the distance are conserved between any pair of points [252]. The histogram equalization method enhances signal in the deeper regions of the tissue [253]. Finally, the stack

of motion B-scan images was converted to angiography. The background subtraction was made to remove the noise from the signal in the image. Later, the angiography stack was achieved by the orthogonal reconstruction of the volume of B-scan image stacks. The Frangi-Hessian filter based on obtaining the eigenvalues in the Hessian matrix is applied to the angiography stack with an appropriate sigma value (radius of the vessel) to recover, detect and trace only the vasculature structure [254]. The ROI with good signal quality is chosen and segmented using depth segmentation prior to averaging the stack of angiography images to achieve a fair resolution of vessels.

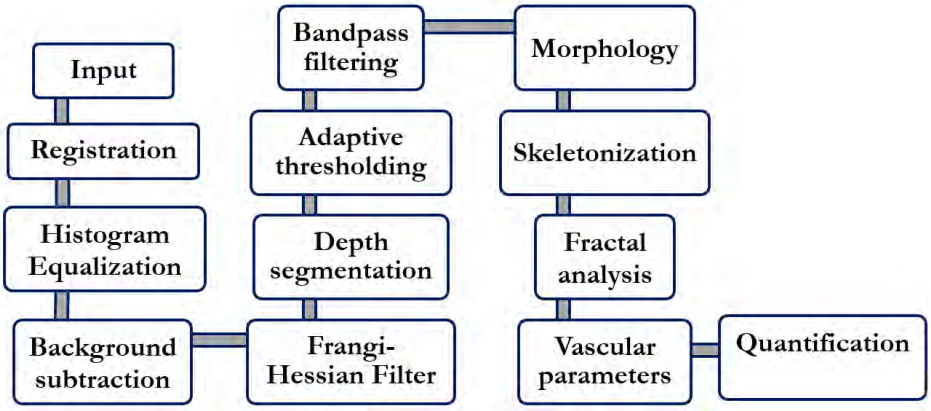

Figure 3-16 The flow chart representing the post-processing steps to achieve an enhanced brain microvasculature.

The global adaptive thresholding was applied with a binary image output representing the segmentation. In this method, the threshold for each pixel in the image was calculated, and if pixel value falls below the threshold, it set to the background value. Otherwise, it takes as foreground value [255]. The fast Fourier transform (FFT) bandpass filter function was used to suppress the horizontal and vertical stripes caused due to the motion of the small animal, and then the angiography image is inverse fast Fourier transformed to get an artefact-free image. The morphology analysis segments the morphological features using morphological operations, such as morphological gradient and extended minima with watershed flooding algorithms [256]. The skeletonization of the angiography image was used to binarize the image, extract and analyze the skeleton for further quantification. The fractal analysis, a contemporary method using Euclidean concepts to understand the patterns, measures the complexity using the box-counting method and obtains the fractal dimension (FD). The FD further helps to quantify the vascular parameters such as vascular density metrics: vascular density (vessel area/total area), vascular length density (skeletonized vessel area/total area), branching index (branch points/unit area), vessel length, the number of vessels and lacunarity [257].

3.4 Animal handling

In our studies, we had the dura matter kept intact with the brain using the cranial window method, whereas, in most studies, it was removed to increase depth resolution. It can provide optical access for the wide information spectrum such as functional, neuronal, vascular, glial, and other metabolic parameters to investigate both pathophysiological and physiological mechanisms. The OCM-A technique with transcranial window implantation for the in-vivo cerebral microvasculature handles most imaging limitations compared to other modalities. It can be performed in a non-contact mode with a low risk of damage and does not have adverse effects on the tissue in the limited course of the experiment.

All new methods related to work on animals as well as procedures and surgeries were invented and performed by our collaborators from the Nencki Institute of Experimental Biology of the Polish Academy of Sciences: Monika Malinowska, PhD and Hubert Doleżyczek, MSc. All procedures were performed in accordance with the principles established by the First Local Ethical Committee for Animal Research in Warsaw. All procedures adhere to the national and international laws and provisions regarding the protection of animals. In particular, all animal experiments will be performed by authorized personnel under the rules of each given country according to EC Directive 86/609/EC. Animals will be housed and cared in professional animal facilities and they will be provided with food and beverage ad libitum and will be placed in proper cages with adequate bedding. Research and housing of animals is conducted according to the EU directive 86/609/EC, regarding the protection of animals used for experimental and other scientific purposes.

3.4.1 Mice preparation

C57/Bl6 male mice of 25-30 grams were anaesthetized with 2% isoflurane, and the skull was removed through the surgical procedure. Later, the cranial window was installed on the dura near the right somatosensory cortex, and a coverslip of 4 mm diameter was used to cover the dura, and later a metallic frame was fixed to reduce the motion artefacts using dental cement. The mice were immobilized using a stereotaxic frame to reduce the bulk movements of the mouse, and it was placed on the motorized stage located under the optical coherence microscope setup. The artificial cerebral spinal fluid (ACSF) is applied around to match the brain and air concentration. The dental cement was used to seal the coverslip to the brain and metallic frame around the cranial window. The rat is allowed to rest for 20-30 min for recovery before imaging.

3.4.2 Rat preparation

An Albino male rat of 280-320 grams and 8 weeks old were anaesthetized with 2-3% Isoflurane. The cranial was made around the skull with dura intact, and a glass coverslip and dental cement are used to glue it around the brain surface. The lidocaine was used as a local anaesthetic during the surgery, and heparin solution was used initially during surgery to prevent coagulation. The mouse is placed on the sample stage with a heating pad underneath to prevent variations in physiological conditions and movements. The eye ointment was used to prevent the eyes from drying during surgery. The agarose solution was used to match the refractive index between the brain-glass surface before sealing the cranial window. The artificial cerebral spinal fluid (ACSF) was applied around match the brain and air concentration. The rat is allowed to rest for 20-30 min for recovery before imaging.

3.4.3 Glioblastoma preparation

The cranial was prepared 14 days earlier to inject tumour cells to give the time to heal and reduce inflammation and recovery due to surgery. A group of four C57/Bl6 male mice (N = 4), each weighing about 30-40 grams, out of which three were injected with GL261 ~5000 tumour cells and one with saline(control) into the somatosensory cortex region of the mice brain and used as a control mouse. The mice were under veterinary care and given anti-inflammatory drugs and analgesics. The murine models of primary human glioblastoma were generated through the direct injection of ~5000 tumour cells, line GL261 head immobilized to keep brain motionless injection with a power of 1.9 mW objective of 10× and NA 0.13 of U87MG cells into the brain parenchyma of mice, after which cranial windows were affixed to the exposed tissue to facilitate imaging. The cranial of mice prepared were imaged after 7-8 days. The tumour was injected into three different mice, and the progression was acquired for 1,3,7,9,11 and 14 days with FOV of angiography 1.4 × 1.4 mm. The angiographic and intensity images were processed, and the volume of the tumour was clearly visualized. The difference between healthy and tumor mouse was clearly visualized in vessels' tortuous, irregular nature during progression. Nevertheless, there is a need for consistency, proper focusing and repetitive measurements. So, the measurements were performed by optimizing all the parameters to achieve the best quality results.

3.5 Preparation of contrast agents

3.5.1 Microfluidic channel fabrication

The microchannel system was prepared in Prof. Garstecki's laboratory at the Institute of Physical Chemistry of the Polish Academy of Sciences. The microfluidic chip was fabricated in three steps. Firstly, the channels were milled in a polycarbonate (PC) plate using a CNC machine (MSG4025, Ergwind, Poland). In the second step, the liquid polydimethylsiloxane (PDMS) was poured onto the PC chip. After polymerization at 75°C for 1 hour, the surface of PDMS mold was activated by Laboratory Corona Treater (BD 20AC, Electro-Technic Products, USA) and salinized in the vapours tridecafluoro-1,1,2,2-tetrahydrooctyl-1-trichlorosilane (United Chemical Technologies, USA) for 30 min under 10 mbar pressure. The PDMS mold was filled with a fresh portion of PDMS in the third step, polymerized at 75°C for 1 hour, and finally bonded to a 1 mm thick glass slide using oxygen plasma. The hydrophilicity of the microfluidic channels was provided by introducing modifying solution and baking the chip overnight at 75°C. Each microfluidic channel consists of three regions, which dimensions we specified using a Bruker contour GT-K optical profilometer (Bruker, USA). The channels are squares in cross-sections, so the size inspection was focused in one direction. The depths of the most miniature, middle and widest parts are 63, 144, and 243 um, respectively (Figure 3-16).

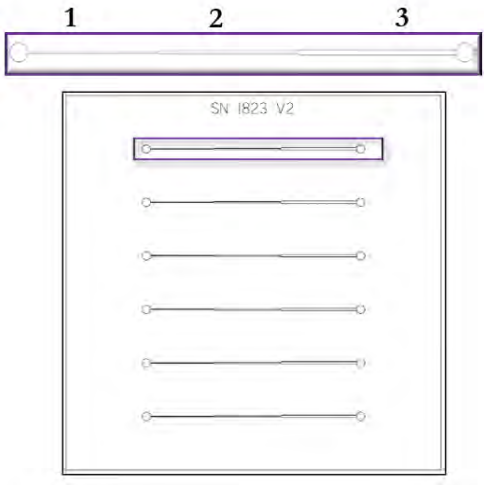

Figure 3-17 The microfluidic channel with the different channels for the experiments with LGNRs in water. The top part of the figure shows the varied thickness for different channels (1,2,3) from small to large or increasing order.

The microfluidic chip with the three channels on a polycarbonate (PC) plate with different thicknesses and depths: the smallest part: 63 µm, the middle part: 144 µm and the biggest part: 243 µm are represented in Figure 3-18 and Figure 3-19.

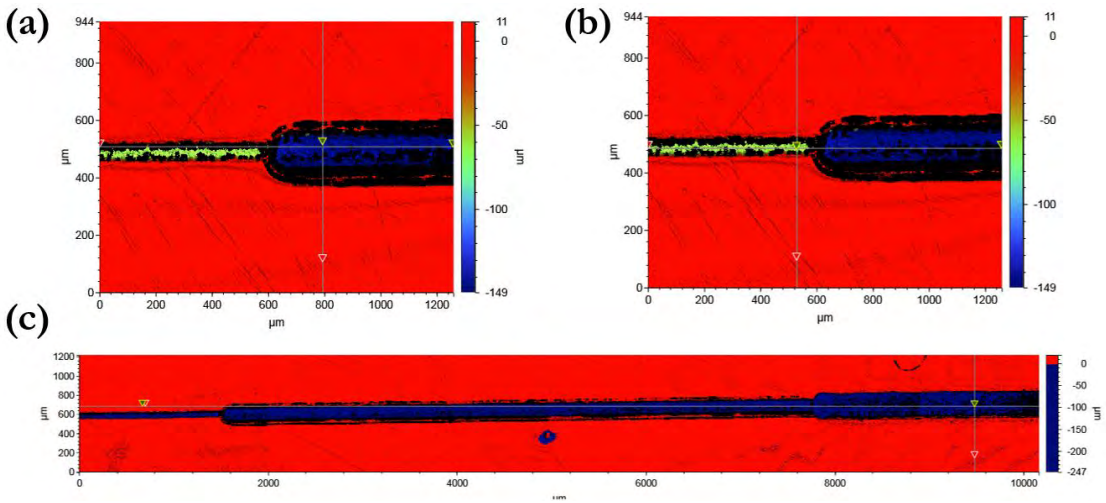

Figure 3-18 The microfluidic channel representing the depth of the smallest channel, medium channel, and large channel, with the vertical line showing the position of the channel.

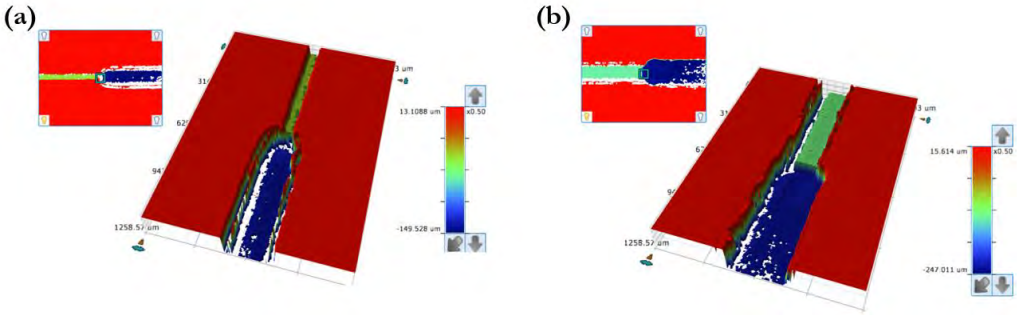

Figure 3-19 shows the depth profiles of the middle and the largest part of the microfluidic channel.

3.5.2 Preparation of Large Gold nanorods (LGNRS)

Nanoparticles for the research presented here were prepared in the laboratory of Prof. Joanna Niedziolka-Jonson from the Institute of Physical Chemistry of the PAS.

Synthesis: Gold nanorods (AuNRs) were synthesized using the seed-mediated growth method. The modified literature procedure was adopted from the Murray group [258]. First, the seeds solution was prepared by reducing a mixture of 5 mL 0.5 mM HAuCl4 and 5 mL 0.2 M cetyltrimethylammonium bromide (CTAB) solution with 1 mL fresh 0.006 M $NaBH_4$ solution. The solution colour was changed from yellow to brownish-yellow, and after vigorous stirring for 2 min, the seed solution was aged 30 min before use. Next, the growth solution was prepared by dissolving 7 g CTAB and 1.2993 g potassium oleate in 250 mL warm water (50 °C). After the growth solution was cooled down to 30 °C, 18 mL 4 mM $AgNO_3$ solution was added. The mixture was then kept undisturbed for 15 min at 30 °C. Then, 250 mL 1 mM $HAuCl_4$ were injected and stirred for 90 min; in the next step, 2.1 mL 37 wt. % HCl was added and slowly

stirred for 15 min. The final step was to inject 1.25 mL 0.064 M ascorbic acid with stirring for 30 s. Finally, 0.4 mL seed solution was added into the growth solution and stirring for 30 s. The resultant mixture was allowed to grow at 30 °C for 12 h without stirring. The gold nanorods (AuNRs) were concentrated using centrifugation at 5500 rpm for 20 min. The bio-functionalization of mPEG-LGNRS is obtained [158].

Materials: All chemicals are obtained from commercial suppliers and used without further purification. The hexadecyltrimethylammonium bromide (CTAB, > 98.0%), potassium oleate (KOL, > 98.0%), L-ascorbic acid (BioUltra, ≥ 99.5%), silver nitrate (AgNO3, >99%), sodium borohydride (NaBH4, 99%) and hydrochloric acid (HCl, 37 wt. % in water) were purchased from Sigma Aldrich. Whereas the hydrogen tetrachloroaurate trihydrate ($HAuCl_4 \cdot 3H_2O$) were purchased from ABCR company. The water was purified with an ELIX system (Millipore). All glassware was cleaned using freshly prepared aqua regia (HCl: HNO_3 in a 3:1 ratio by volume), followed by rinsing with copious amounts of water.

UV-VIS analysis: All the ultraviolet-visible (UV-VIS) spectra have been collected with Thermo Evolution 300 Spectrophotometer at room temperature. The extinction spectra were recorded using a glass cuvette with a 1 cm optical path length. The spectra were measured in the range 400-1100 nm with a bandwidth of 2 nm and the scan speed 60 nm/min.

Figure 3-19 represents the scanning electron microscope (SEM) images (left) and UV-VIS spectrum (right) obtained for LGNRs and mPEG-LGNRS at 990 nm. The size of the LGNRS is estimated to be 95 nm x 14 nm, $V_{nanorod} \approx 18488.42\ nm^3$, $R_{eff} = 16.41$ nm, $\varepsilon \approx 1 \times 10^{10}$. The concentration (diluted sample): $3{,}17272 \times 10^{-11}$ M and the concentration of the main sample: $5{,}64039 \times 10^{-9}$ M.

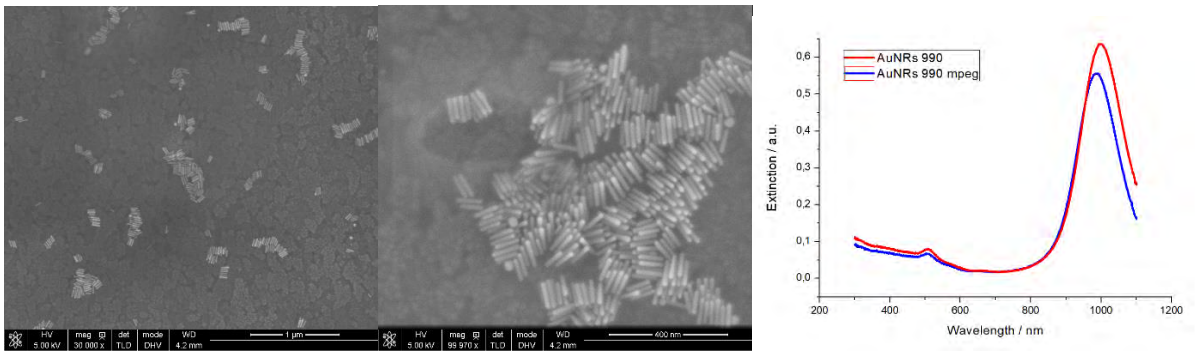

Figure 3-20 The SEM images (left side) and the UV-VIS spectrum (right) of the obtained both LGNRs and mPEG-LGNRs at 990 nm wavelength.

The Figure 3-20 represents the scanning electron microscope (SEM) images (left) and UV-VIS spectrum (right) obtained for LGNRs and mPEG-LGNRS at 670 nm. The size of the LGNRS is estimated to be 77.4 nm x 25.8 nm, $V_{nanorod} \approx 29209.28\ nm^3$, $R_{eff} = 19.10$ nm, $\varepsilon \approx 1.5 \times 10^{10}$. The concentration of the diluted sample: 1.12×10^{-11} M and the concentration of the main sample: 2.0×10^{-9} M.

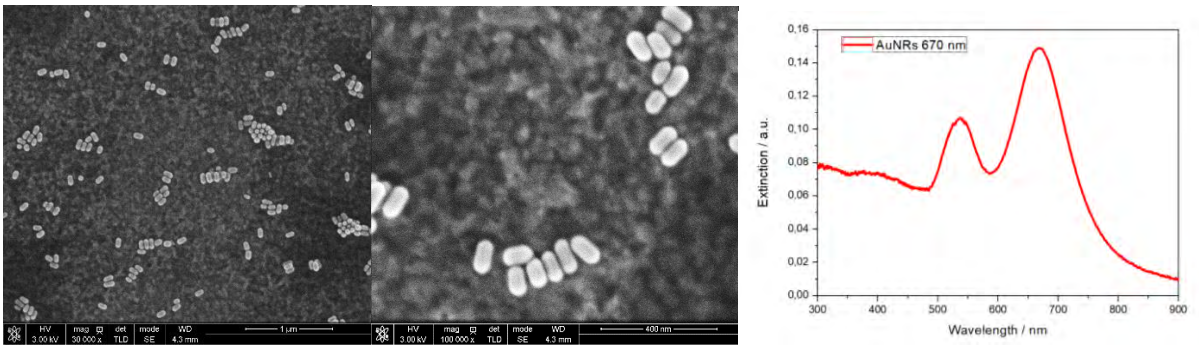

Figure 3-21 The SEM images (left side) and the UV-VIS spectrum (right) of the LGNRs obtained at 670 nm wavelength.

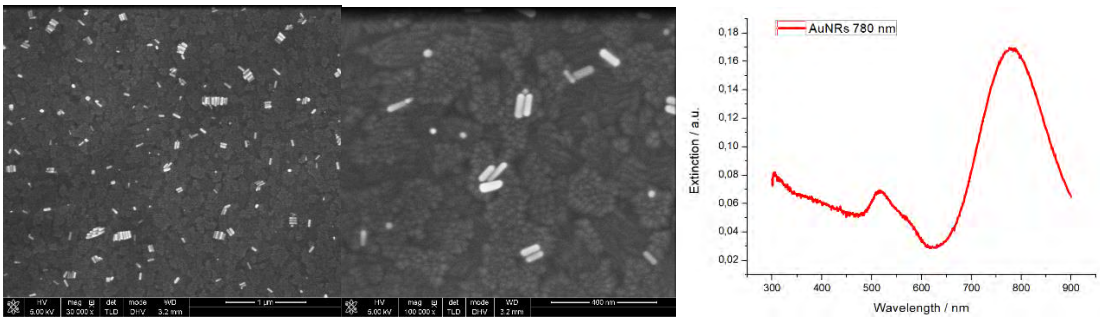

Figure 3-22 The SEM images (left side) and the UV-VIS spectrum (right) of the obtained both at 780 nm wavelength.

The Figure 3-21 represents the scanning electron microscope (SEM) images (left) and UV-VIS spectrum (right) obtained for LGNRs and mPEG-LGNRS at 780 nm. The size of the LGNRS is estimated to be 116.4 nm x 58.2 nm, $V_{nanorod} \approx 244918.96\ nm^3$, $R_{eff} = 38.81$ nm, $\varepsilon \approx 3.75 \times 10^{10}$. The concentration of the diluted sample: 3.97×10^{-12} M and the concentration of the main sample: 5.3×10^{-11} M.

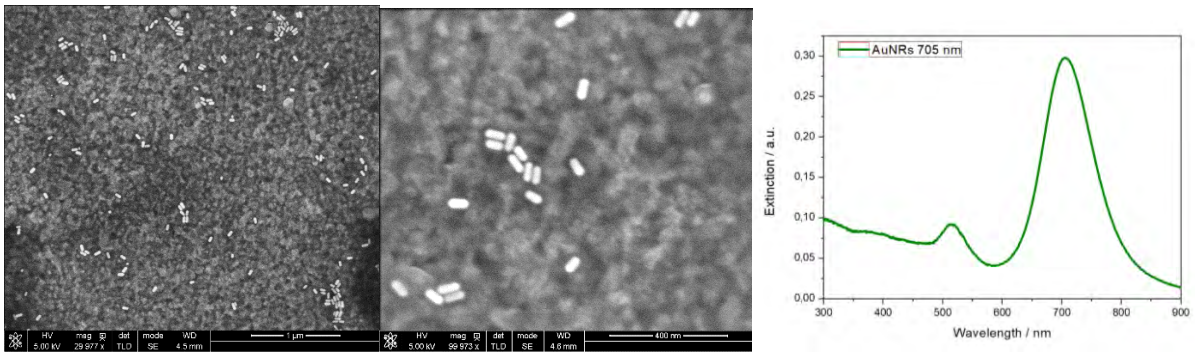

Figure 3-23 The SEM images (left side) and the UV-VIS spectrum (right) of the obtained both at 705 nm wavelength.

The Figure 3-22 represents the scanning electron microscope (SEM) images (left) and UV-VIS spectrum (right) obtained for LGNRs and mPEG-LGNRS at 780 nm. The size of the LGNRS is estimated to be 65.5 nm x 29.1 nm, $V_{nanorod} \approx 35444.25$ nm^3, $R_{eff} = 20.38$ nm, $\varepsilon \approx 1.5 \times 10^{10}$. The concentration of the diluted sample: 1.99×10^{-11} M and the concentration of the main sample: 263×10^{-10} M.

The Gold nanorods-CTAB (without modification with mPEG) samples synthesized are very stable. The colour of the solutions is bright red. The band's positions (514 and 805 nm) are exactly at the same wavelengths. It confirms that bare AuNRs are very stable and can be stored at room temperature for months without changing shape. The AuNRs cannot be stored longer than 3 weeks since the final stability of particles will depend on many factors like synthesis method, purity of reagents, storage conditions, etc., but these are very promising for future studies on GBM. Directly after preparation, AuNPS-PSS-mPEG are blue-shifted on the longitudinal band (802 nm), and the transverse band remains in the same wavelength (514 nm). The FWHM is the same as before modification. There is no aggregation or change in the colour of the solution. After almost 30 days, blue-shift increase on AuNRs-PSS-mPEG (763 nm). Additionally, the transverse band starts to change due to this big blue shift on the longitudinal band. The FWHM is the same for that blue shift as before/before modification. There is no aggregation, and the colour of the solution is a bit different comparing to bare AuNRs. Because PSS stabilize the longitudinal faces and the mPEG is attached to the caps, from UV-vis, we can notice that rods start to change their shape and shorten their length. It means, AuNRs-PSS-mPEG has to be used in the next step as soon as possible, so we can decrease the concentration of mPEG for the next modification to improve their stability.

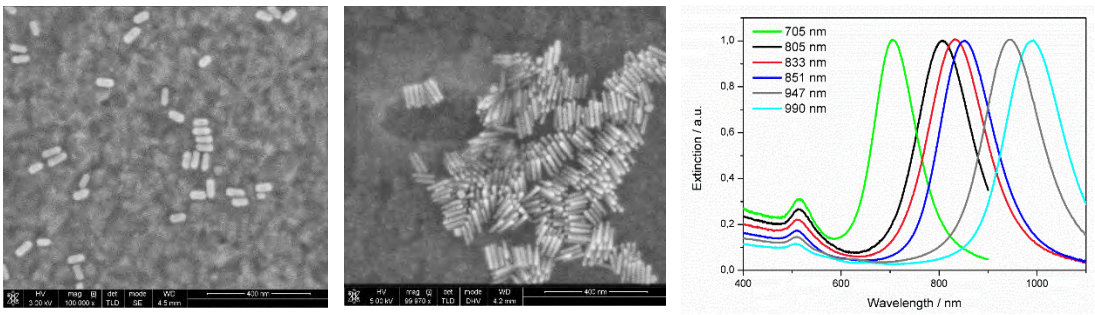

The LGNRs were synthesized of size ~110 × 30 nm in measured by scanning electron microscopy (SEM), and they exhibited a peak longitudinal surface plasmon resonance (LSPR) at 802 nm. To test the improvement in the optical signal from OCM we tested initially in water. The important parameters for choosing the LGNRs for in-vivo measurements are the non-

toxicity, scattering wavelength and biostability. So, LGNRs are commonly coated with thiolated poly(ethylene glycol) (PEG-SH) reagents, methoxy-PEG-SH and incubation of LGNRs with poly(sodium 4-styrene sulfonate) (PSS) produced particles (LGNRs-PSS). These are stable in both DDI H_2O and FBS_20. PSS is safe for in vivo studies. Finally, we obtained the LGNRs-PSS with methoxy-PEG-SH and washed them to produce LGNRs-PSS-mPEG to ensure biocompatibility and nontoxicity. The LGNRs-PSS-mPEG produced enough backscattering to provide strong contrast enhancement in water. The size were 106 nm x 30 nm with the aspect ratio: 3.5, and the main peaks from UV-vis spectroscopy are 805 nm and 514 nm, the $V_{nanorod} \approx 41901.16$ nm^3 and the $R_{eff} = 21.55$ nm with extinction coefficient $\varepsilon \approx 3.5 \times 10^{10}$. The main concentration of the stock solution obtained is 2.61 x 10^{-7} M. The monodisperse gold nanorods can be synthesized with different aspect ratios, and the optical properties of gold nanorods were tuned via a controllable experimental route. The biofunctionalization of gold nanorods makes them stable and suitable for medical applications. The high tumour penetration capability of biofunctionalized gold nanorods and the high cellular uptake makes them an excellent optical agent for imaging by OCM. The enhanced scattering of biofunctionalized LGNRs was used to image small blood vessels. The contrast enhancement achieved with our method allowed us to monitor the contrast enhancement.

3.5.3 LGNRs and LGNR-PSS-mPEg experiments in water and mice:

The bare LGNRs and LGNR-PSS-mPEg were injected into a microfluidic device of a 200 × 200 μm channel. The measurement of water alone was taken to subtract the contribution later. They were starting from the low concentrations 1femtomolar (fM) the incremental steps of 10-15 measurements up to 10 nanomolar (nM) were injected. Every time the microfluidic channel was cleaned with water to ensure the right concentration and remove the leftover LGNRs from the previous injection. The OCM signal vs concentration graph clearly shows the increase in the OCM signal by almost four orders of magnitude for higher concentration. This graph also agrees with the literature [259]. We assume that the same trend applies to the measurements of LGNRs in blood. We predicted that the same parameters and square root regime would provide a good prediction for in vivo data. We injected intravenous injections into the living mouse near the neck vein. Each mouse was anaesthetized with 2% isoflurane and a total of 400 microlitres (μL) of 23.5nM LGNRs. We performed a second injection to the right ear pinna and mouse brain with cranial window, and the data was acquired. Before and after incremental injections, the representative OCM images were prominent in water, and we did not yet observe a huge difference in angio. This could be that concentration was too low for enhancement or the

circulation time and the acquisition time did not fit in the regime. The study of LGNRs in water at different concentrations detailed studies on both on and off-resonance wavelengths.

3.5.4 Intralipids

Materials: The samples were prepared from a 1000 ml intralipid aqueous suspension containing purified soybean oil (100 g), purified lecithin (12 g), and glycerin (22 g). This 10 % intralipid solution (with a concentration of 100 mg/l) was diluted with distilled water to obtain samples with concentrations from 1 % to 10 %.

3.5.5 Intralipids experiments with the in-vivo mouse:

For the mouse experiments, the intralipid of 300µL was injected into the mouse brain through an intracarotid vein - neck vein injection. The total time of injection was 1 minute. The mouse was imaged during and after injection of intralipid. The mouse is allowed to rest for 20-30 min for recovery before imaging.

For the rat experiments, the first injection of 500 µL intralipid was injected into the rat brain to focus on the superficial and deeper vessels through direct neck vein injection through a catheter. The mouse was imaged during and after injection of intralipid. The second dosage of injection was given after 10 min with the focus on the deeper cerebral microvasculature. The total time of injection was 1-2 minutes for both the injection. The small animal was scanned for 1-4 minutes, and simultaneously to OCM data was acquired.

Chapter 4 Results

4.1 Test measurements on mouse brain using OCM

The standard Gaussian and Bessel OCM setup is home-built based on the Michelson and Mach Zehnder interferometers, respectively, to quantify the tissue properties for evaluating changes in morphological, structural and pathological characteristics. It aids to resolve and distinguish these features in tissue to visualize the microvasculature with a greater resolution (~2 µm) and good penetration depth (~ 400 - 800 µm) with our system. The ability to study the stroke, progression of small tumours and other disease models requires an OCM system with potential parameters like a high-resolution system of less than 5 µm, depth of focus of around 500 µm and reasonable oversampling to attain high-quality angiography. Here we discuss these important parameters for the in-vivo imaging of the mouse brain to characterize the OCM system for the in-vivo measurements. The mouse was deeply anaesthetized and was mounted on the stereotactic frame, and the head was immobilized during the experiments.

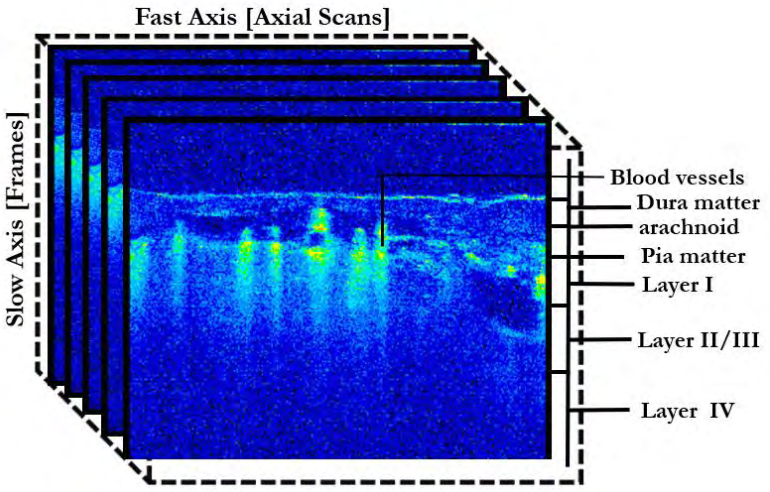

Figure 4-1 The cross-sectional B-scan of the in-vivo mouse brain obtained from the OCM system represents different cerebral region layers with the fast and slow axis.

4.1.1 Objective lens for brain imaging

The objective lens is used in the microscope to magnify the objects to see tissue in greater detail. The numerical aperture (NA) of a lens is defined as the ability of the cone or aperture to collect light and resolve the fine details in the specimen at a fixed objective working distance. The NA of an objective lens is directly proportional to the resolution. There is a trade-off between magnification and working distance - the working distance decreases as the lens magnification increases. Two lenses, 10× NA 0.25 and 4× NA 0.13 were used to test and compare structural and motion angiography quality. Figure 2 shows the results obtained with these lenses on a 3-D scatter test subject (top row) and in-vivo mouse brain (bottom row). Both images were cropped to the same region of interest. It was noted that for mouse brain angiography, 10× gives better resolution, and 4× gives a better penetration depth. As can be seen from the angio images, it is sufficient to use the 4× NA 0.13 lens to image small blood vessels at the same level of detail as with the 10× objective.

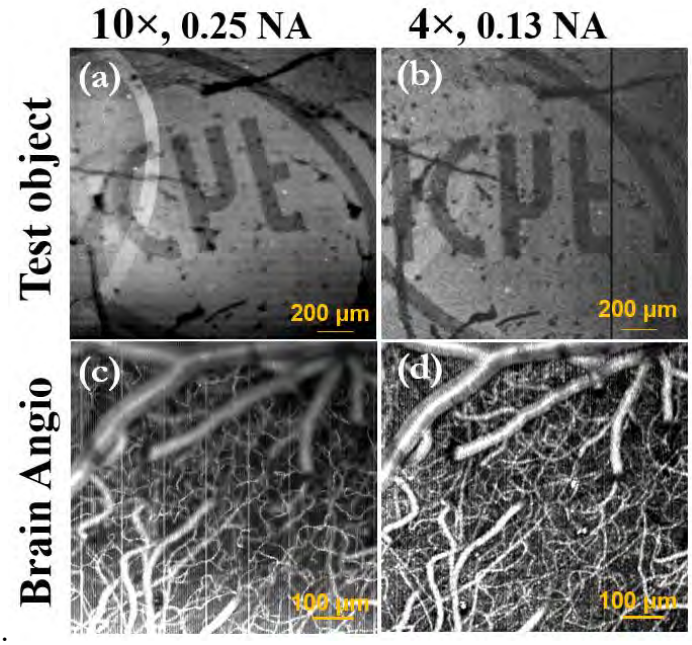

Figure 4-2 OCM and angiographic images acquired with objectives: 10× NA 0.25 (left) and 4× NA 0.13 (right) obtained for 3-D test disc (top row) and in-vivo mouse brain (bottom row)

4.1.1 The optimum position of the focal plane

The laser beam was focused at different depths from the surface of the mouse brain tissue. Experiments were performed with optimal focus to ensure visualization of the sharpest vessels.

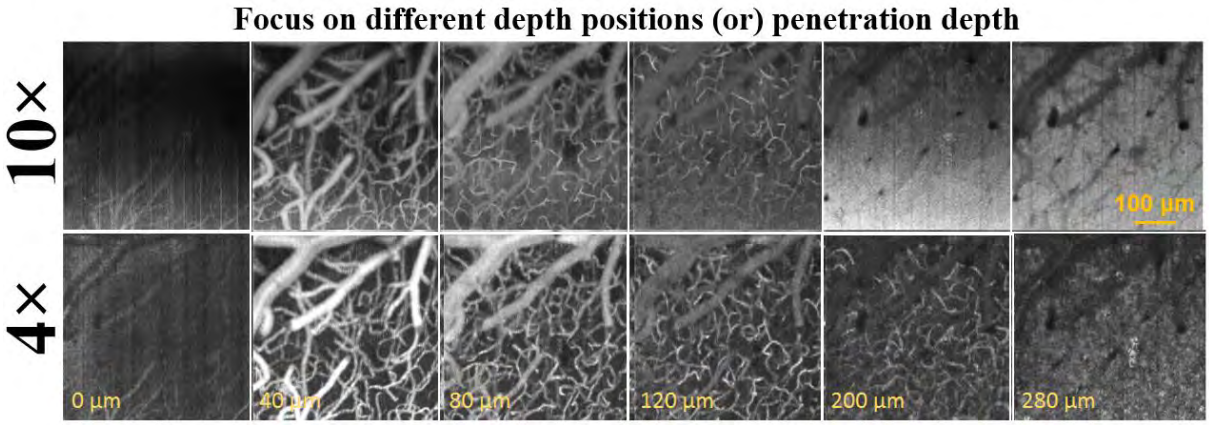

Figure 4-3 Focus at different depth positions of mouse brain: at the surface of the cranial window (0 µm), superficial layers (40 µm), middle layers (80 µm) and, deeper layers (120 µm, 200 µm, 280 µm) for 10× NA 0.25 (top) and 4× NA 0.13 (bottom) objectives.

Selecting the optimal focal plane position of the system is critical for making longitudinal measurements in animals. The repeatability of structure, the sharpness of vessels, and the number of vessels will depend on the focus position. Fortunately, the vessels on the surface of the brain form a layer of well-established thickness, and it is relatively easy to set the focal position reproducibly for both types of lenses. The results are shown in Figure 4-3 showing the focus (f) of the lens at different depth positions: on the surface of the cranial window (f = 0 µm), in the superficial layer (f = 40 µm), in the middle layers (f = 80 µm), and deeper layers (f = 120 µm, 200 µm, 280 µm) for the 10× NA 0.25 (top) and 4× NA 0.13 (bottom) lenses for the mouse brain area. The results show that we could visualize the microcirculation up to a depth of 200 µm with good resolution. The focus at the level (f = 80 µm) would be optimal to visualize both large and small vessels with good resolution. Figure 4-3 shows that microvessels are more prominent when the focus is in deeper areas, but there is a trade-off with macrovessels.

4.1.2 Oversampling

Oversampling (L) is defined as the number of repetitive measurements of the same region to achieve a high-quality angiography with a better signal to noise ratio. The consecutive B-scans can be subtracted from each other to yield dynamic or motion information.

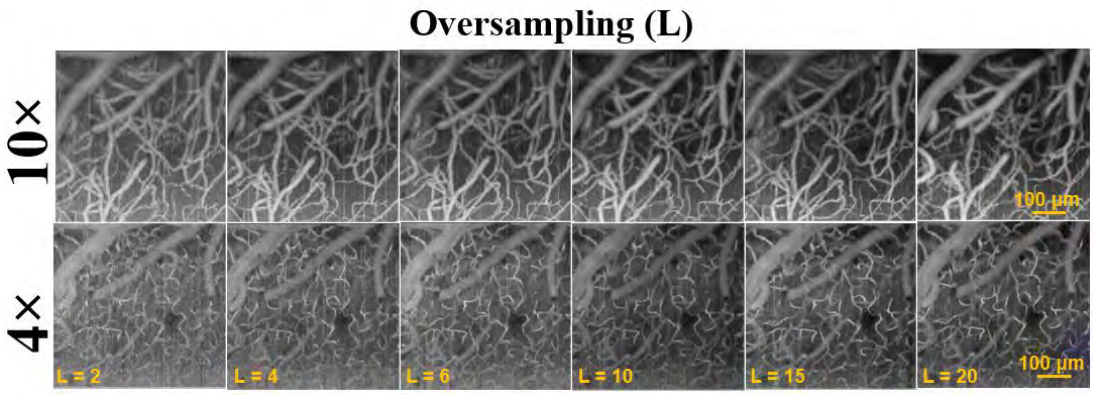

Figure 4-4 The oversampling size L = 2, 4 , 6, 10, 15, 20 for 10× NA 0.25 (top) and 4× NA 0.13 (bottom) objectives of mouse brain angiography.

The oversampling of Size L = 2, 4, 6, 10, 15, 20 was chosen to test the efficiency and quality of cerebral angiography of the mouse brain as shown in Figure 4-4 for 10× NA 0.25 (top) and 4× NA 0.13 (bottom) objectives. The higher oversampling, the larger is Size of data, which increase data acquisition and processing time. We aim to achieve a high-quality angiography using a high-speed OCM, which enables the acquisition in a few milliseconds to see the dynamic changes in stroke, tumour and other diseased models. Hence, we limited our sampling size to 6, which has an optimal acquisition time and sufficient resolution to quantify the microvasculature.

4.1.3 OCM system: Focusing

In the OCM system, lateral and axial resolution is vital to characterize the potential of the system. The axial or longitudinal resolution gives information about penetration depth or focuses on different depth positions. It was determined from the numerical aperture of the objective. The depth segmented angio obtained from a single measurement from the mouse brain cerebral vasculature with 10× (top) and 4× (bottom) objective lens at segmented depths: 0, 75, 150, 250, 350 and 450 µm and their resultant enhancement in the microvasculature was depicted in Figure 4-5.

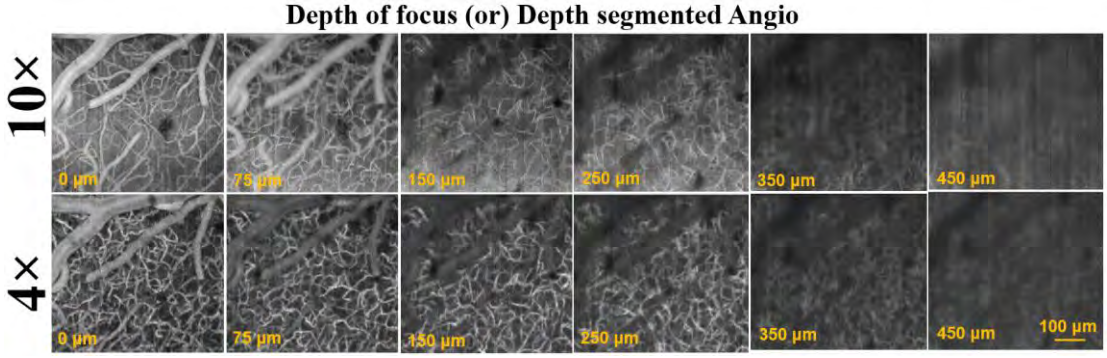

Figure 4-5 The depth segmented angio of the mouse brain at segmented depths: 0, 75, 150, 250, 350 and 450 µm and their resultant microvasculature enhancement with depth are depicted below with 10× (top) and 4× (bottom) objective lens.

4.1.4 OCM system: Field of view

The Field of View (FOV) is the total area occupied by the diameter of the circle of light visualized through the microscope. The relation between magnification and FOV are inversely proportional to each other.

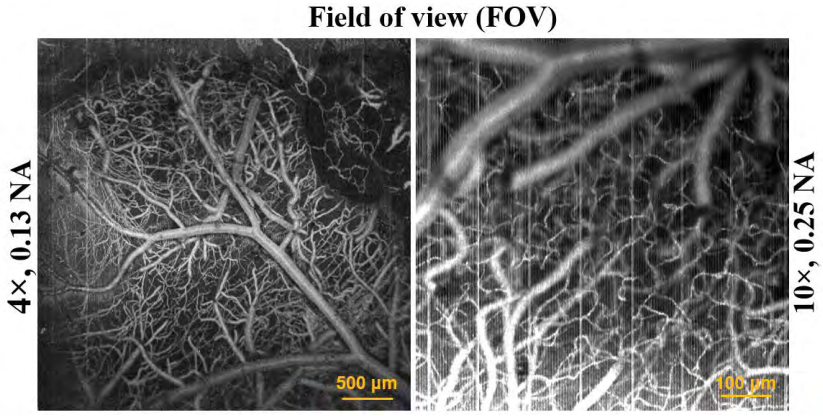

Figure 4-6 The field of view (FOV) of mouse cerebral microvasculature with 10× NA 0.25 (left) and 4× NA 0.13 (right) objective lens.

The FOV of mouse cerebral angiography with two objectives lens for 10× NA 0.25 (right) and 4× NA 0.13 (left) are represented in Figure 4-6. The 10× objective has the better resolution and the maximum FOV achieved is 1.7 × 1.7 mm, whereas for 4× objective has a longer penetration depth, the FOV is 4.4 × 4.4 mm.

4.2 OCM processing algorithms

The important OCM processing algorithms used to achieve microvasculature visualization, such as angiography algorithms, bulk motion correction, and averaging algorithms, are applied to mouse brain imaging. The physiological activities such as cardiac and respiratory motions causing motion artefacts are corrected by suppressing the global phase fluctuations (GPF's) in the axial direction and bulk image shifts (BIS's) methods.

4.2.1 OCM-A algorithms

The OCM-A algorithms were tested on the in-vivo mouse cerebral angiography to evaluate their efficiency for the visualization of the small capillaries and sensitivity for flow motion contrast detection.

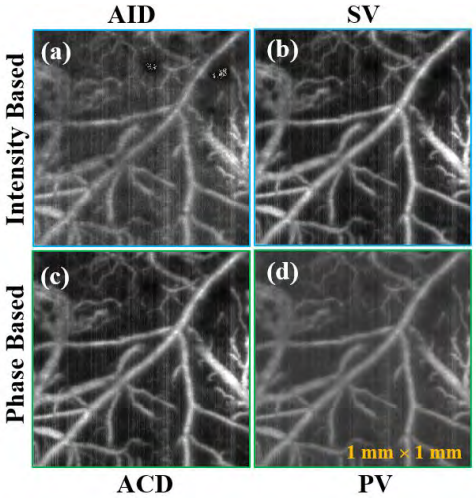

Figure 4-7 (a-b) represents the intensity-based angio algorithms (AID, SV) and (c-d) represents the phase-based angio algorithms (ACD, PV).

The four angiography algorithms are applied to the obtained in-vivo OCM mouse brain data, out of which two are intensity-based: absolute intensity difference (AID), speckle variance (SV) and the other two are phase-based: absolute complex difference (ACD), phase variance (PV). The ACD algorithm was used for the angio processing since it effectively reduces the current in-vivo brain data for bulk motion correction and better signal to noise ratio than other methods. Figure 4-7 represents the angiography image obtained after application of the intensity-based angio algorithms: (a) AID and (b) SV and phase-based
angio algorithms: (c) ACD and (d) PV.

4.2.2 OCM averaging methods

We have applied three different A-scan averaging techniques to the in-vivo mouse cerebral vasculature OCM data [260]: magnitude of mean averaging, spectral and time-domain OCT (STdOCT) averaging [261, 262] and complex averaging. The quality and impact of the averaging techniques on the angiography image were analyzed using the parameters: Signal to noise ratio (SNR), dynamic range (DR), C (speckle noise) and contrast to noise ratio (CNR). The SNR, CNR, and DR should have the highest possible value, whereas 'C' should have the minimum value since it depends on the signal intensity fluctuations to have an optimal performance of the OCM imaging. The Figure 4-8 represents the results of the averaging methods applied to both motion B-scan (top) and angiography data (bottom): the magnitude averaging (left column), complex averaging (middle column) and STd-OCT averaging (right column) methods for mouse brain microvasculature. The Figure 4-9 graph represents the SNR (blue), C (orange), DR (grey) and CNR (yellow) values for three averaging methods: magnitude averaging, complex averaging and, STd-OCT averaging obtained after analysis of the mouse

cerebral motion B-scan (left) and angio (right) images. It can be seen clearly that SNR, DR and CNR values are highest, and 'C' is lowest for the STdOCT approach, which makes it a better fit for in-vivo brain imaging.

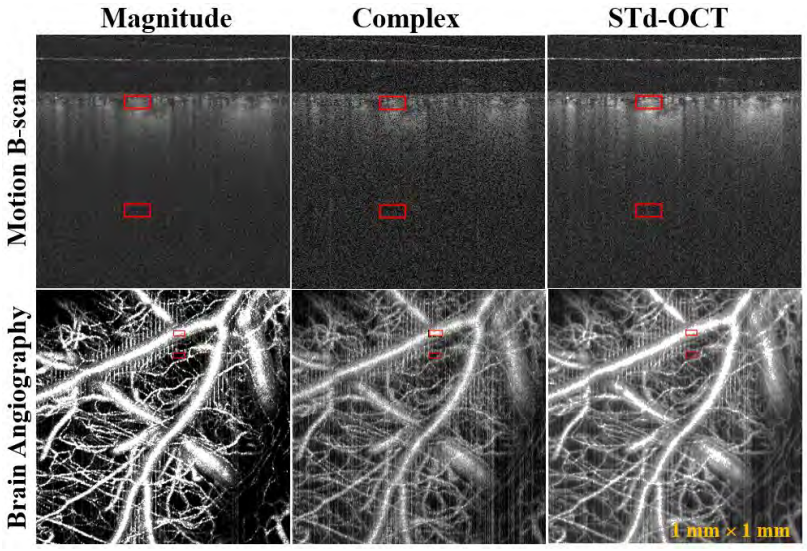

Figure 4-8 The averaging methods for the motion B-scan (top) and angiography (bottom): magnitude averaging (left column), complex averaging (middle column) and STd-OCT (right column) methods applied on mouse brain vasculature

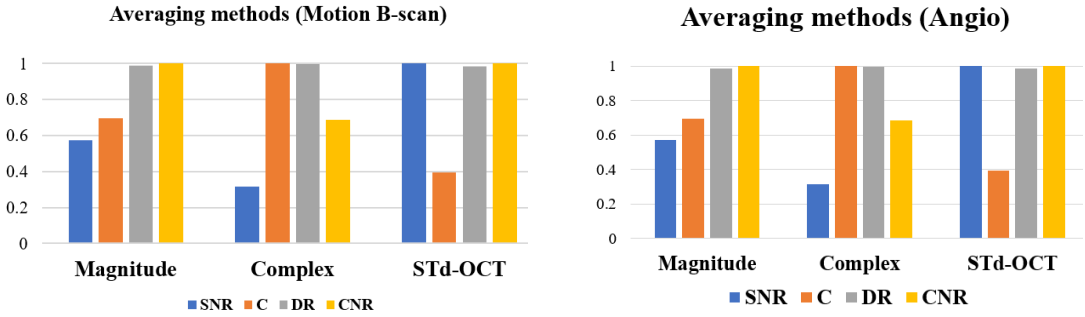

Figure 4-9 The ISNR, C, IDR and CNR values for averaging methods obtained after analysis of the mouse cerebral motion B-scan (left) and angio (right).

The STdOCT averaging offers high sensitivity to all averaged A-scans' decorrelation and speckle reduction and combined the advantage of both magnitude and complex averaging techniques at the cost of increased computation time for processing. Moreover, this method also provides both the structural and functional information it initially introduced for elastography and Doppler measurements. If computational time is a major drawback, then magnitude averaging can be considered the best method for averaging.

4.2.3 OCM artefact removal

The major challenge in processing the OCM angiographic (OCM-A) data is the removal of artefacts related to the motion of the sample. The main reason for the artefacts is the movement of the mouse due to heartbeat and respiratory movements. The vertical and

horizontal stripes are the resultant of these artefacts on the angiographic images. The best way to handle these artefacts is to deeply anaesthetize the mouse and fixing the head in a stereotactic frame. The artefacts were handled during the data processing with motion correction algorithms.

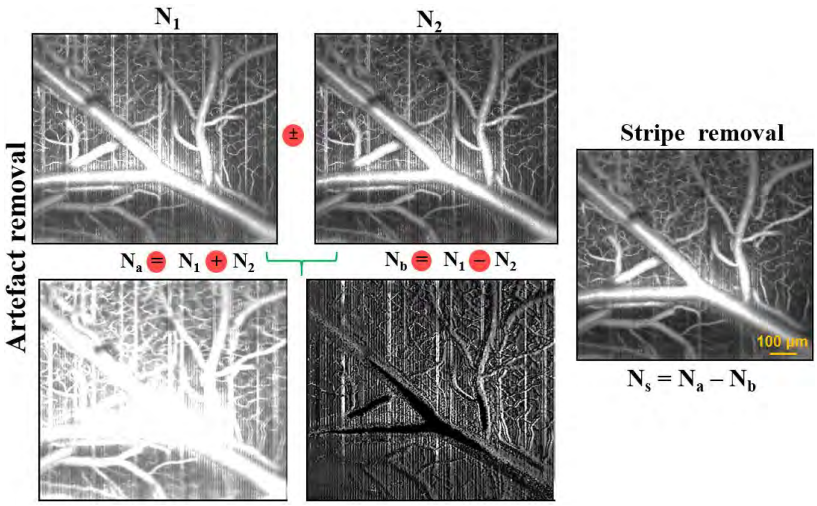

Figure 4-10 The stripe removal algorithm for mouse cerebral microvasculature showing two consecutive angiography images (N_1 and N_2), the resultant of addition and subtraction of the consecutive images (N_a and N_b) and, the final image obtained after stripe removal (N_s)

Here, we consider the microvasculature as static components and artefacts as dynamic components. Later, a simple algorithm to remove these artefacts from microvasculature. This is one of the most efficient ways to achieve high-quality angiographic data at the moderate cost of increasing the processing time and memory of the system. If the artefacts occur at the same place in the two data sets, this method does not work the best. If the artefacts still prevail, then the easiest way to remove the stripes is to acquire at least two consecutive angiography images of the same region (N_1 and N_2). In that case, more than two data sets should be used for this algorithm. Later, a Fourier filtering can also suppress the stripes at the cost of loss in data quality. Figure 4-10 shows the algorithm for stripe removal; here, the images resulted after the addition ($N_a = N_1 – N_2$) and subtraction ($N_b = N_1 – N_2$) of consecutive angiography data sets N_1 and N_2 will be used to remove the stripes. The subtraction of N_a and N_b results in the final angiography images without stripes.

4.2.4 OCM Post-processing methods

The Hessian-based Frangi vesselness filter is used for the enhancement of vessels, combines the outputs of several Gabor filters at different orientations and scales. This method uses a ridge detector, enhancing the tubular-like (e.g. vessels) geometrical structures. However,

this method's major drawback is that anything that is not narrow and elongated will also be attenuated in the output. To resolve this problem, the data is upsampled before applying the Hessian-Frangi method and applied other post-processing algorithms to achieve a high-quality angiography. We can also filter the large vessels (using a larger sigma value), smaller vessels (using a smaller sigma value) independently or select the optimal sigma to get a more balanced rendering.

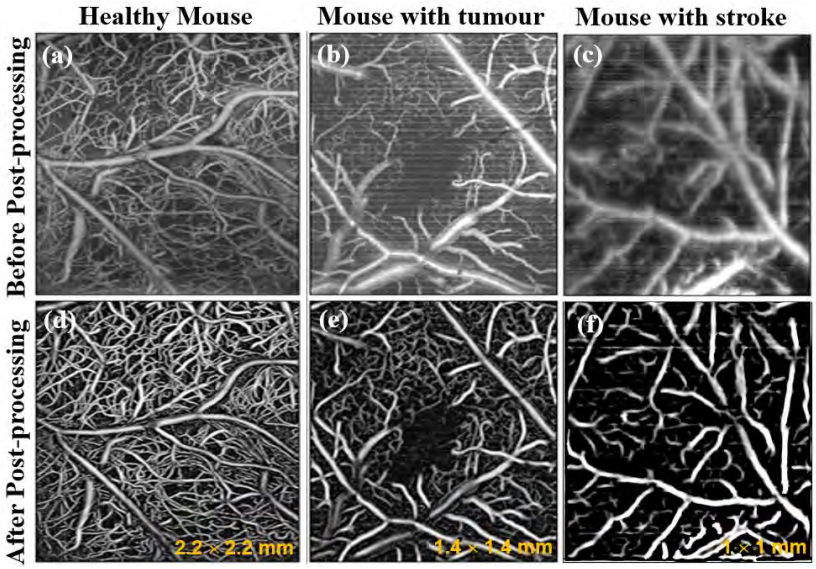

Figure 4-11 Before (above) and after (below) application of Hessian-Frangi analysis and other post-processing methods for improving visualization of cortical vessels applied to the dataset for healthy mouse, the mouse with induced stroke and mouse with tumour.

Global thresholding is not effective for the enhancement of small vasculature. So, instead, we used the adaptive thresholding method to enhance the smaller microvasculature. We also used a combination of Fast Fourier Transform (FFT) and median filters. The increase in the visibility of cerebral vasculature with the enhancement of smaller vessels and improvement in the quality of OCM-A data is shown in Figure 4-11 before (top row) and after post-processing (bottom row) with almost zero background noise. This comparison suggests that the efficiency of post-processing steps is crucial in achieving the enhancement and high quality of microvasculature reconstructions for both healthy and diseased conditions like stroke and tumour for further quantification.

4.3 Bessel vs Gaussian Angiography OCM results

The potential of applying non-diffracting beams generated by conventional optics in place of the Gaussian beam to extend the DOF while maintaining high lateral imaging resolution in OCM was studied. A comparative analysis between OCM imaging with Bessel and

Gaussian beam illumination using custom-created optical artefacts was described. The self-healing and self-diffracting properties of the Bessel beams have an advantage of extended depth of field (DOF) over a Gaussian beam whilst preserving the transverse resolution in the OCM system. There were several studies on both Gaussian and Bessel beam OCM systems, but these studies were mainly concentrated on phantoms. There were no studies on in-vivo and angiography comparison with these systems. The challenge of brain imaging is the increased scattering properties with depth in turbid tissue medium to achieve a uniform image contrast in deeper regions of the tissue using OCM. We investigated the use of axicon lens by generating Bessel beam and compared the advantage along with the performance of Bessel beam over Gaussian for imaging using OCM. We show the influence of image quality for both beams for in-vivo imaging of the mouse brain. We also presented the detailed studies of B-scans and depth encoded angiomaps using the OCM system on the cerebral region of the in-vivo mouse brain with cranial window. We aim to present the angiography comparison and discuss the merits and demerits of Bessel and Gaussian OCM along with the practical aspects, user-friendly and robust OCM for everyday measurements. The Bessel beam OCM and the standard Gaussian OCM setup were home-built and configured with Mach–Zehnder interferometer with axicon lens to generate the Bessel beam with a gaussian detection system and Michelson interferometer, respectively. Both the systems have a similar laser source of ~6fs laser source and a central wavelength of 800 nm.

Nevertheless, the Bessel beam suffers from contrast degradation due to the extra side lobes in the spectrum and also inherent SNR trade-off compared to Gaussian beams equal power at the focus plane for scattering medium. The Bessel beam specification includes imaging depth ~800 microns with 2.2 microns lateral resolution with a sensitivity of 94 dB. In comparison, the specification for the Gaussian beam OCM is: imaging depth ~300 microns with 2-3 microns lateral resolution with the sensitivity of 86dB.

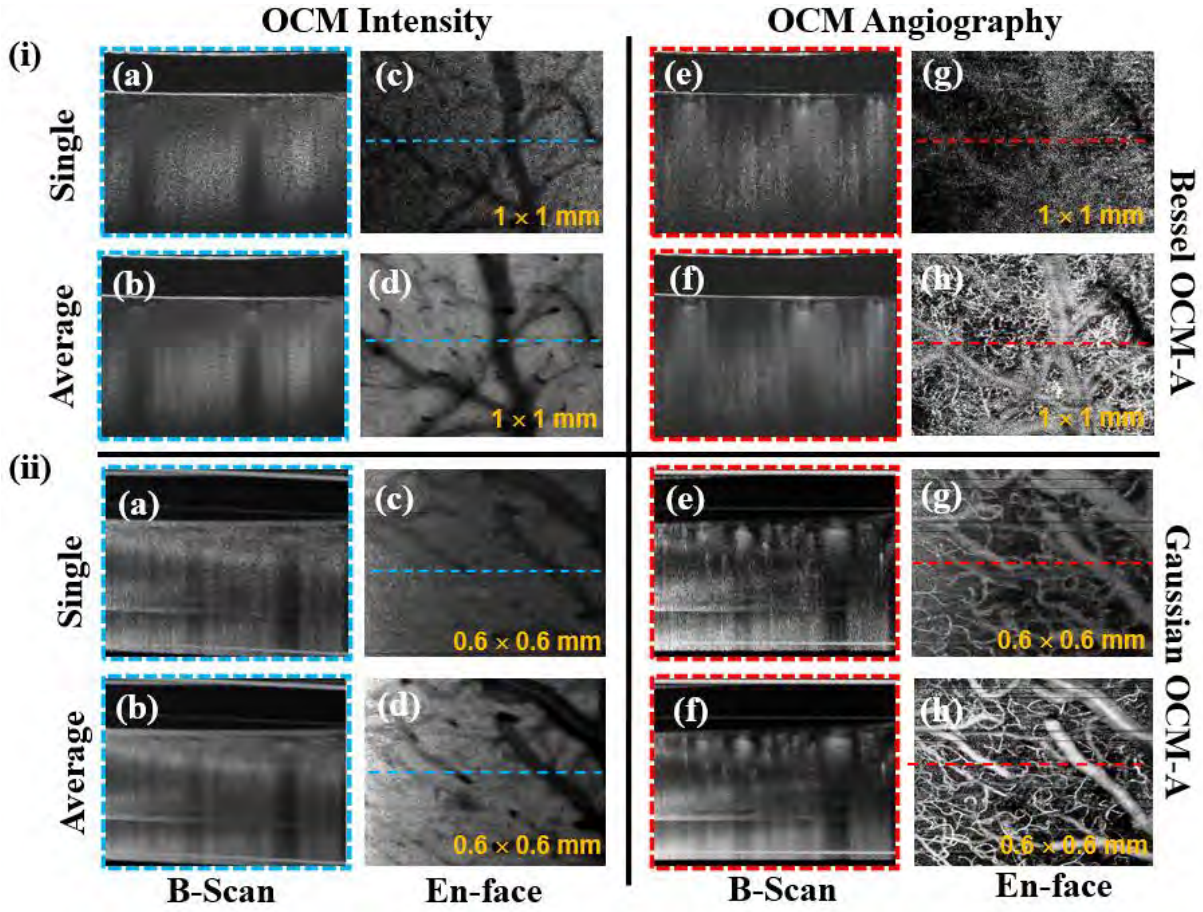

Figure 4-12 (i-ii) represents the results for the Bessel beam OCM-A and Gaussian OCM-A system. The OCM intensity: (a-b) the B-scan for single and averaged B-scans (N=10) respectively, (c-d) the structural angio image for single and averaged angio projection; The angiography images: (e-f) for the single motion B-scan and averaged motion B-scans (N=10) respectively, (g-h) for the single angiography and averaged angiography projection, all the dashed line represents the corresponding central B-scan for the structural image.

The scanning protocol used for Bessel and Gaussian beam OCM consists of 300 A-scans × 300 B-scans and 400 A-scans × 400 B-scans, respectively. All the experiments are performed using a 10x NA 0.25 objective lens for both imaging systems. Figure 4-12 (i-ii) represents the OCM intensity and angiography projection of mouse cerebrovascular with Bessel beam and Gaussian beam, respectively. Whereas the OCM intensity images of B-scan and angio: (a-b) the single B-scan and averaged B-scans (N=10) respectively, the OCM structural angio: (c-d) structural image for single and averaged angio projection. Whereas the motion angiography images: (e-f) the single motion B-scan and averaged motion B-scans (N=10) respectively, (g-h) for the single angiography and averaged angiography projection. The number of B-scans used for averaging is 10, and all the dashed line represents the corresponding central B-scan for the structural image or angiography image. The angiomaps obtained at different depths also infers and concludes that the Bessel beam has a uniform focus in the segmented depth. However, the overall contribution from all the regions is comparable to the Gaussian OCM.

4.3.1 Quantitative analysis with OCM image parameters

The image quality is assessed quantitatively with four parameters corresponding to different image properties analyzed for Bessel and Gaussian OCM data. To optimize the performance of OCM imaging, the SNR, DR, C and CNR are evaluated. Figure 4-13 represents the results obtained to quantify the angiography of the mouse brain using Bessel beam OCM-A (top row) and Gaussian beam OCM-A (bottom row) optical system. The shows are raw cross-sectional (B-scan) obtained from the Gaussian and Bessel beam OCM setup are averaged (N=10), and the ROI was selected for quantification. The different segmented depths: depth1 (green rectangle), depth2 (pink rectangle), depth3 (red rectangle) are chosen for the quantification. The region of tissue near the surface of the cranial window was rejected as it suffers from glass reflection. The corresponding z-axis or depth profiles intensity profiles are plotted as a function of depth for the raw cross-sectional image (B-scan) and distance (in pixels) for the segmented regions and are represented in Figure 4-13 (b,c) for Gaussian and Bessel beam respectively. The quantitative image metrics parameters such as signal to noise ratio (left), dynamic range (middle) and the signal to noise ratio (right) are evaluated for these three-segmented regions and are plotted in Figure 4-13 (c,f) for both Gaussian and Bessel beam OCM setup respectively.

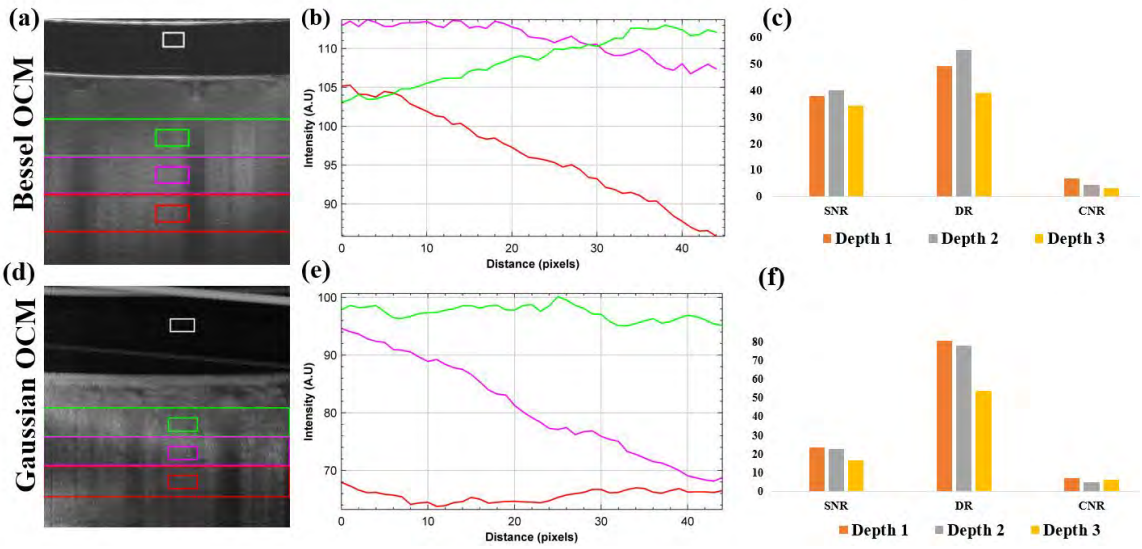

Figure 4-13 (a,d) OCM Intensity averaged B-scan (N=10) of Bessel and Gaussian beam OCM-A setup respectively for three different layers; (b,e) their corresponding depth profiles of each layer (45 pixels) with Bessel and Gaussian beam OCM-A system respectively; (c,f) the quantification of ISNR, IDR and CNR parameters for both the systems.

The white rectangle measures for fixed-position background (BG) region of interest (ROI), and the other coloured rectangles measures the sliding signal ROI. We analyzed and confirmed that SNR, CNR, and DR does not change significantly when different ROIs are used. From these

graphs shown, it was very clear that Gaussian has similar penetration depth, especially for angiography. However, the image metrics decay slower with depth for Gaussian than for Bessel illumination. To visualize trends in SNR, CNR and DR vs depth are plotted in Figure 4-13, but they cannot be used for absolute comparison between two systems (because of the differences in input images) and the system limitations. This quantitative analysis clearly shows that both SNR and CNR decrease with a depth significantly slower for Gaussian than for Bessel setup. The intensity profiles of the Bessel beam are quite smooth in comparison with the results of Gaussian. The angiomaps obtained at different depths also infers and concludes that the Bessel beam has a uniform focus in the segmented depth. The Bessel beam has a unique advantage because it extends the depth of focus, but the Bessel beam OCM construction and maintenance complexity make it less attractive over Gaussian beam OCM. However, the overall contribution from all the regions is comparable to the Gaussian OCM. Figure 4-14 represents the different segmented angio layers for different depths (S1, S2, S3, S4, S5) of the mouse cerebral microvasculature for the Bessel beam OCM-A and Gaussian beam OCM-A setup.

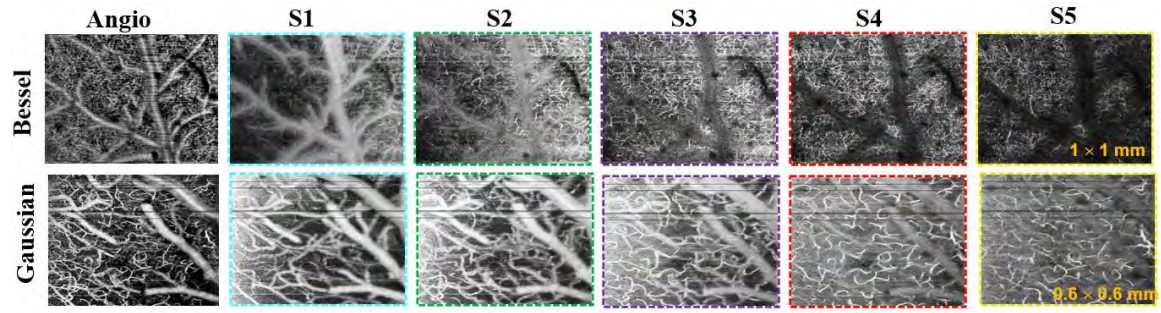

Figure 4-14 Angio depth segmented layers for Bessel beam OCM-A (top) and Gaussian Beam OCM-A (bottom), respectively.

Figure 4-15 represents the exemplary results obtained from the mouse cerebral angiography using Bessel beam OCM-A (right) and Gaussian beam OCM-A (left) optical system. Figure 4-15 (a-b) represents the depth encoded angiography projection or the 3D angiography data, where the depth was represented as the third dimension for both Gaussian and Bessel beam systems, respectively.

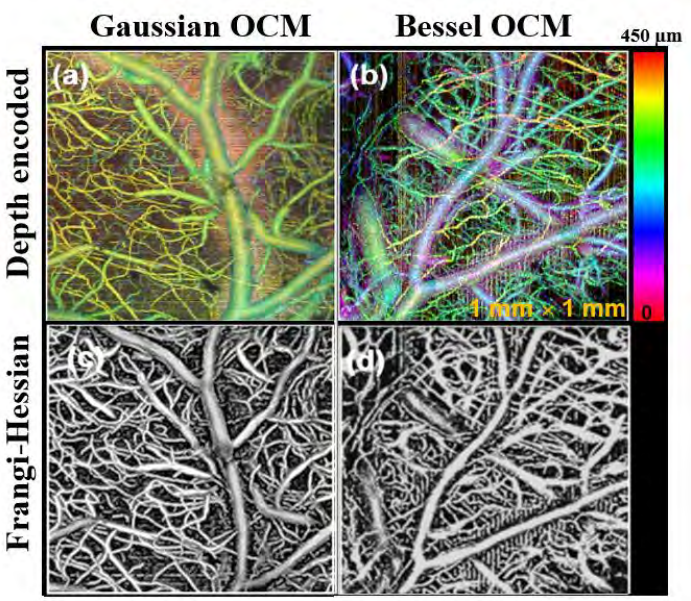

Figure 4-15 (a-b) shows the depth encoded angiomaps obtained from the Gaussian OCM (right) and Bessel beam OCM (left) set up, respectively; (c-d) corresponds to the enhanced angiomaps after post-processing methods with Hessian based frangi filter.

The results after post-processing methods and the Hessian-based frangi filter application are shown in Figures 4-16 (c-d) for Gaussian and Bessel beam OCM-A. From the angiomaps obtained from both the beams, it can be clearly seen from the quality of the microvasculature at different depths, the Gaussian beam is equally effective as the Bessel beam, and it gains superiority in the reduction of contrast around the focal region. These results are consistent with the theoretical and experimental simulations on phantoms [134]. We strongly agree that for Bessel beam have a unique advantage because it extended depth of focus. For OCM-A, the difference for the systems is also negligible, and for critical studies including deep microvasculature, neurons the Bessel system is more powerful. The trade-off between the system should be chosen on the application for biological studies. The signals out of focus as regular OCM also gives a reasonable image quality.

4.4 Glioblastoma longitudinal tumour progression

The Glioblastoma Multifrome (GBM) longitudinal progression is primarily concerned with demonstrating the possibility of quantifying brain tumour growth. The OCM system can evaluate tumours (~2-6 microns) and has the greatest advantage to understand the repressed mechanism in their growth progression. The technical capabilities of the Gaussian OCM system in imaging of vascular network and neovascularization was demonstrated during the tumour development. In this work, we had to take the first step towards developing methodologies for quantitative monitoring of glioma and test them on animals. We aim to study the small tumours

(~2 μm in diameter) up to 350 μm depth of GBM tumour developed in mouse brain and evaluate the tumour progression. The cranial of mice prepared was imaged after 7-8 days prior to the experiments. Later, the GBM tumour was injected into the mouse brain, and the growth progression was analyzed for a few days. The tumour was injected into two different mice for Gl261 implantation/tumour studies (Glioblastoma-1, Glioblastoma-2), and the other two served as a control for the experiments. The mice injected with glioma cells developed a solid tumour at the injection site. The results in the second animal for the control mouse demonstrate similarity, and hence we have shown only one set of data for the control mouse. The longitudinal tumour progression was acquired for 1, 3, 7, 9, 11 and 14 days after the injection. We ended experiments following indications of the bioethics committee on day 14 due to the weight loss of the mice and the real possibility of their death. The OCM imaging requires the presence of glass tightly adjacent to the brain and glued to the skull bone to minimalize brain movement and keep appropriate moisture of brain surface necessary to maintain stable scattering properties. The angiographic and intensity images were processed, and the volume of the tumour was visualized. The difference between healthy and tumour mouse was visualized in the morphological nature of the tissue, such as the tortuosity, irregular nature of vessels during progression.

4.4.1 Control mouse vs Glioma mouse results

The growth and progression of the control and tumour mouse brain vasculature were followed up using OCM measurements and was performed at the following time points: 1, 3,7,9 11, and 14 days after injection of the glioma cells for over two weeks period.

Control mouse

The control mice were studied on the same days as the GBM mice. Figure 4-16 – Figure 4-18 demonstrates the acquired angiography images for both motion angiography [Figure 4-16(a-d) – Figure 4-18(a-d)] and structural angiography [Figure 4-16(e-h) – Figure 4-18(e-h)] images of days 3, 11 and 14, respectively, for the control mouse. The total region of imaging (yellow) with their depth segmented regions: I (red), II (blue) and III (green). The corresponding structural B-scan [Figure 4-16(i) – Figure 4-18(i)] and angio B-scans [Figure 4-16(j) – Figure 4-18(j)] were represented. The field of view (FOV) of the angiography images is 2.2 × 2.2 mm (transverse dimensions).

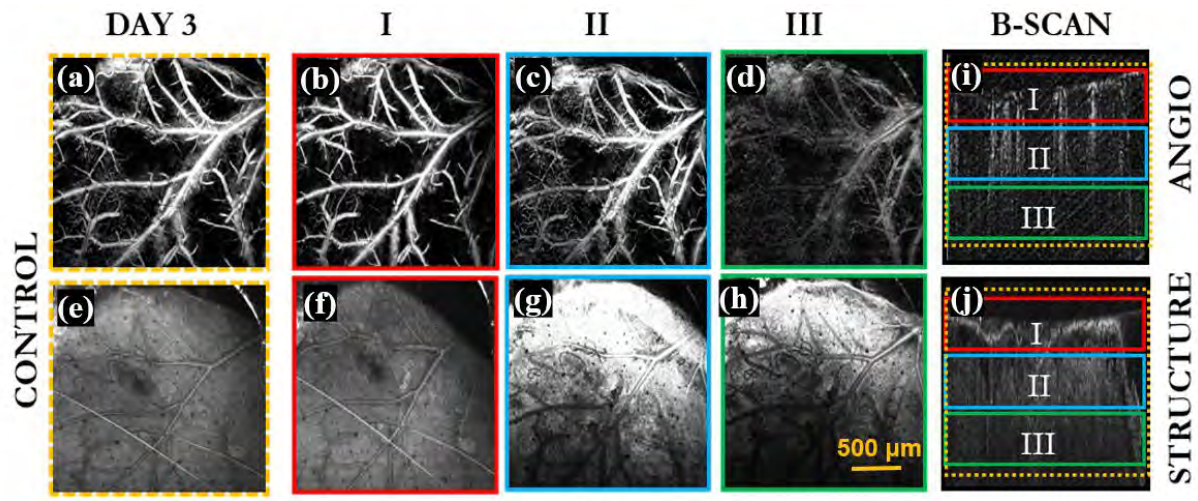

Figure 4-16 The motion angiography (a-d) and structural angiography (e-j) images of day 3 for the control mouse demonstrating the depth segmented regions I, II and III with their corresponding B-scans (i-j).

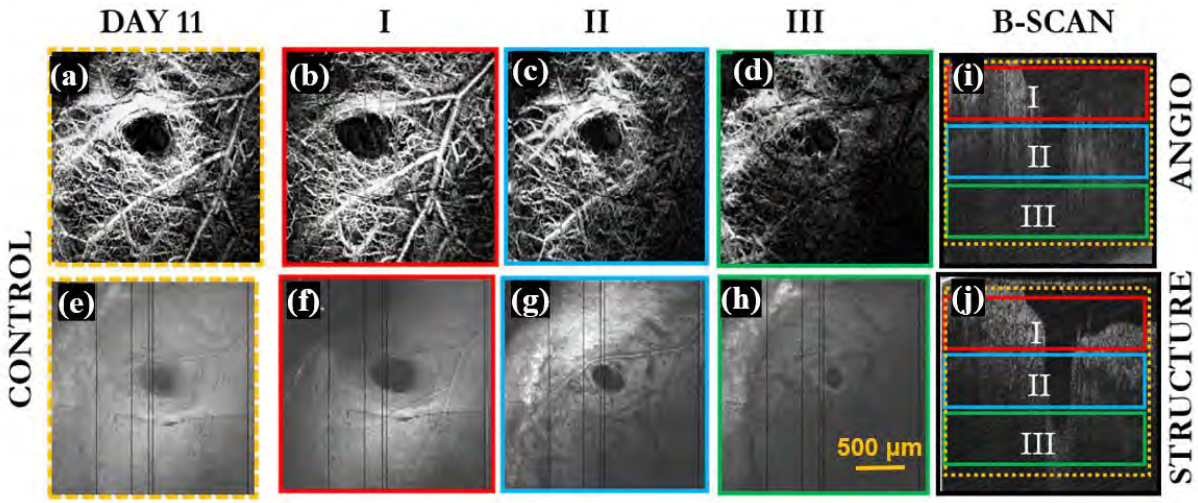

Figure 4-17 The motion angiography (a-d) and structural angiography (e-h) images of day 11 for the control mouse demonstrating the depth segmented regions I, II and III with their corresponding B-scans (i-j).

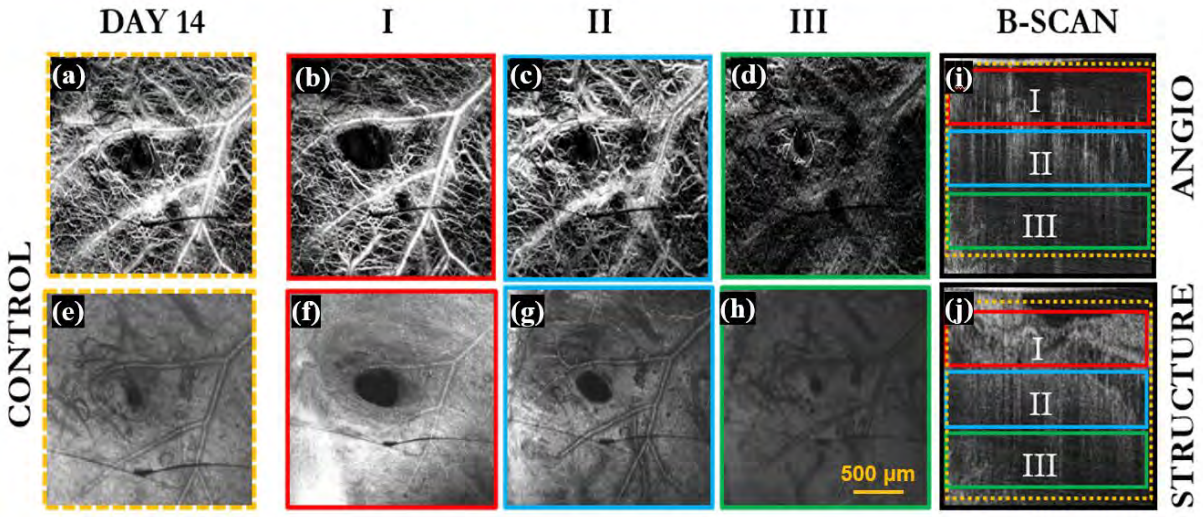

Figure 4-18 The motion angiography (a-d) and structural angiography (e-h) images of day 14 for the control mouse demonstrating the depth segmented regions I, II and III of the corresponding B-scan (i-j).

Glioblastoma mouse

In humans, glioblastoma can develop anywhere within the brain (white and grey matter) but has a predilection for the subcortical white mater and deep subcortical grey matter. No mouse model provides the same tumour phenotype as humans. We used the so-called syngenic model of glioblastoma, where a mouse glioma cell line was implanted into the brain. The demonstration and monitoring of the GBM progression were achieved by acquiring the OCM structural en-face projections and angiography images with a field of view (FOV) of 2.8×2.8 mm (transverse dimensions) at selected time points.

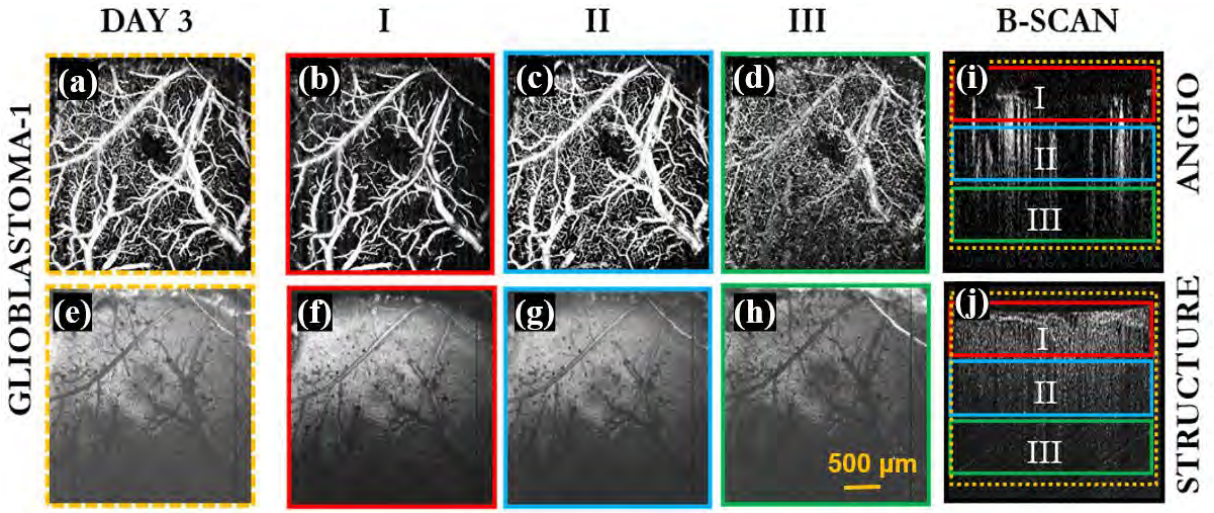

Figure 4-19 The motion angiography (a-d) and structural angiography (e-h) images for day 3 for the mouse1 with glioblastoma demonstrating the depth segmented regions I, II and III of the corresponding B-scans (i-j).

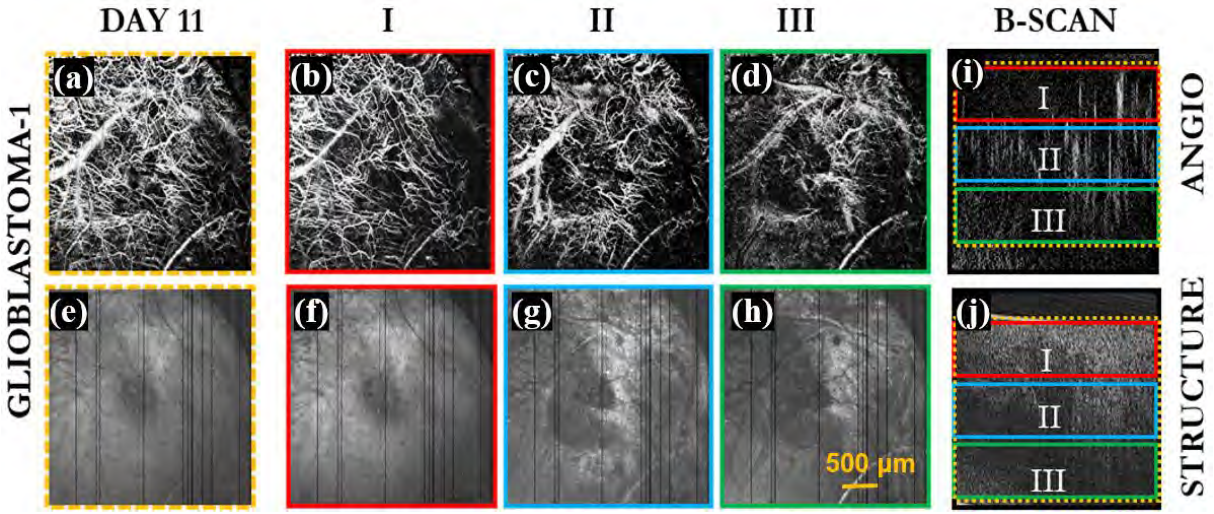

Figure 4-20 The motion angiography (a-d) and structural angiography (e-h) images of day 11 for the mouse1 with glioblastoma demonstrating the depth segmented regions I, II and III of the corresponding B-scans (i-j).

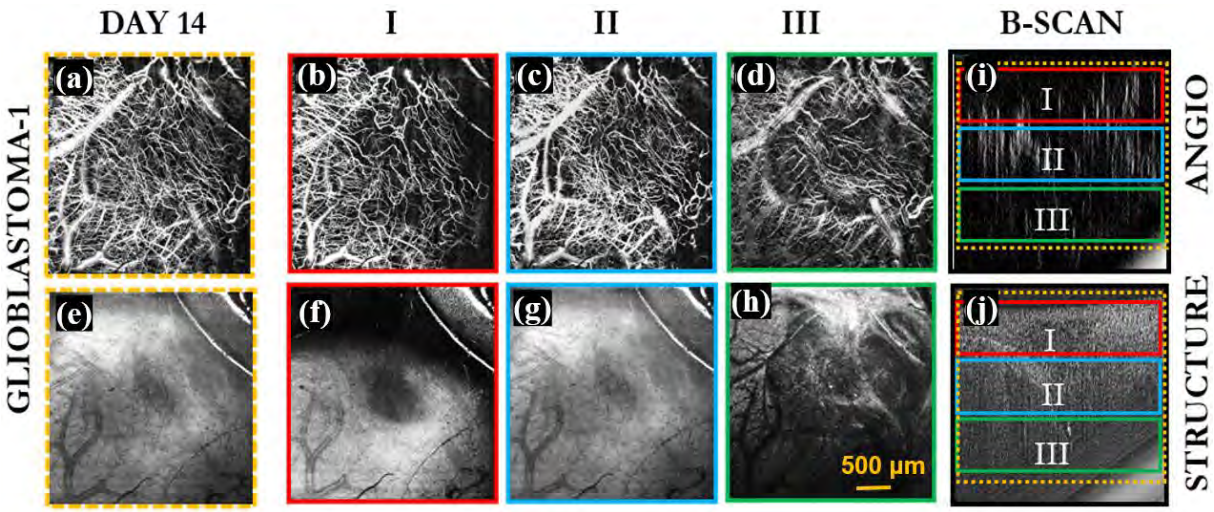

Figure 4-21 The motion angiography (a-d) and structural angiography (e-h) images of day 14 for the first set of the mouse with glioblastoma demonstrating the depth segmented regions I, II and III of their corresponding B-scans (i-j).

Figure 4-19 – Figure 4-21 shows the acquired angiography images for the first set of the mouse with Glioblastoma (Glioblastoma-1). The angiography images obtained for the second set of the mouse with glioblastoma (Glioblastoma-2) was shown in Figure 4-22 – Figure 4-23. The results represent both motion angiography [Figure 4-19(a-d) – Figure 4-21(a-d)] and structural en-face angiography [Figure 4-19(e-h) – Figure 4-21(e-h)] images obtained for day 3, 11 and 14 (left to right) for the Glioblastoma-1 mouse.

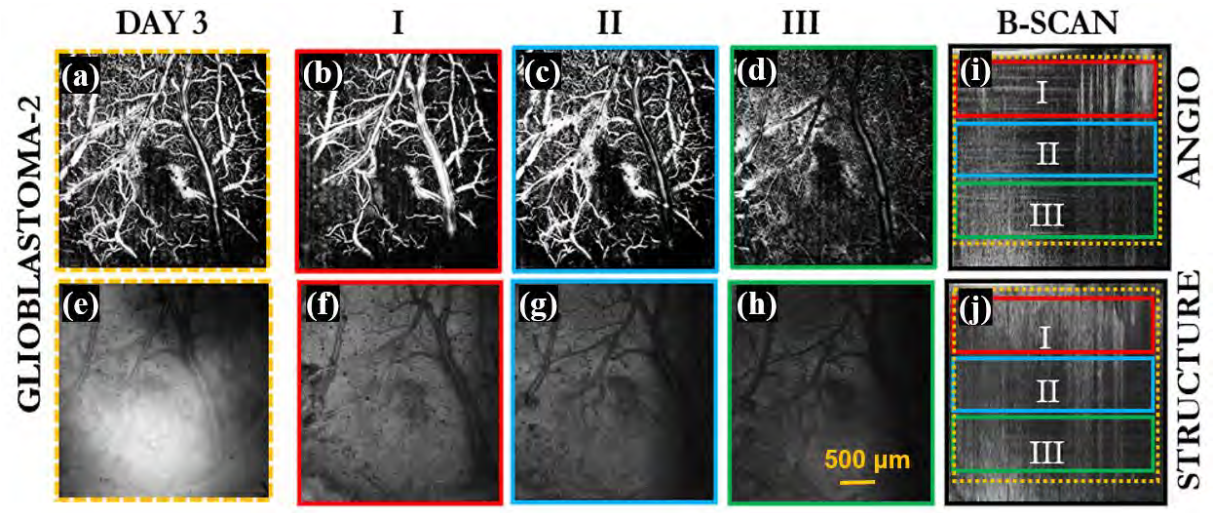

Figure 4-22 The motion angiography (a-d) and structural angiography (e-h) images of day 3 for the second set of the mouse with glioblastoma demonstrating the depth segmented regions I, II and III of their corresponding B-scans (i-j).

The motion angiography [Figure 4-22(a-d) – Figure 4-23(a-d)] and structural en-face angiography [Figure 4-22(e-h) – Figure 4-23(e-h)] images for day 3 and day 14 for the second Gliobalstoma-2 mouse was demonstrated. The total region of imaging (yellow) with their depth

segmented regions: I (red), II (blue) and III (green). The corresponding structure and angio B-scans [Figure 4-22(i-j) – Figure 4-23(a-d)] was demonstrated.

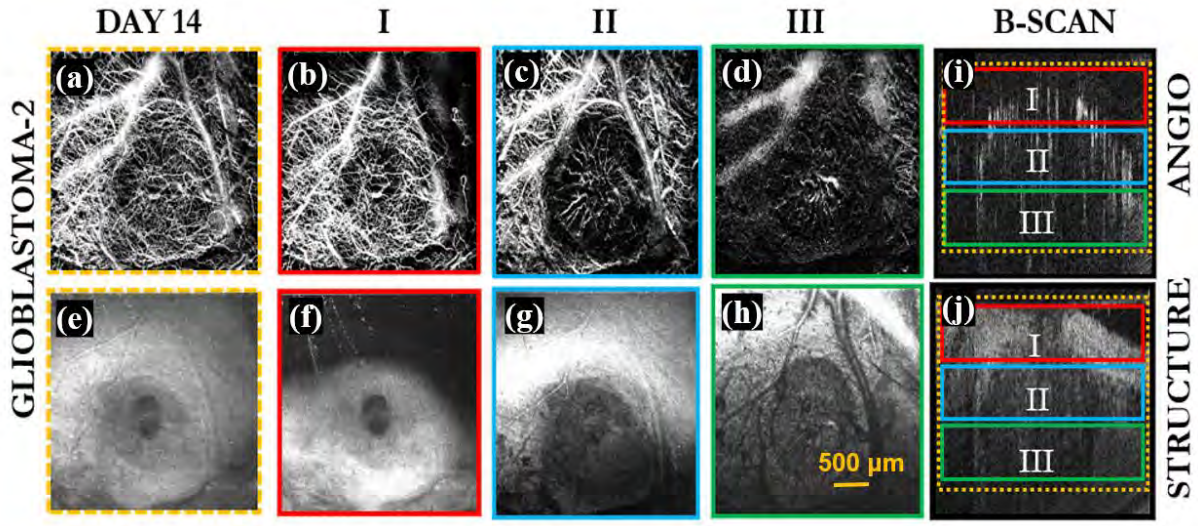

Figure 4-23 The motion angiography (a-d) and structural angiography (e-h) images of day 14 for the second set of the mouse with glioblastoma demonstrating the depth segmented regions I, II and III of their corresponding B-scans (i-j).

4.4.2 Control mouse vs Glioblastoma mouse

Comparing the angiogenesis in both the mice with glioblastoma is used for tumour studies with respect to control mice. We have used two scanning regions of 2.8 × 2.8 × 0.4 mm and 1.7 × 1.7 × 2 mm for each mice in the experiments. However, we choose to represent the scanned region 2.8 × 2.8 × 0.4 mm in XYZ axes as it covers a large FOV for both control and glioblastoma mice.

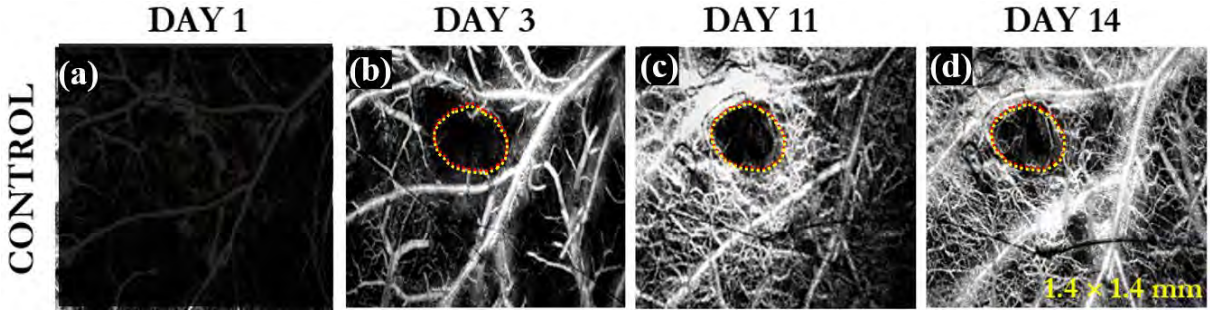

Figure 4-24 (a-b) The summarized angiography images of the control mouse were acquired on day1, day3, day11 and day14 from left to (right), respectively. The yellow dotted region indicates the tumour border, whereas the red dotted region indicates the trace of the needle after injection.

The injection region (red dotted region) was visible on angiographic projections for the control culture medium shown in Figures 4-24(b-d) for day 3, day 11 and day 14, respectively. In contrast, the glioma cells injection (red dotted region) and the tumour border

(yellow dotted region) is shown in Figure 4-25(e-h) for day 1, day 3, day 11 and day 14, respectively for Glioblastoma-1 mouse. Their respective depth encoded images of the Glioblastoma mouse-1 is represented in Figure 4-25(a-d).

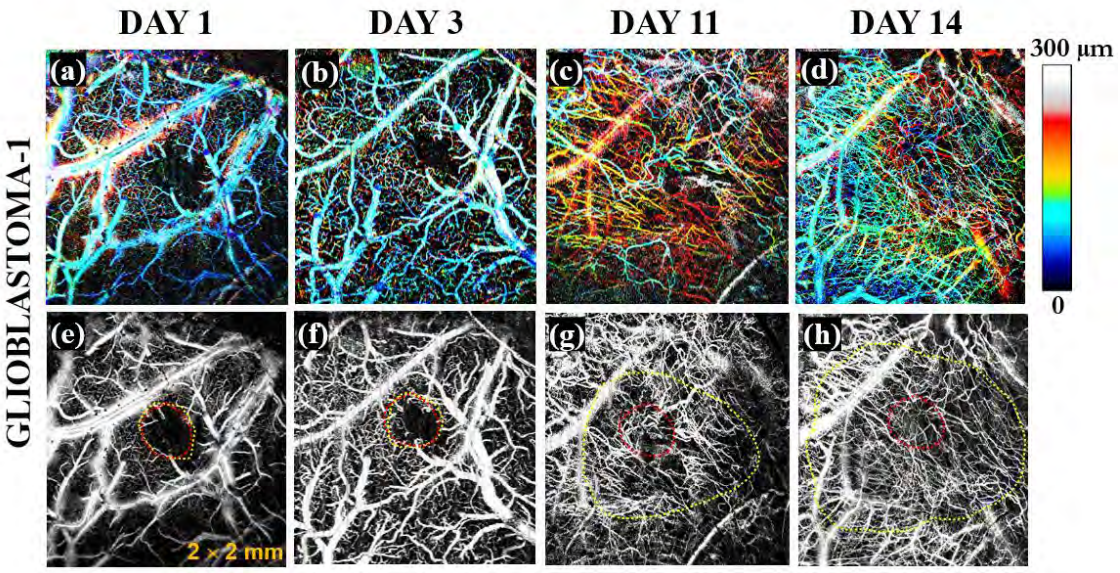

Figure 4-25 The summarized angiography images of the glioblastoma mouse: (a-d) depth encoded angiography and (e-h) post-processed angiographic images acquired on day1, day3, day11 and day14 from left to (right) respectively. The yellow dotted region indicates the tumour border, whereas the red dotted region indicates the trace of the needle after injection.

The glioma cells injection (red dotted region) and tumour border (yellow dotted region) for Glioblastoma-2 mouse for day 3 day and day 14 respectively are shown in Figure 4-26(c-d). However, the delineation of the GBM tumour margin cannot be easily confirmed only from the angiographic or en-face OCM structural images, but the size can be estimated by looking at cross-sectional images [Figure 4-16(e-h) – Figure 4-23(e-h)]. The injection area has remained avascular and has a similar size for the control mouse till day 14, and it can be clearly observed in Figure 4-24. The presence of a malignant tumour in the mouse brain was completely confirmed from the histology (HE staining) images by evaluating the size and structure of the GBM tumour and thereby comparing it to the structural OCM images [17]. Nevertheless, between day 3 and day 11 for both mice with Glioblastoma [Figure 4-25(b,d) and Figure 4-26(b,d)] there is observed an intense, significant difference in the size of the tumour growth (yellow dotted regions) marking an increase in vascular density. The structural images obtained for the control mouse in the injection region (yellow dotted region) show avascularity till day 14, as shown in Figure 4-24(b-d). Based on complementing both cross-sectional images [Figure 4-19(e-h) – Figure 4-21(e-h)] and en-face angiographic images [Figure 4-19(a-d) – Figure 4-21(a-d)], the delineated potential tumor extended was represented by yellow dotted lines in Figure 4-25(e-h). It was estimated

to be 0.6 mm, 2.0 mm and, 2.3 mm for day 3, day 11, and 14, respectively, for the Glioblastoma mouse.

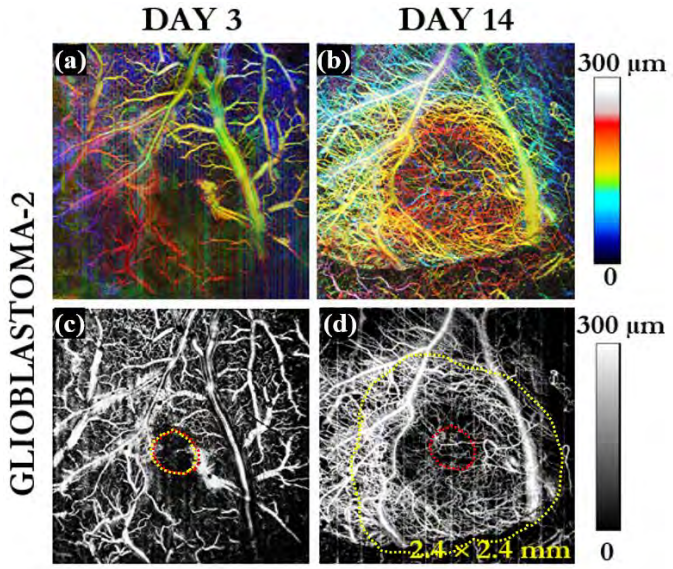

Figure 4-26 The colour-coded angiography images of the second mouse with glioblastoma (Glioblastoma-2) were acquired on day3 (left) and day14 (right), and the colour bar represents the z-axis. The yellow dotted region indicates the tumour border, whereas the red dotted region indicates the trace of the needle after injection.

The structural angiography obtained from the OCM system also revealed the characteristic structure of the glioma growth, evident during days 7, 11 and day 14 as shown in Figures 4-25(e-h) in yellow dotted regions. The comparison in the course of the process of neovascularization for two days: day 3 [Figure 4-26(c)] and day 14 [Figure 4-26(c)] along with the depth encoded representation of the angiography [Figure 4-26(a-b)] for Glioblastoma-2 mouse was demonstrated. Figure 4-27(a-d) shows the depth segmented angio layers obtained for Glioblastoma-2 mouse for day 14 with a depth of ~300 µm, mostly focussed on representing the four depth layers: (a) 0-50 µm, (b) 50-100 µm, (c) 100-200 µm, (d) 200-300 µm. The core region of the glioma tumor is the place of necrosis, whereas the periphery is the place of angiogenesis, and it can be clearly seen in the region with blue stars. We have assessed different cortical depths and the diversity of the GBM tumour structure for 14 days.

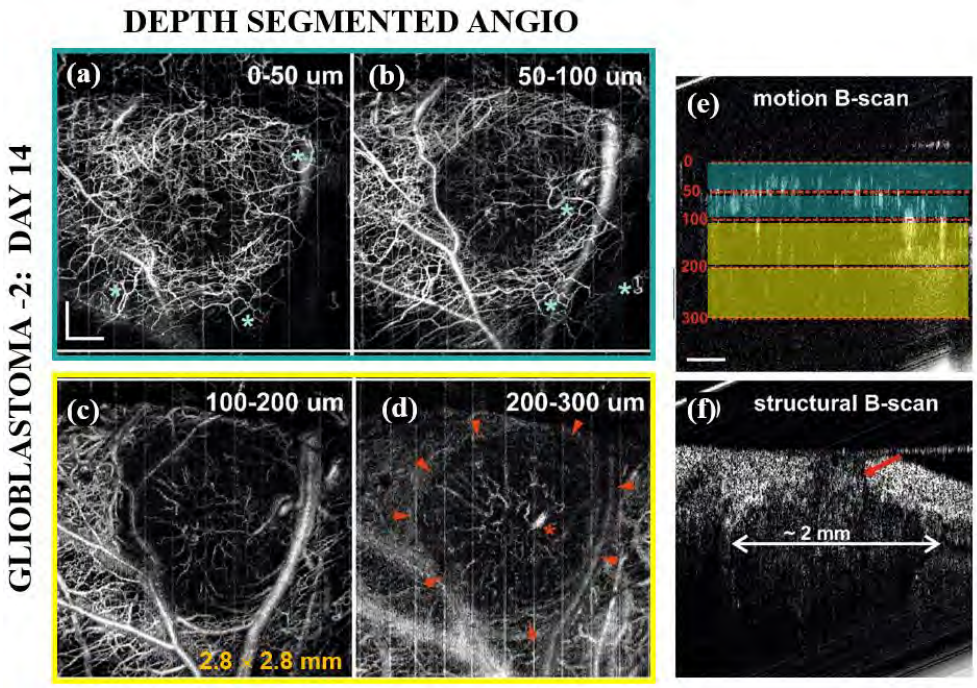

Figure 4-27 The angiography depth segmented glioblastoma at different depth (a) 0-50 µm, (b) 50-100 µm, (c) 100-200 µm, (d) 200-300 µm (e) the motion B-scan and (f) structural B-scan obtained on day14 for the second set of the mouse. The red arrow shows the abnormality of the vessels, and the blue star shows the loops specific for glioma of a sprouting branch.

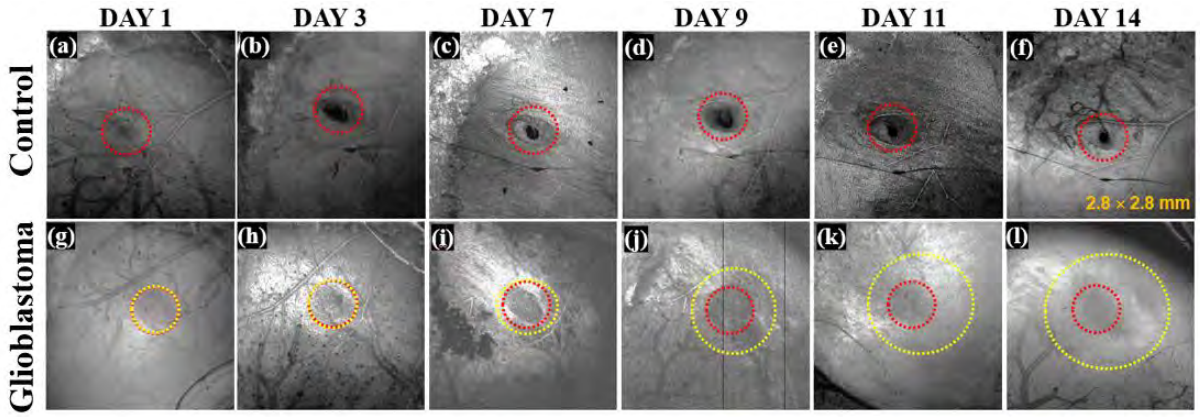

Figure 4-28 The structural images obtained by control (top) and Glioblastoma mouse (bottom) for day1, day3, day7, day9 and day14. The yellow dotted region represents the region of tumour injection, and the red dotted region represents the region of tumour growth.

Additionally, it was observed that the expansion of the GBM tumour is beyond the large vasculature on day14, and was clearly visible on structural en-face projections [in Figure 4-25(h)]. During the GBM tumour growth, the progression of angiogenesis is visible significantly on day 14 [in Figure 4-25(g)] compared to day 11 [in Figure 4-25(h)]. Figure 4-26 also shows the OCM-A data obtained for the second set of mice with a GBM tumour. In both cases, quite similar angiogenesis and neovascularization process was observed, leading to the distinguishable morphological features: tortuous, tangled, and irregular microvasculature in tumor proliferation. The size of the tumour was estimated to be approximately 1.8 mm (length)

× 2 mm (width) × 3 mm (depth). The approximate tumour margin (red dotted region) is shown in the structural angiography image on day 7, day 9 and day 14, as shown in Figure 4-28(g-l).

4.4.3 Angiogenesis and Fractal analysis for GBM tumour dataset

Tumour was often described as the uncontrolled and abnormal growth of the tissue. Angiogenesis is the « physiological process for de novo vascular network formation from pre-existing blood vessels » [263]. During the tumour growth process, the blood vessels undergo significant changes in size, vessel diameter, junction density, vessel length, morphological, and structural changes from a few microns to an order of hundreds of microns. The advantage of using evaluation points to measure the physiological phenomena like the length of the sprouting vessels (Sprouting vessels are the ones formed from the existing blood vessels), vascular density, number of sprouting vessels. These parameters yield promising results to evaluate the tumour state and a better understanding of the growth process. There are a variety of vasculature metrics like lacunarity, fractal dimension, vessel area, average vessel length, number of endpoints, number of junctions, vessel density and, vessel junction density are developed for the tumour evaluation in order to access both the diagnosis and study of the growth progression in tumour {Brú, 2008 #518}.

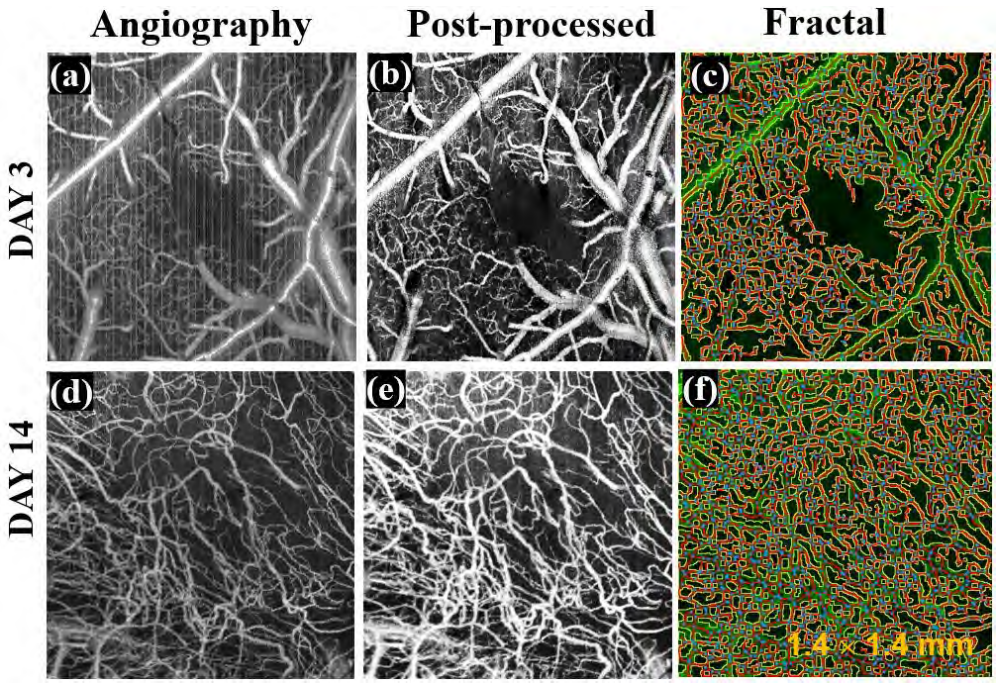

Figure 4-29 The angiography images of the GBM tumour mouse the angiography, post-processed and fractal analysis respectively for obtained for (a-c) day 3 and (d-f) day 14.

The contrast of OCM is not enough to image the longitudinal progression of the brain tumour due to the variation in the scattering properties over time. We have performed fractal analysis

to evaluate the angiogenesis process by skeletonizing the OCM-A microvasculature data acquired for GBM tumours over different time points over 14 days. The GBM tumour was imaged, and longitudinal growth progression was obtained using OCM-A for day 3 [Figure 4-29(a)] and day 14 [Figure 4-29(a)] was analyzed in the cortical region of the mouse brain. The angiography images obtained after post-processing steps as shown in Figure 4-29(b,e) after background removal, artefact removal along with median and FFT filtering was obtained. Their corresponding fractal analysis on GBM tumour progression is shown in Figure 4-29(c,f) for a day 3 and day 14 days, respectively. The fractal analysis is a solid indicator for demonstrating progression and evaluate the angiogenesis process during tumour growth. The rate of growth of the tumour at different time points can be quantified using fractal parameters such as the total number of junctions, average vessel length, vessel area and junction density. The sudden increase in these values over time show the rapid progression of a tumour. The fractal analysis was performed by skeletonizing the OCM-A microvasculature data acquired for the GBM tumour over a period of time.

4.4.4 Quantitative analysis of GBM tumour

This work aimed to propose and demonstrate an analytical method based on OCM imaging. The process of vascularization during the glioblastoma tumour growth was proven in the literature, but it was not shown for in-vivo imaging using ~ 2-5 μm resolution for the angiography image.

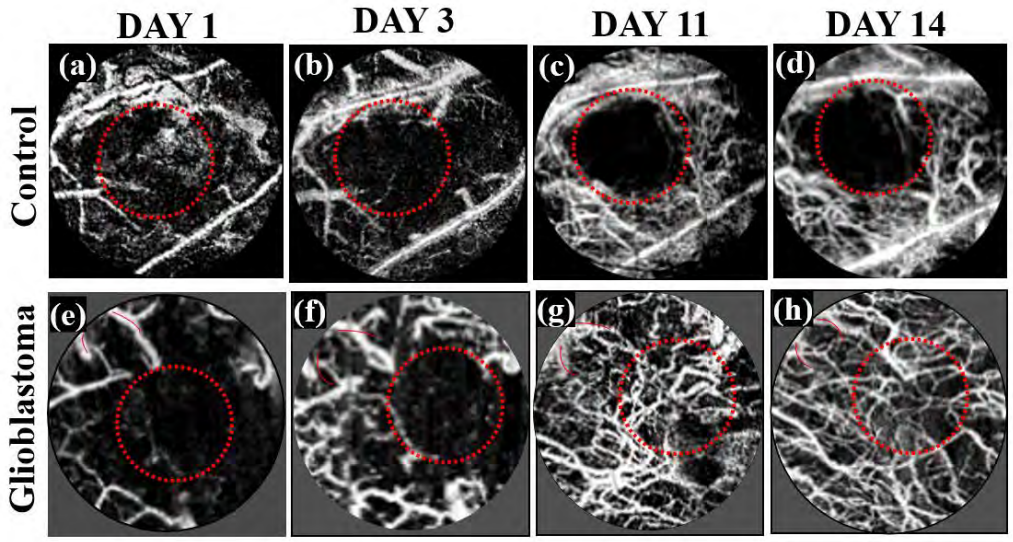

Figure 4-30 The microvasculature obtained for (a-b) control mouse (e-h) Glioblastoma mouse for the 1, 3, 11 and 14 days (from left to right) with a red dotted circle indicating ROI chosen for analyses.

The goal was to show the vascularisation changes of the tumour recorded on the OCM images, which are spectacular and quantified for the progression. The fractal analysis is performed on the ROI region of the vessel network of en-face angiographic projections to obtain the morphological parameters such as the total number of junctions, the total number of endpoints, vessel area and total vessels length was shown in Figure 4-30.

The angiography images were cropped to have the same region of the microvasculature, and the results are shown in control mouse [Figure 4-30(a-d)] and for the second set of Glioblastoma mouse [Figure 4-30(a-d)] for the 1, 3, 11, and 14 days. The red dotted circle is the ROI chosen for analyses.

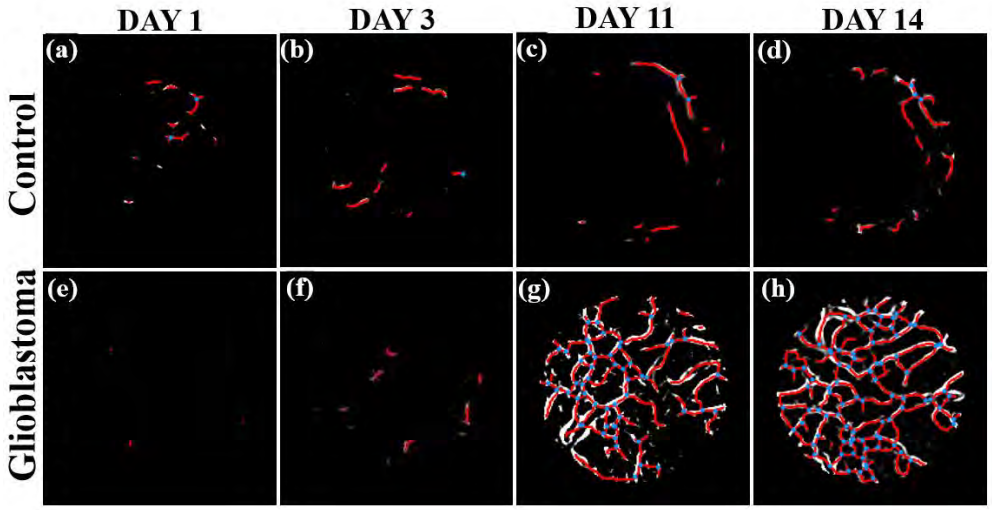

Figure 4-31 The selected ROI after applying the post-processing methods (Frangi-Hessian filter) and the Fractal transformation for (a-b) control mouse (e-h) Glioblastoma mouse for day 1, day 3, day 1 and day 14, respectively. The blue dots represent the junctions, and the red curves indicate vessels.

The selected ROI for day 1, day 3 control mouse [Figure 4-31(a-d)] and Glioblastoma mouse [Figure 4-31(a-d)] are avascular and fractal parameters analyzed at low levels for both control and glioma groups.

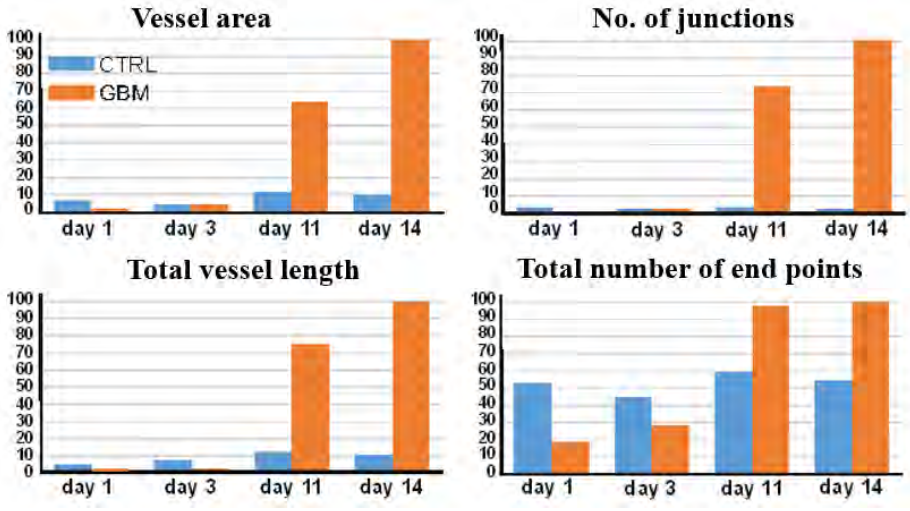

Figure 4-32 The four morphological parameters: vessel area, number of junctions, total vessel length and the total number of end points characterizing the microvasculature of the GBM tumor in comparison to the control mouse.

The diameter of the avascular area was estimated at around 0.7 mm in the selected ROI. The four morphological parameters: vessel area, number of junctions, total vessel length and the total number of end points characterizing the microvasculature of the GBM tumor in comparison to the control mouse. The morphological parameters such as vessel area, number of junctions, total vessel length and the total number of end points were used to characterize the progression of the microvasculature is shown in Figure 4-32 for day 1, day 3, day 11 and day 14 for the GBM tumor in comparison to the control mouse. A dramatic increase in all morphological parameters on day 11 clearly indicates the potent angiogenesis for the GBM mouse. The further increase in these parameters was observed for day 14. Whereas the characterization parameters in the selected ROI remained at low levels over the total period of investigation.

The results on the control mice (after buffer injection) confirm unequivocally that the neovascularization observed results from tumour growth. This method of OCM-A imaging allowed to monitor the physiological changes and angiogenesis in brain structure with extra control of interpreting the natural and fundamental biological process of tumour growth. These results show promising results to analyze brain plasticity during tumour growth and progression within 15-20 days. Several factors can affect the angiography data: the mouse has a different cerebral microvasculature, orientation, and organization size. It also depends on the age and weight of mice.

Nevertheless, we have observed tumor neovasculogenesis mice (which is the key feature in both mice injected with Gl261 implantation. This was also confirmed from the quantitative

fractal analysis and structural angio OCM images. Based on complementing cross-sectional images and en-face images, we delineated potential tumor extent (average diameter of the tumor: day 3 – 0.6 mm; day 11 – 2.0 mm; day 14 – 2.3 mm), presented on en-face images dotted yellow lines visible in Figures 4g-4l. We also presented the results showing the capability and sensitivity of the OCM system for the application of longitudinal imaging and progression studies of the GBM tumor microvasculature without the use of any contrast agents.

4.5 Contrast enhancement of nanorods and intralipids

4.5.1 LGNRs sensitivity in the water

The LGNRs were prepared in water at concentrations ranging over five orders of magnitude ranging from 50 fM (≈2 × 10^7 NPs/ml) to 5 nM (≈2 × 10^{12} NPs/ml) for dilutions from 1:1 to 1:100. We used Gaussian OCM (G-OCM) system with a super-luminescent diode (SLD) as laser source with central wavelength at 870 nm, FWHM 180 nm and 146 microwatts (mW) output power at the sample for all the experiments with LGNRs.

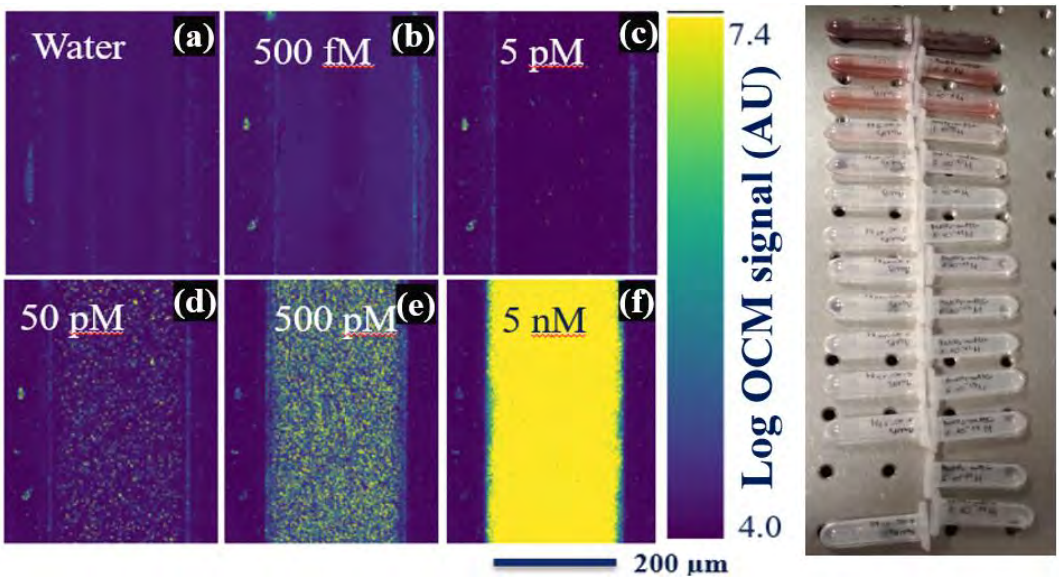

Figure 4-33 (a-f) The measured Log OCM signal intensity for various LGNRs concentrations in water (ascending order) in rat blood. The LGNRs sample prepared with different concentrations (right). Evaluation of LGNR contrast and circulation time in blood in vitro. The Colour bar represents the signal intensity.

The rat blood was chosen for the experiments because the total blood volume (TBV) for an adult mouse is only ~1.46 ml, whereas, for an adult rat, the volume is 25.6 ml [264] which would be sufficient for the experiments. The home-built G-OCM was used to detect and characterize the large gold nanorods (LGNRs) with 50 pM sensitivity in freshly collected whole

rat blood. The bare and mPEG-LGNRs were injected into the microfluidic channel with rectangular-shaped glass with a capillary of 200 × 200 µm dimensions. The LGNRS are circulated in water at different concentrations, and OCM signal intensity was measured. Every time the microfluidic channel was cleaned with water to ensure the right concentration and remove the leftover LGNRs from the previous injection. The low concentrations such as 1fM have been incremental steps of 10-15 measurements up to 10 nM were injected. The measurements for water alone was performed to subtract its contribution from the LGNRs. The final raw B-scans obtained after processing were averaged from 194 consecutive B-scans for a single measurement and was used to calculate all ROIs. The Log of OCM intensity with increasing concentrations of LGNRs in rat blood is measured and plotted in Figure 4-33. The results show an increase in OCM signal contrast from blue to green-yellow, as shown in Figure. 4-33(a-f) with an increase in concentrations. Below 50 pM, the OCM signal dependence with concentration is roughly linear. However, the OCM signal at higher LGNR concentrations increases by $\sqrt{N}$ dependence. The interference effects cause the signal to increase with a square root dependence on the number of particles within a voxel intensity and concentration at the higher concentrations. At sufficiently high concentrations of LGNRs, the observed OCM signal had deviated even further from the $\sqrt{N}$ prediction.

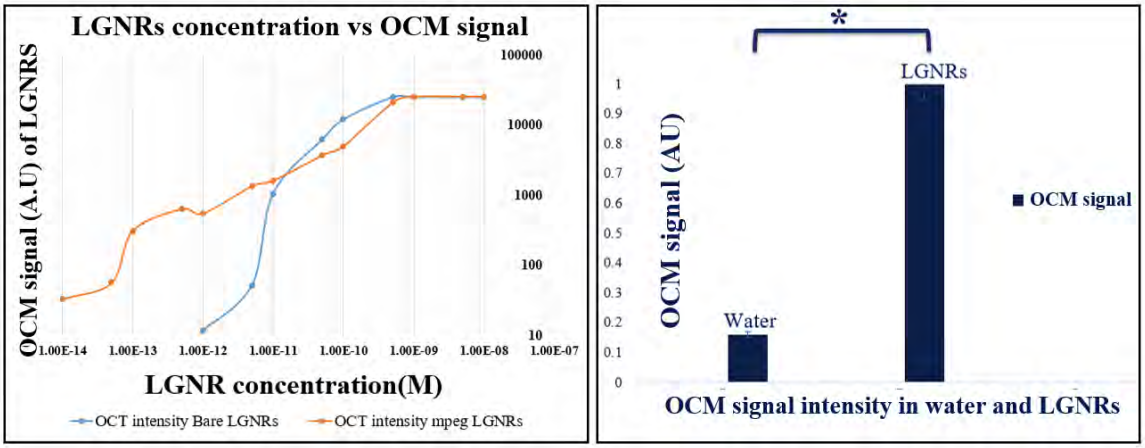

Figure 4-34 (a) Mean measured OCM signal intensity after subtraction of contribution from water in the ROI (Region of Interest) as a function of LGNRs concentration for bare LGNRs (blue) and mPEG (red) of experimental data and (b) OCM signal intensity variation in water and LGNRs.

For the ROI [Figure 4.33(f)], the total mean signal intensity from the OCM was calculated and plotted in the graph as a function of OCM signal at different concentrations for both bare LGNRs (blue) and mpEG LGNRs (red), as shown in Figure. 4-34(a). The variation in OCM signal intensity in the difference in water alone and LGNRs were shown in Figure. 4-34(b). Moreover, the Figure. 4-34(b) clearly demonstrate almost ten orders of magnitude increments

between the OCM signal in water and LGNRs. We assume that the same trend applies to the measurements of LGNRs in blood. The relation between OCM signal and particle concentration were agreed with the literature [249]. Our experiments could accurately quantify the signals produced by exogenous scattering agents (LGNRs) using OCM with the microfluidic channel.

4.5.2 LGNRs sensitivity in mouse ear

The m-PEG LGNRs were prepared in water at a concentration of 23.5 nM in 0.4 mL, and the first and second rounds of injection were performed with the same concentrations. We performed an intravenous injection into a living mouse near the neck vein with 400 µL of 23.5nM concentration to the right ear pinna, and the data was acquired using the OCM system. The mPEG-LGNRs was centred at 795 nm wavelength with a size of 100 × 30 nm (length × width) was injected into the neck vein with a volume of 100 µL of 5 nM mPEG coated LGNRs. The experiments were performed with a time of 1 min to 1h observation. The data analysis for angiography enhancement and post-processing methods were used for background nullification. The OCM imaging of the right ear pinnae of living mice was obtained after following mPEG-LGNRs subcutaneous injections: before injection of LGNRs (t = 0) [Figure 4-35(a)] and after the first round of injection of LGNRs at t = 2 min [Figure 4-35(b)], t_1 = 10 min [Figure 4-35(c)] and second round of injection at t_2 = 20 min [Figure 4-35(d)] was obtained. The representative angiography images before and after intravenous injections show no increment in the OCM signal intensity. Moreover, there was no prominent enhancement in the vasculature in the ROI (yellow dotted region) before and after injection of LGNRs, as shown in Figure 4-35. It is to be noted that there is a change in the region of imaging of vasculature, and it can be seen from the shift in the position of the vessels (red arrow). Indeed, some vessels have shown an enormous drop in signal from vessels after injection, as shown in Figure 4-35(b-d). There was no aggregation of LGNRs before the experiments, and it was confirmed using scanning electron microscopy (SEM) images. So, the shift in vascular positions could be the change in focus in the imaging region (red dotted lines). This could be attributed due to the huge movement of the mouse after the first round of injection of LGNRs. Another possible reason could be that the LGNRs concentration was too low for enhancement or the circulation time or the acquisition time did not fit in the regime, but all these cases are ignored since we ensured the proper parameters prior to and during the experiments. The OCM signal intensity was prominent in water (in section 4.5), but in the case of in-vivo mouse ear imaging, we did not yet observe a considerable difference in in-vivo mouse ear angio due to a change in focus position. Since the angiography can be viewed only after post-processing, it is difficult to check

the slight change in focus in raw B-scans making LGNRs difficult and unattractive for the in-vivo brain imaging.

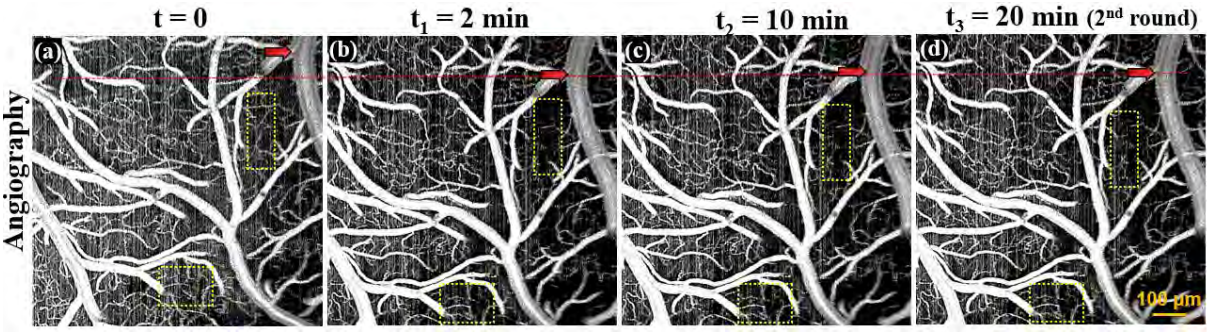

Figure 4-35 The angiography images obtained from OCM imaging of the ear pinnae of living mice (a) before at t = 0 min (b-c) after the first round of injection (t_1, t_2 = 2 min, 10 min) of LGNRs (d) after the second round of injection (t_3 = 20 min) of LGNRs.

4.5.3 LGNRs sensitivity in mouse brain

The LGNRs has an ability to exhibit 110-fold greater OCM signal per particle compared to conventional GNRs even with low concentrations of 250 pM in the in-vivo mice ear pinna [138]. However, the OCM signal enhancement was not verified for in-vivo brain imaging, and we have for the first time demonstrated the sensitivity of LGNRs for in-vivo brain imaging.

Gaussian-OCM (800 nm, ~6 fs)

The home-built Gaussian OCM system centred at 800 nm with a pulse width of 6 fs was used for the experiments in the mouse brain. The mPEG-LGNRs centred at 802 nm wavelength and size of 110 × 30 nm (length × width) are injected into the neck vein with a volume of 100 μL of 5 nM. The LGNRs are allowed to circulate for few minutes, and then the mouse brain is imaged at different time points: 5 min, 10 min, 15 min and 20 min during the experiment. The angiography images obtained from the imaging of mouse brain vasculature before injection at t = 0 min [Figure 4-36(a)] and after injection at time points: t_1 = 15 min [Figure 4-36(b)], t_2 = 20 min of LGNRs [Figure 4-36(c)] was demonstrated. The consecutive angiography images obtained at 0 min, 15 min, 20 min after injection was subtracted from each other, and their difference are shown in Figure 4-36(d-e), and the enhancement in the vascular signal was observed. The imaging position of the vascular region (red dotted line) did not get affected in this case after injection of the LGNRs. There is an enhancement of the vascular signal (yellow rectangle region) before and after injection

of intralipid [Figure 4-36(d-e)] and shows the potential of LGNRs to improve the contrast. However, the contrast of enhancement is not very huge in case of small vasculature.

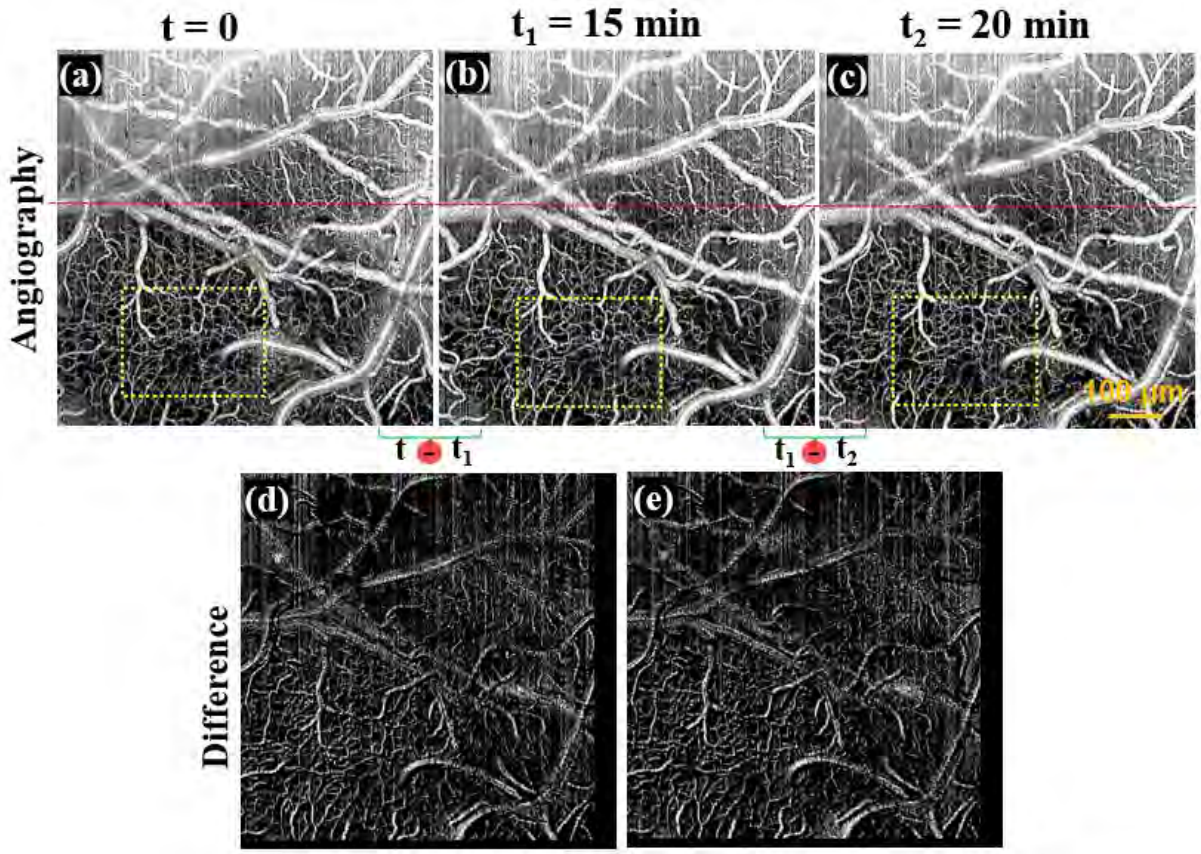

Figure 4-36 The imaging of blood vessels in mouse brain tissue of angiography images (a) before at t = 0 min and (b-c) after injection at t_1, t_2 = 15 min, 20 min of LGNRs (d-e) difference in the consecutive angiography images after injection of intralipid obtained for 0 min, 15 min and 20 min.

The motion B-scan images obtained before injection at t = 0 min [Figure 4-37(a)] and after injection at time points: t_1 = 10 min [Figure 4-37(b)], t_2 = 15 min [Figure 4-37(c)] and t_3 = 20 min of LGNRs [Figure 4-37(c)] is demonstrated. The consecutive motion B-scan obtained after every 5 min of injection up to 20 min images are subtracted from each other to observe the enhancement after LGNRs injection and is shown in Figure 4-37(e-g).

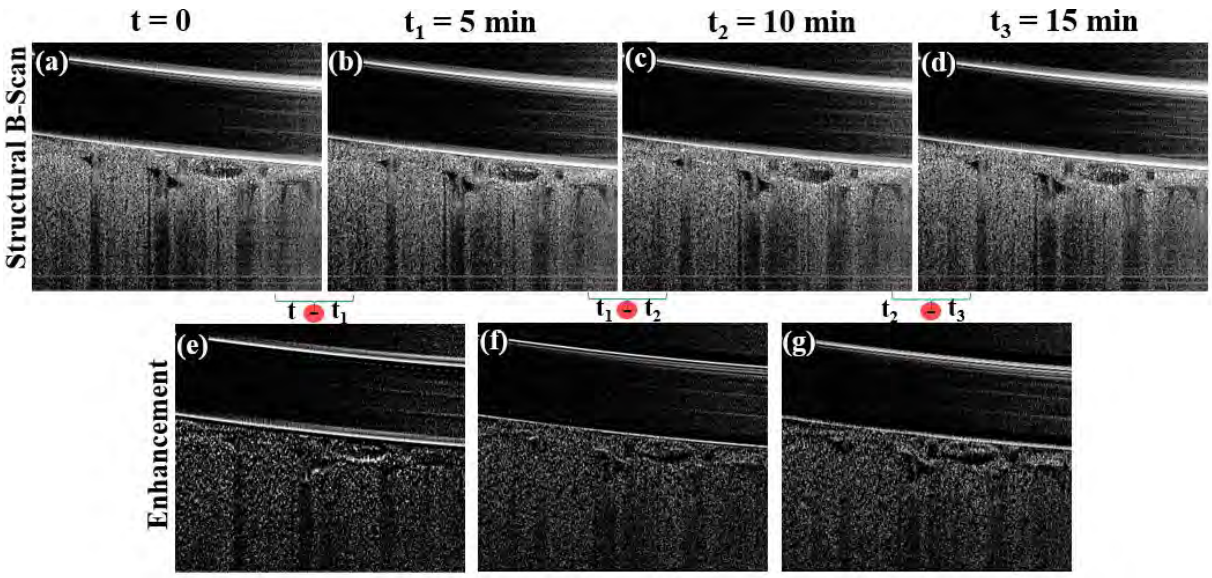

Figure 4-37 The imaging of blood vessels in mouse brain tissue and their motion B-scan images (a) before at t = 0 min and (b-d) after injection at t_1, t_2, t_3 = 10 min, 15 min, 20 min of LGNRs (e-g) difference in the consecutive angiography images after every 5 min of injection till 20 min.

We demonstrated the OCM imaging of the living mice brain imaging with mpEG-LGNRs and evaluated the enhancement. We imaged blood vessels in brain tissue before and after injection of LGNRs. The enhancement in small vessels is not very huge compared to large vasculature with LGNRs.

Gaussian-OCM (1300 nm)

The microvascular enhancement in the deeper region of the brain is important to study tumours and other diseased models. For this, we have used the Telesto PS-OCM system, centred at 1300 nm, to check the OCM vascular signal enhancement in small vessels. This system was optimized to achieve a high imaging depth (~2.5 mm) with 4.2 µm axial resolution (in the tissue). The mPEG-LGNRs with 100 nM concentration are injected into the mouse brain and circulated for a few minutes. There was no aggregation of LGNRs and was confirmed prior to the experiments using SEM images. The mouse brain was imaged, the angiography images were obtained before and after injection of LGNRs at different time points: t = 0 min (before injection), t_1 = 5 min (after injection), and t_2 = 15 min (after injection) of the LGNRs for the segmented superficial layer [Figure 4-38(a-c)] and deeper layer [Figure 4-38(e-f)] respectively.

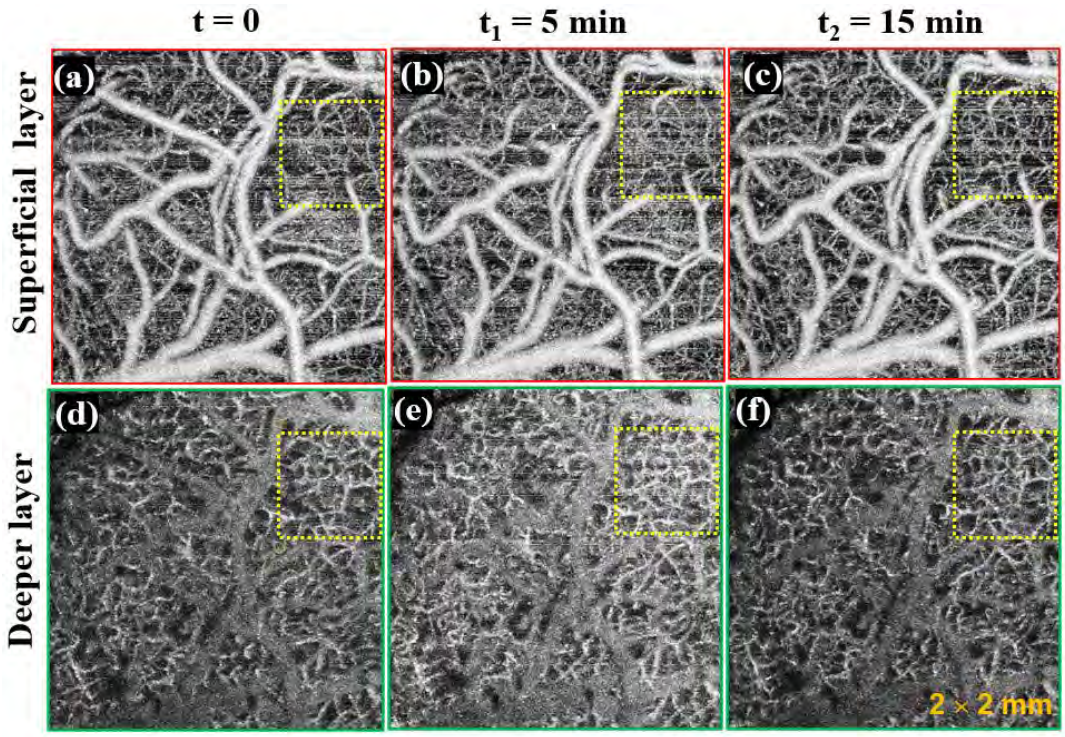

Figure 4-38 The angiography of the mouse cerebral vasculature at different time points: at t = 0 min (before injection) and t_1, t_2 = 5 min, 15 min respectively after injection of the LGNRs of the segmented for (a-c) superficial layers and (d-f) deeper layers.

The enhancement in the ROI (yellow rectangular region) for the segmented superficial layer [Figure 4-38(a-c)] and deeper layer [Figure 4-38(e-f)] of the cerebral angiography before and after injection of LGNRs is not very huge, even when measured with 1300 nm OCM system. Moreover, a huge vessel, as shown in Figure 4-39 (black rectangle dotted region) which was there before the injection of intralipid [Figure 4-39(a)] was disappeared after injection of the LGNRs [Figure 4-39(b)]. The possible reason could be that the LGNRs have caused a similar stroke in the mouse brain.

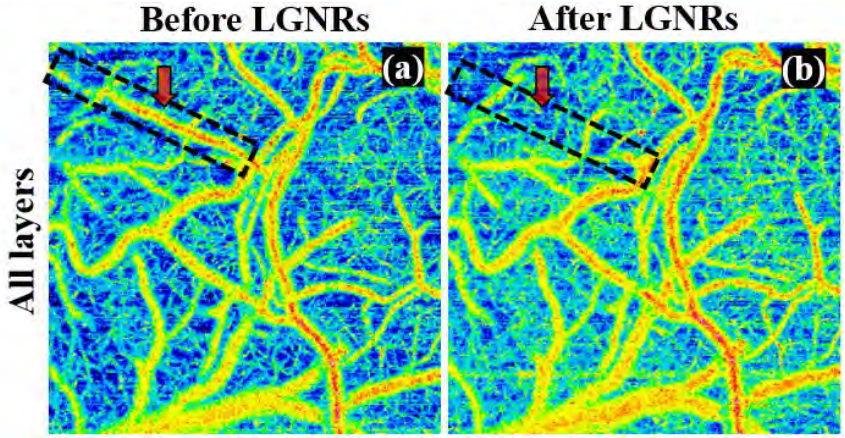

Figure 4-39 The in-vivo angiography images of the living mice brain microvasculature in the cerebral region (a) before and (b) after injection of LGNRs.

Sometimes there was a change in focus of the tissue imaging area due to the huge movement of the mouse after injection of LGNRs, which could be the possible reason for no signal improvement as seen in section 4.5.2. These experiments demonstrate the possible failures of the LGNRs for brain imaging: change of focus position after injection of LGNRs, conditions like stroke due to injection and a very little enhancement in the deeper microvasculature. There was a considerable enhancement for in-vivo brain imaging using LGNRs for the superficial layers, confirmed by using an 800 nm Gaussian OCM system. Nevertheless, there was little to no enhancement in the angiography of the deeper layer of the mouse brain microvasculature with LGNRs and was verified using the 1300 nm OCM system as shown in section 4.5.3. These observations question if the potential application of LGNRs to cerebrovascular studies, especially for longitudinal imaging, is significant and advantageous? Moreover, no available literature studies are showing the OCM signal enhancement using LGNRs for brain imaging. We are the first group to apply the mPEG-LGNRs for cerebral studies, and we found that LGNRs are not a suitable candidate for contrast enhancement for in-vivo brain imaging due to the above reasons.

4.5.4 Intralipids sensitivity in mouse and rat brain

The intralipids are non-toxic scattering contrast agents for in-vivo brain tissue imaging [108, 164, 265]. But our interest was to have an OCM signal enhancement, especially in deeper microvasculature of the brain. However, there are no available studies that quantify the sensitivity and show the enhancement percentage, especially in the deeper microvasculature using OCM-A. For the first time, we have quantified and evaluated the potential enhancement without intralipids using our new method in the in-vivo mouse brain for the deeper layers of the mouse brain tissue using both 800 nm and 1300 nm Gaussian OCM system. We also evaluated the contrast enhancement with a 1300 SS-OCM system with high axial and transverse resolution.

To understand the effect of the intralipids as contrast agents and quantify the increase in OCM signal contrast, we performed experiments on in-vivo imaging of mouse and rat cerebrovasculature with dura intact to the skull Gaussian OCM. The size of intralipids being smaller than RBC's, the scattering of intralipids are more proportionate at 800 nm wavelength than 1300 nm. Nevertheless, we used both wavelengths to study the potential OCM signal enhancement with intralipids in both superficial and deeper microvasculature. The experiments with intralipid with 1300 nm and 800 nm would reference the contrast enhancement for our studies.

Gaussian-OCM (800 nm, ~6 fs)

The Gaussian beam OCM instrument using broadband superluminescence (SLD) diode laser operated at central wavelength 870 nm with FWHM 180 nm was used for intralipids experiments. The theoretical axial resolution is 2 - 3 µm for a depth resolution of 300 - 400 µm makes it very good to study the deep microvasculature with good spatiotemporal resolution. The power used in the sample was 400 µW, and the acquisition time is 20 µsec for a single A-Scan. The 3-D information of the mouse brain also can be rendered even for small capillaries were also resolved and distinguished. The intralipid of 300 µL was injected into the mouse brain through an intracarotid vein - neck vein injection through a tube. The total time of injection was less than a minute. The mouse was imaged during and after injection of intralipid. The total time of injection was 10-15 seconds for both the injection, and mice were scanned for 2-5 minutes and simultaneously to OCM data was acquired before, during and after injection of intralipid for several minutes. Figure 4-40 depicts the cross-sectional motion B-scan (left) of the healthy mouse brain before (top row) and after 10 minutes of injection (bottom row) along with five depth segmented angiographic layers. We can observe that there was strong evidence of OCM signal enhancement after injection of intralipid in Figure 4-40.

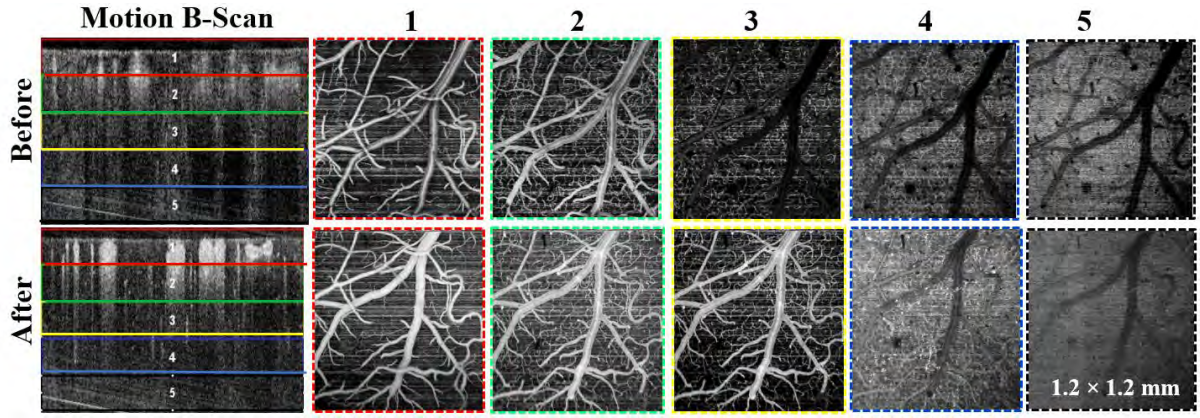

Figure 4-40 The depth segmentation of the healthy microvasculature of mouse brain before (top) and after (bottom) injection of the intralipids with 800 nm Gaussian OCM system. The first column contains the cross-sectional images before (top) and after injection (bottom). Each segmented layer consists of 50 pixels in depth.

The segmented depth images (green and yellow) clearly depict that the blood vessels in deeper regions are strongly visualized and distinguished before and after injection. This clearly shows that the capability of the OCM system to achieve the results without removal of dura and reduction of shadowing artefacts was achieved. To achieve this result involves proper care and various factors such as a good OCM system, proper focus position, the accurate amount of the

intralipid injection, good quality cranial window and alignment techniques. These results also agree with the literature [165]. The contrast enhancement using Gaussian OCM for the cerebral region in the mouse brain was made on the small region of the vasculature with the field of view (FOV) of 0.5 × 0.5 mm since the time of acquisition is less than one-round of blood circulation time in a mouse which is approximately 15-22 seconds [266]. This enables to capture of the enhancement of the RBC's during a single circulation time. The angiography images were obtained from the mouse cerebral vasculature at different time points: before injection t = 0 [Figure 4-41(a)] and after injection of intralipid at t_1 = 1 min [Figure 4-41(b)], and t_2 = 2 min [Figure 4-41(c)] is shown in Figure 4-41 (top).

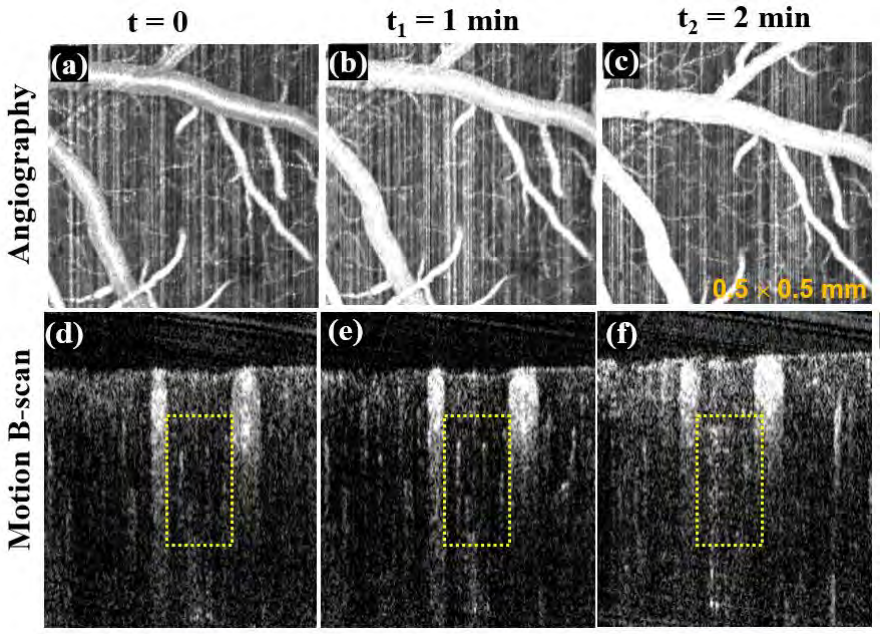

Figure 4-41 The OCM imaging the living mice brain vasculature in one blood flow circulation time depicted for (a-c) angiography images and (d-f) motion B-scans at time points t = 0 min (before injection) and after injection at t_1 = 1 min and t_1 = 2 min of intralipids.

Whereas, the enhancement in motion B-scans was shown in Figure 4-39 at different time points: before injection t = 0 [Figure 4-39(d)] and after injection of intralipid at t_1 = 1 min [Figure 4-39(e)], and t_2 = 2 min [Figure 4-39(f)] is shown in Figure 4-39 (bottom). The yellow dotted rectangular region shows a clear enhancement in the OCM signal before and after injection of intralipid in one single blood circulation time. These results demonstrate the potential of 800 nm G-OCM for the contrast enhancement in the mouse cerebrovascular and agree with the results in the literature [103, 108, 165].

Gaussian-OCM (1300 nm)

The cerebrovascular enhancement in the deeper region of the mouse brain is studied using the Telesto PS-OCM system, centred at 1300 nm. The OCM vascular signal enhancement with intralipids in small vasculature can be quantified efficiently as this system was optimized to achieve a high imaging depth (~2.5 mm) with 4.2 µm axial resolution (in the tissue). The mouse brain was imaged, and the angiography image was obtained before intralipid injection as shown in Figure 4-42(a-c) and after injection of intralipids as shown in Figure 4-42(d-f) for all layers [Figure 4-42(a,d)], the segmented superficial layer [Figure 4-42(b,e)] and deeper layer [Figure 4-40(c,f)] respectively. There is the enhancement in both the superficial layer (red dotted rectangle) and the deeper layer (green dotted rectangle). These results are consistent with the literature and the enhancement in the deeper region of the cerebral microvasculature [108, 162, 164].

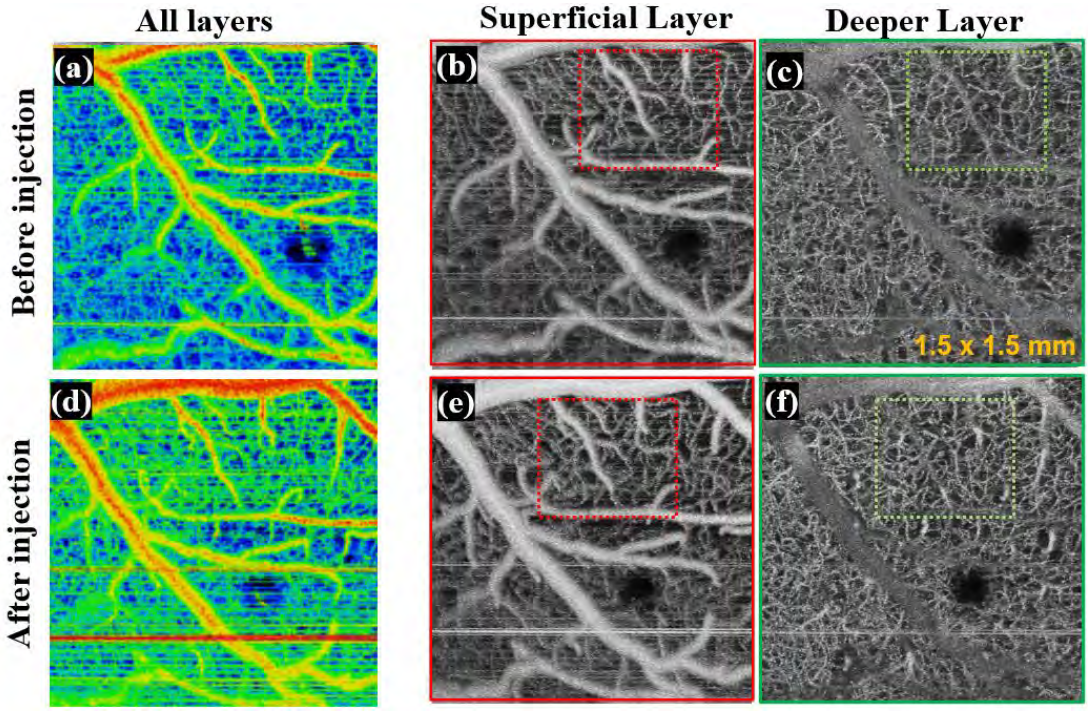

Figure 4-42 Wide-field angiographic map of the cerebral microvasculature with 1300 nm Gaussian OCM system before (top) and after (bottom) intralipid injection for all layers, superficial layers and deeper layers (from left to right).

Wavelength - Swept Source OCM (1300 nm)

The wavelength-swept source OCM (SS-OCM) imaging system with 1300 nm central wavelength and an axial resolution (in tissue) and transverse resolution of 10 mm with an output power on the sample of 20 mW was used for the experiments on rat cerebrovascular imaging [19]. The advantage of using SS-OCM for the experiments of cerebrovascular enhancement provides superior visualization of the deep anatomy of the microvasculature, including the deeper vessels. The first intralipid of 500 µL was injected into the rat brain through direct neck

vein injection through a cather focusing on the superficial vasculature. The rat was imaged during and after injection of intralipid. The focus was moved to the deeper cerebral microvasculature, and the second dosage of 200 µL of intralipid was injected. The total time of injection was 1-2 minutes for both doses of injection. The rat was scanned for 20 minutes to acquire the OCM angiography data simultaneously. The right somatosensory cortex region of the rat brain, as shown in Figure 4-43 (left), depicts the microvasculature region of imaging (blue dashed lines) obtained from the CCD camera was used for imaging.

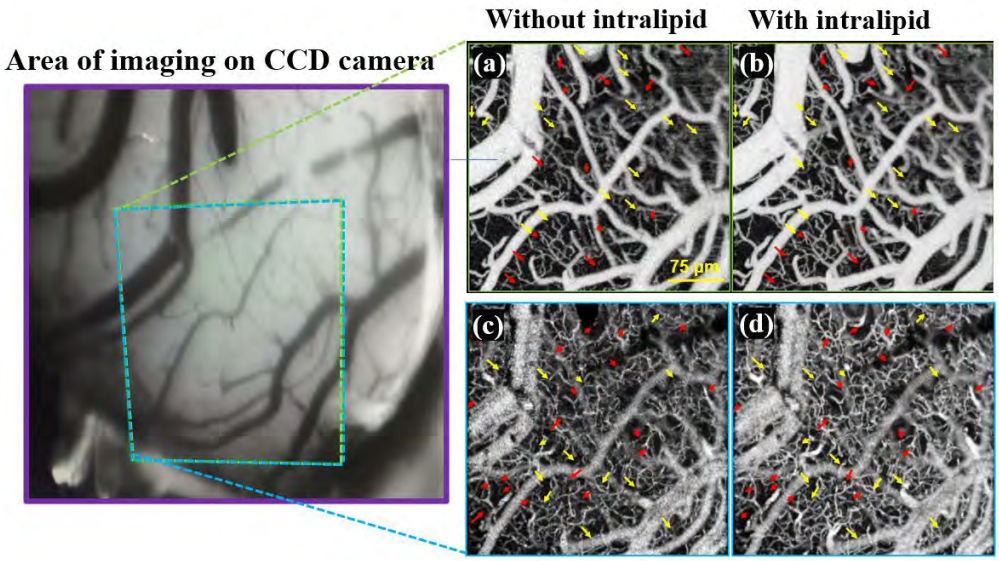

Figure 4-43 (a-b) Wide-field angiographic map of the corresponding rat cerebral microvasculature with 1300 nm SS-OCM system of the healthy rat brain depicting the enhancement before (left), and after (right) intralipid at the focus on the superficial vessels and deeper microvasculature, (c-d) with the change of focus to deeper region shows the enhancement before (left) and after (right) intralipids. Red arrows guided strong enhancement in the vasculature compared to before intralipid injection, whereas the yellow arrows show little enhancement in OCM signal after injection of intralipids.

The cross-sectional image of the en-face projection-angiography of the healthy rat brain before and after [Figure 4-43(a) and Figure 4-43(b)] injection of intralipid focused on the superficial vasculature is obtained. The angiography images focused on the deeper vasculature are also obtained before and after intralipid injection [Figure 4-43(c) and Figure 4-43(d)]. The red arrows and yellow arrows show a strong and little enhancement of the microvasculature before and after intralipid injection, respectively, as shown in Figures 4-43. This set of angiography data provides the possibility of a clear differentiation of the enhancement in the deeper microvasculature as the focus for superficial and deeper is done separately, and in addition, the 1300 nm SS-OCM provides a superior microvasculature visualization with high axial and transverse resolution. So, in this direction, we analyzed the difference in the enhancement of the microvasculature to focus on superficial and deeper layers. The angiography data were post-processed to remove the background and other artefacts. Figure 4-

42(c) shows the angiography image obtained after the subtraction vasculature focused at the superficial layer of the brain before [Figure 4-44(a)] and after [Figure 4-44(b)] injection of the intralipid. Whereas the angiography images resulted after the subtraction of microvasculature focus at the deeper layer of the brain tissue before [Figure 4-44(a)] and after [Figure 4-44(b)] injection of the intralipid.

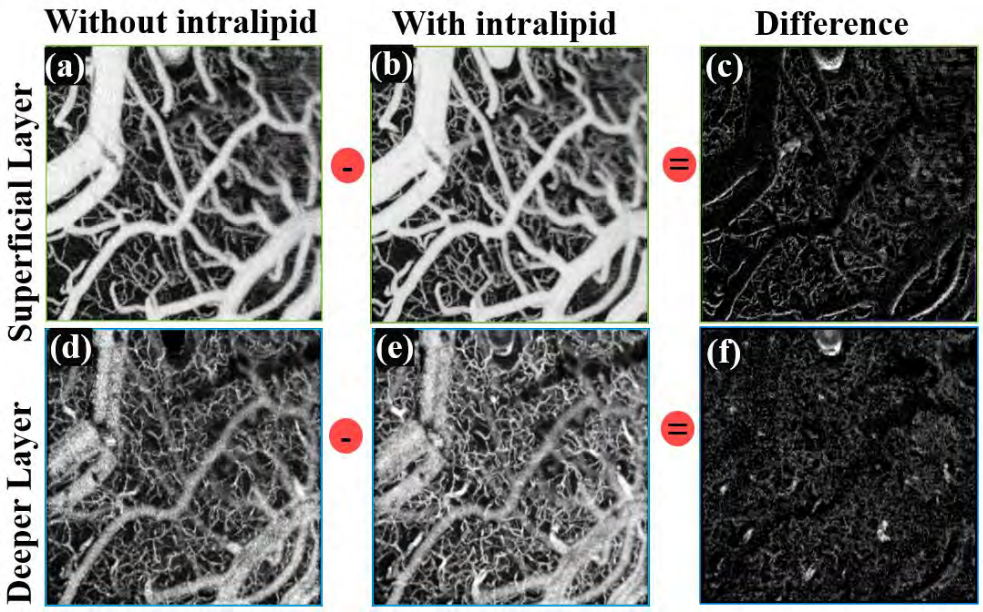

Figure 4-44 The SS-OCM imaging and enhancement (a-b) with and without intralipid injection for the focus on the superficial layer, (c) shows the difference in the enhancement of superficial vasculature, (d-e) with and without intralipid injection for the focus on a deeper layer, (c-f) shows the difference in the enhancement of the vasculature before and after injection of intralipid for the superficial and deeper layers.

We can observe strong evidence of enhancement in OCM signal after injection of intralipid, as shown in Figure 4-44(c-f) for both vessels focussed at superficial and deeper layers. The angiography images clearly depict that the blood vessels in deeper regions are strongly visualized and were distinguished before and after injection.

These results clearly show that the OCM system's ability to achieve the results without removing dura and reducing shadowing artefacts was achieved. The rat dura is thicker than the mouse, and the dura is intact with the rat brain. However, still, there is an enhancement of the microvasculature focus on superficial microvasculature [Figure 4-44(a-b)] and deeper vasculature Figure [4-44(d-e)] was clearly seen. It is also noteworthy that new capillaries that were barely visible with low intensity before the intralipids (red arrows and yellows arrows in Figure 4-44(a-d) are enhanced with better signal intensity after injection intralipid in both angiography with a focus on superficial and deeper layers. It was noted that although the OCM-A signal was increased after the intralipid injection, it is not yet clear that the vessels that we

could not distinguish before the intralipid injection. The results obtained show that only there is an enhancement in the signal intensity from the existing microvasculature, but no new microvasculature was seen before and after injection of the intralipid. We also evaluated the contrast enhancement with a 1300 SD-OCM system with high axial and transverse resolution.

The studies focused on enhancing superficial and deeper microvasculature is studies using a Gaussian OCM system centred at 800 nm [Figure 4-40] and 1300 nm [Figure 4-42] also shows an enhancement. The 1300 nm SS-OCM with high transverse and axial resolution is used to further quantify the improvement in small vessels [Figure 4-43] show the OCM signal enhancement. All of these results agree with the literature [88, 162, 165].

4.6 An alternate method for contrast enhancement

The intralipids are non-toxic scattering contrast agents for in-vivo brain tissue butthe speckle pattern looks different (small speckle pattern) due to the size of intralipid particles smaller than RBCs. Nevertheless, the results obtained from 800 nm and 1300 nm OCM systems show that intralipid can only enhance the OCM signal intensity from the existing microvasculature compared to before intralipid injection. The speckle pattern improvement and the strong variation in signal intensity in the backscattered light is observed when the OCM contrast is enhanced. There are two possibilties to acheive this without constrast agents. The first one is to have long exposure times to capture all the capillaries and other method is to average the consecutive angiography images. The first is limited to the spectrometer and system abilty, whereas the latter can be tested. The red blood cells (RBC's) can pass one at a time through the small capillary and are deformable when passed through the vessel, but still, their volume is preserved even when their shape changes [267]. However, the size of RBC (~ 0.01 mm) is similar to the order of capillary diameter (5 -10 μm). Hence there is only a narrow lubrication gap between the vessel wall and an RBC [268]. They formed a single file when they were advected through a capillary. This provides an opportunity to expose to a larger surface area and more time is available to capture all the RBC's flow in a capillary. The advantage we gain for OCM is that if the exposure time of the camera is shorter, we can capture all the RBC's passed in a capillary in one circulation time (15-22 seconds) and then we can achieve microvascular enhancement. But the disadvantage is it is limited only to a small field of view (FOV) and time of acquisition. We developed an alternative approach, which is to average the consecutive scans that make to capture all the RBC's in a capillary at different time points and achieve similar results without contrast agents. All the RBC's in the capillary cannot be

captured in a single image acquisition time unless the region of imaging is small. It is worthy of mentioning that contrast enhancement in intralipid is limited, and it does not change linearly, and the signal is constant after a certain period.Therefore, averaging consecutive scans will enable capturing all the RBC's in capillaries and enhance the microvasculature. The advantage of this is method is that we can achieve the results even in the larger imaging area of the brain, and this method would additionally allow monitoring the changes in the physiological and microvasculature changes in the brain without misinterpreting the effect of contrast agents in the fundamental biological process such as stroke, tumor growth and other diseased models. These results show promising results to enhance the microvasculature without using contrast agents and to analyze longitudinal progression and brain plasticity for several diseased models. We performed the experiments to prove our new method in the microfluidic channel with blood and in-vivo mouse brains using 800 nm and 1300 nm Gaussian OCM systems. The new method of contrast enhancement is shown in Figure 4-45(a), where the RBC's flow in a capillary is captured at different time points t_1, t_2, t_3 during the image acquisition time. Whereas Figure 4-45(b) shows the contrast enhancement in the microvasculature that can be achieved with intralipid achieved by averaging 'N' number of consecutive scans, which can be equivalent to a single scan with intralipid injection.

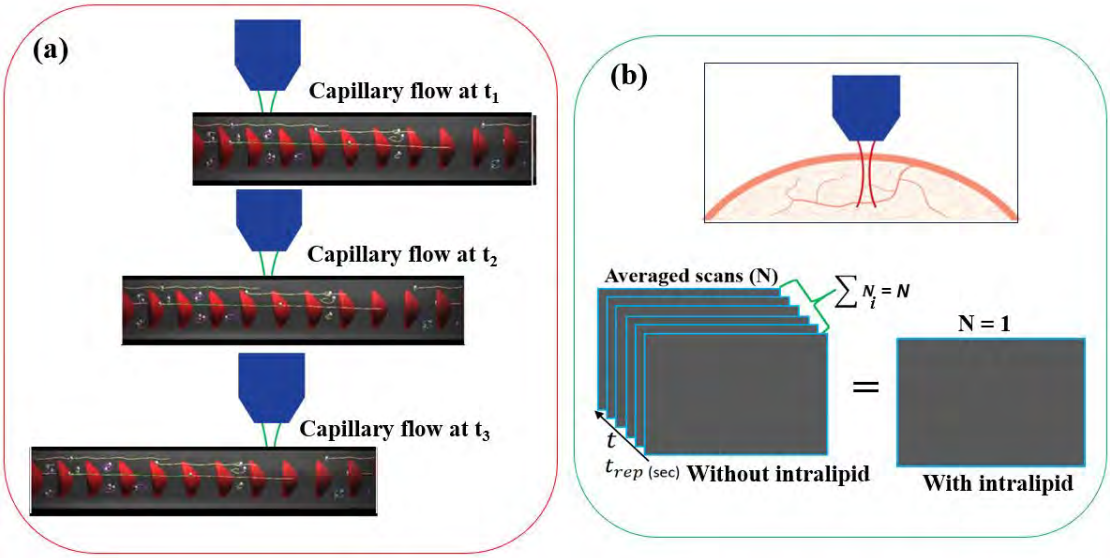

Figure 4-45 The new method of contrast enhancement (a) the RBC's flow in a capillary obtained at different time points t_1, t_2, t_3 (b) the contrast enhancement without intralipid achieved by averaging 'N' number of scans equivalent to the single scan with intralipid.

Verification in a microfluidic channel with blood

The microfluidic channel of 200 × 200 µm circulated with blood was imaged with cross-sectional locations (ROI), and the average one raw B-scan images consist of 194 consecutive

B-scans to calculate the ROI. The experiment was also performed with blood and a mixture of intralipid and blood in the microfluidic channel.

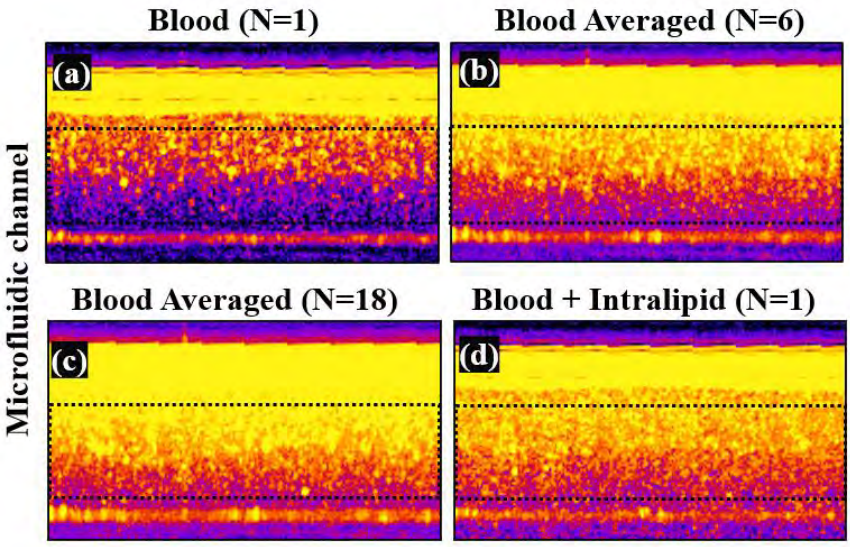

Figure 4-46 The microfluidic channel circulated with blood are averaged in the ROI (black dotted) region (a) the single scan of blood measurement (b) the averaged number of scans (N) of 6 with blood (c) the averaged number of scans (N) of 8 with blood (d) the single scan with blood and intralipid mixture.

The microfluidic channel circulated with blood for the averaged in the ROI (black dotted) region with a single scan of blood measurement [Figure 4-46(a)], the 6 averaged number of scans with blood [Figure 4-46(b)], the averaged 18 number of scans with blood [Figure 4-46(c)] and, the single scan with blood and intralipid mixture [Figure 4-46(d)].

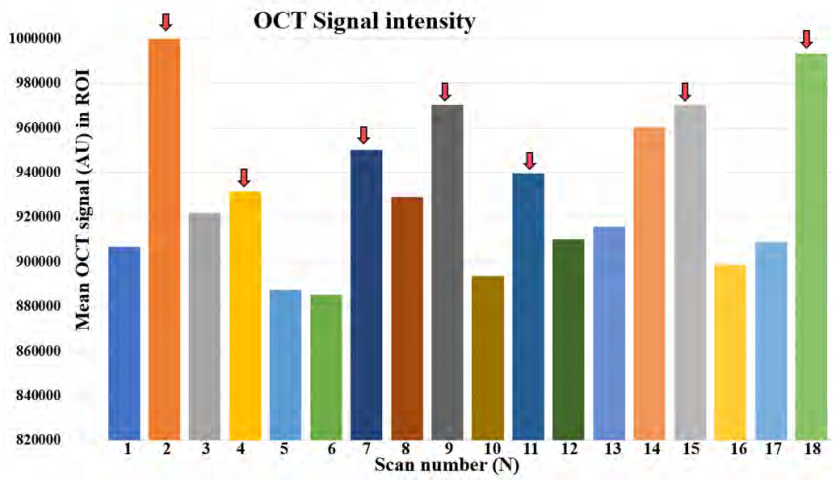

Figure 4-47 The graph showing the number of scans (N) as a function of the mean OCM signal intensity in the microfluidic channel. The red arrows represent the increase in the OCM signal at different scan points.

The graph in Figure 4-47 shows that the number of scans (N) as a function of the mean OCM signal intensity in the ROI region achieved in the microfluidic channel with blood. There is an

increase in the OCM signal, as shown in red arrows in Figure 4-47 at different scan points. This explains that more RBC's are captured at different time points and support our new method.

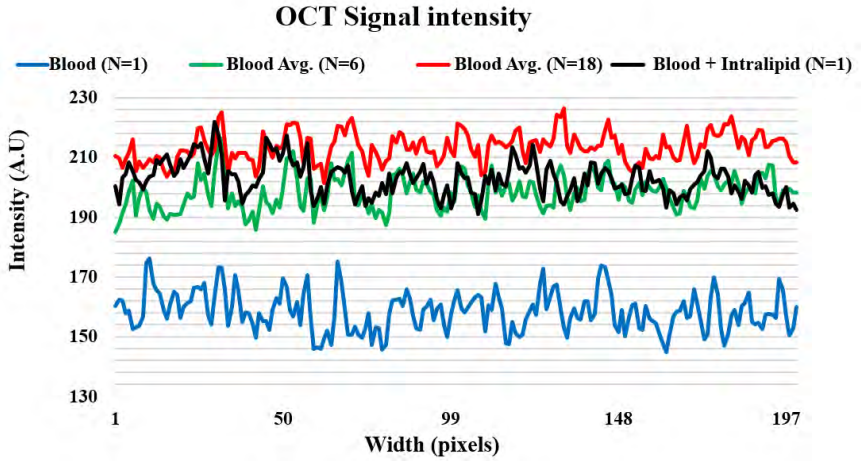

Figure 4-48 The OCM mean signal intensity variation across the microfluidic channel's width with blood averaged for N = 1,6, 18 and single scan for blood with intralipid.

The OCM signal intensity for the averaged ROI region for the microfluidic channel has plotted the function of the OCM signal intensity and width of the channel in pixels. The OCM mean signal intensity variation for the scans averaged for the microfluidic channel circulated with blood and averaged for N = 1, 6,18 and single scan for blood with intralipid is shown in Figure 4-48. This graph clearly shows that the enhancement in the ROI region for only 6 averaged numbers of scans with blood (green) is almost equivalent to the single scan of blood with intralipid (black). Also, averaging 18 consecutive scans (red) shows much higher OCM signal intensity than a single scan with blood and intralipid together (black).

Verification in in-vivo mouse brain

The new method was applied to the microfluidic channel with blood, and the OCM signal enhancement with averaging of only 6 scans is similar to intralipid is verified. Nevertheless, the final goal has the enhancement in the in-vivo mouse brain. For this, we have imaged mouse cerebrovasculature using 800 nm and 1300 nm Gaussian OCM system for verification of new method in both superficial and deeper vasculature. The mouse was injected with 300 µL of intralipid injection, and data were acquired before and after injection of intralipid.

Gaussian OCM (800 nm, 6 fs) system

The mouse was injected with 300 µL intralipid, and data were acquired before and after injection of the intralipid. The angiography images acquired before and after injection of intralipid are shown in Figure 4-49(a-b), with 16 scans averaged for both the data. Three regions

of interest (ROI) is chosen for the quantification for the region with large vessel - R1 (blue), background or noise without any vessel - R2 (yellow) and small vessel - R3 (green).

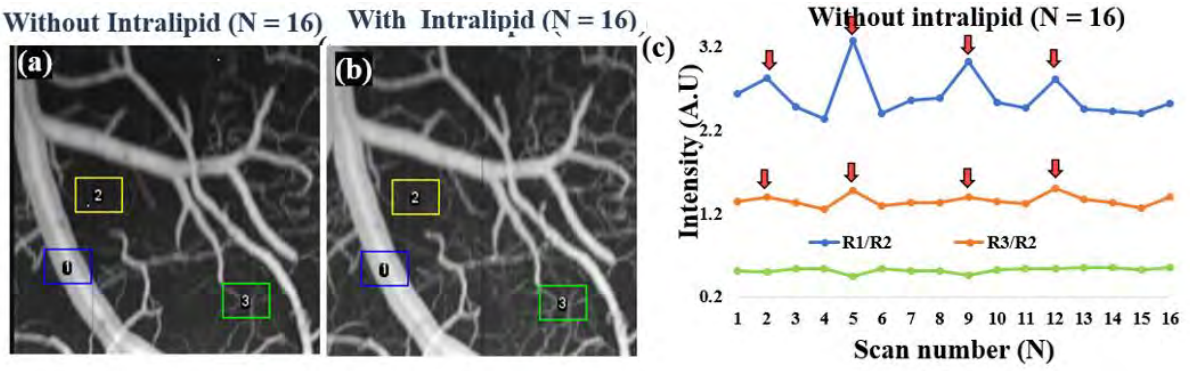

Figure 4-49 (a-b) The imaging of mouse cerebral vasculature with averaged number of scans (N = 16) in three different regions of interest (ROI) for a large vessel, noise and small vessel (c) the mean OCM signal intensity as a function of scan number for the ratio of ROI's.

The graph is plotted as a function of the OCM signal intensity across the ROI's for these three regions as the ratio of intensities which give the OCM signal for the contribution only from a large vessel $(R1/R2)$ and small vessel $(R3/R2)$ of the angiography data without intralipid for consecutive scan number was shown in Figure 4-49(c). The red arrows represent the increase in the OCM signal enhancement at different scan numbers. These results agree with our new method that at different time points, more RBC's are detected as the flow in capillaries is inconsistent with time. It is worthy of mentioning that contrast enhancement in intralipid is limited. After 12 scans, the OCM signal remained constant.

To prove our new method further and observe a clear enhancement in the microvasculature after injection of intralipid, the angiography data was depth segmented into superficial layer and deeper layers. The angiography of the mouse brain was averaged for 10 scans (N = 10) for the superficial region before [Figure 4-50(a)] and after [Figure 4-50(b)] of intralipid injection. Whereas the angiography for the deeper layer before [Figure 4-50(d)] and after [Figure 4-50(e)] injection of intralipid for the deeper region.

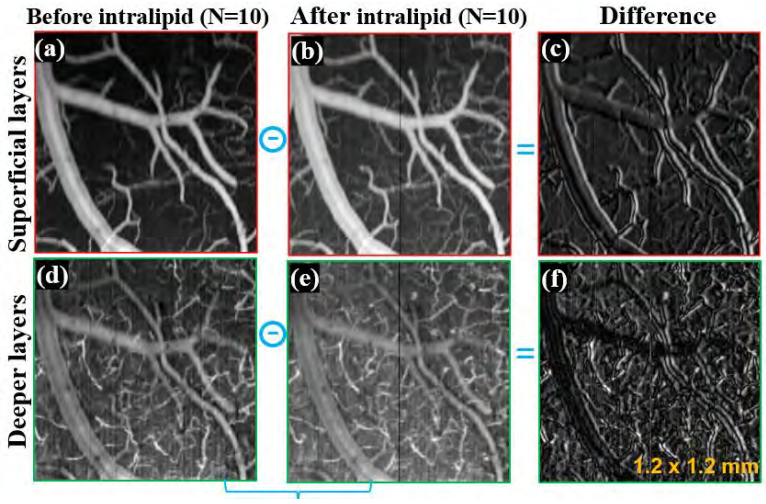

Figure 4-50 The angiography of mouse brain averaged for 10 scans (N = 10) using an 800 nm Gaussian OCM (a-b) before and after injection of intralipid for the superficial region, (d-e) before and after injection of intralipid for the deeper region, (c,f) the difference of angiography images showing the difference after injection of intralipid for the superficial and deeper regions respectively.

The difference in enhancement before and after intralipid injection in angiography images for the superficial [Figure 4-50(c)] and deeper [Figure 4-50(f)] regions, respectively. There is no huge difference in the enhancement in the deeper microvasculature after injection of the intralipid with an 800 nm Gaussian OCM system. To further analyze and quantify the enhancement, we have analysed the imaging parameters such as signal to noise ratio (SNR), C (speckle noise), a contrast to noise ratio (CNR) and dynamic range for three ROI's with large vasculature (blue), background (yellow) and small vasculature (green) before and after injection of the intralipid.

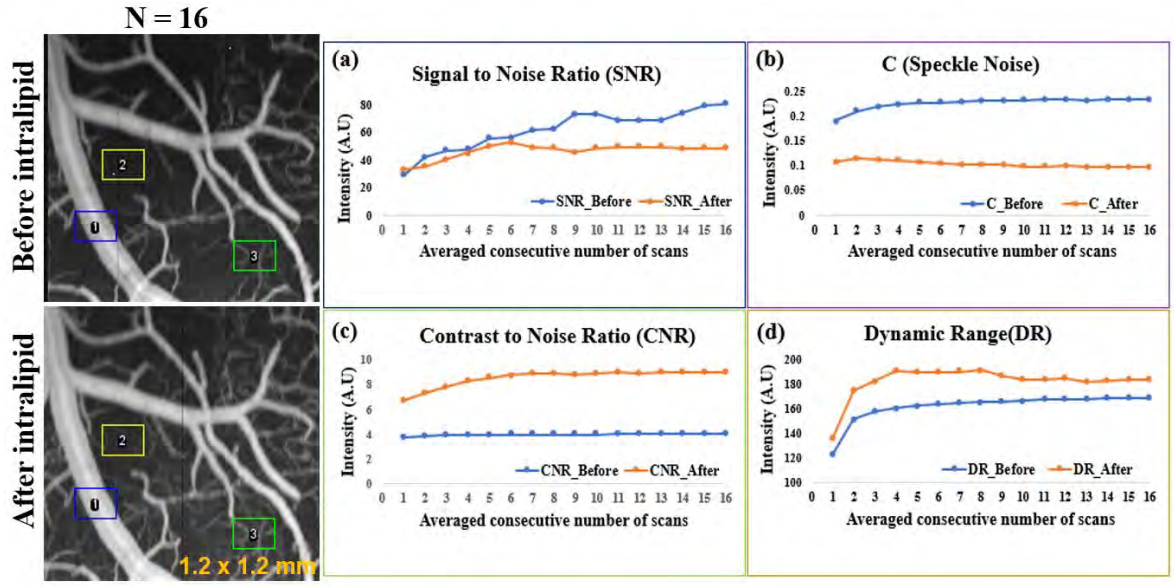

Figure 4-51 The imaging parameters SNR, C, CNR and DR to quantify the enhancement before and after injection of intralipid for the averaged consecutive scans.

The SNR, C, CNR and DR intensity was plotted as a function of a number of averaged consecutive scans to quantify the enhancement before and after injection of intralipid for the 16 averaged consecutive scans shown in Figure 4-51. It was observed that after 9 averaged consecutive scans, the imaging parameters has almost remained constant. This clearly shows that with or without intralipid averaging over 9 consecutive scans would not increase the intensity. The signal to noise ratio is similar for before and after injection of intralipids for up to 8 averaged consecutive scans, but whereas the speckle noise (C) has decreased after injection of intralipid.

Gaussian OCM (1300 nm) mouse brain

The cerebrovascular enhancement in the deeper region of the mouse brain is studied using the Telesto PS-OCM system, centred at 1300 nm. The OCM vascular signal enhancement with intralipids in small vasculature can be quantified efficiently as this system was optimized to achieve a high imaging depth (~2.5 mm) with 4.2 μm axial resolution (in the tissue). The small region of the cerebral region was imaged to capture all the RBC's in the capillary in one circulation time (>15 sec), and only the segmented deeper layer of the brain is analyzed to see the enhancement in small vessels. The FOV of the cerebral imaging is 0.3 × 0.3 mm and the enhancement is easier to visualize in this small FOV along with 1300 nm Gaussian OCM system. The mouse cerebral vasculature with [Figure 4-52(a)] and without [Figure 4-52(b)] intralipids for 6 different ROI regions. The integrated intensity profile in these ROI's as the function along the width of ROI region is plotted for with [Figure 4-52(c)] and without [Figure 4-52(d)] intralipid injection for the deeper regions. There is only ~10-15% increase in the OCM signal intensity before and after injection of intralipid in all the 6 selected ROI's.

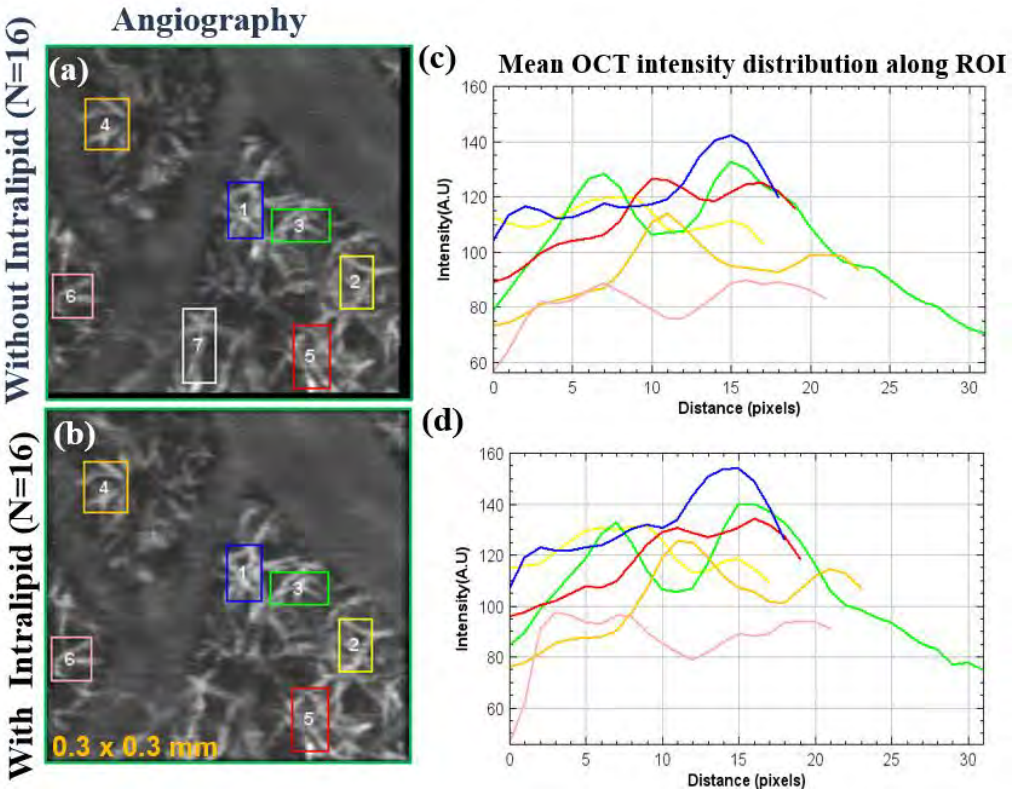

Figure 4-52 The mouse cerebral vasculatureusing 1300 nm Gaussian OCM (a-b) with and without intralipids for 6 different ROI regions respectively and (c-d) the mean OCM intensity profile in the ROI as the function along the width of ROI region plotted for with and without intralipid injection.

These results suggest that even with a 1300 nm OCM system, which gives superior visualization of the microvasculature, the difference with and without intralipids is low (~10-15%).

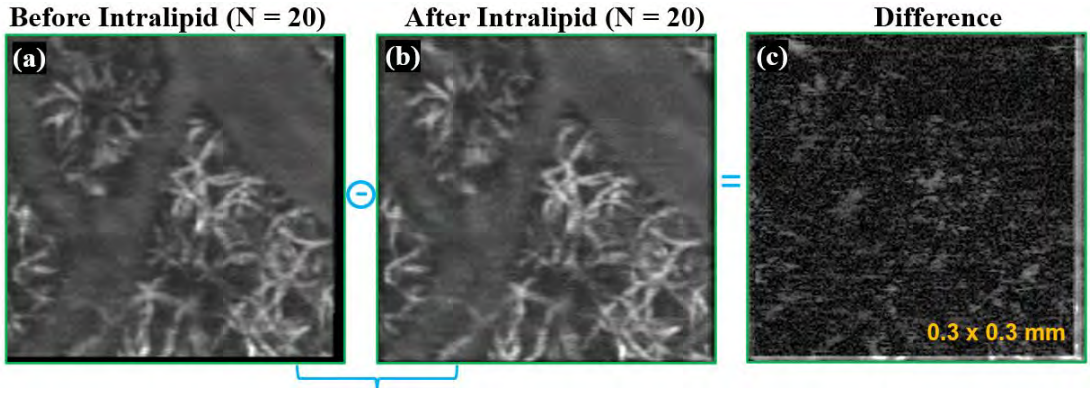

Figure 4-53 The angiography images for 20 consecutive images (N = 20) for (a-b) before and after injection of intralipid and (c) the difference in the enhancement of microvasculature before and after injection of intralipid.

To further confirm the enhancement after injection of intralipid, we subtracted the angiography images for 20 averaged consecutive angiography images before [Figure 4-53(a)] and after [Figure 4-53(b)] injection of the intralipid and the difference in enhancement is shown in Figure 4-53(c) for the deeper microvasculature. The visualization of the enhancement in the

microvasculature, the 20 averaged consecutive images were subtracted for angiography obtained before [Figure 4-53(a)] and after [Figure 4-53(b)] injection of the intralipid and the difference is shown in Figure 4-53(c) for the deeper microvasculature. Both superficial and deeper layers of the mouse brain angiography images for 16 averaged consecutive images (N = 16) obtained with three different ROI's is shown in Figure 4-54.

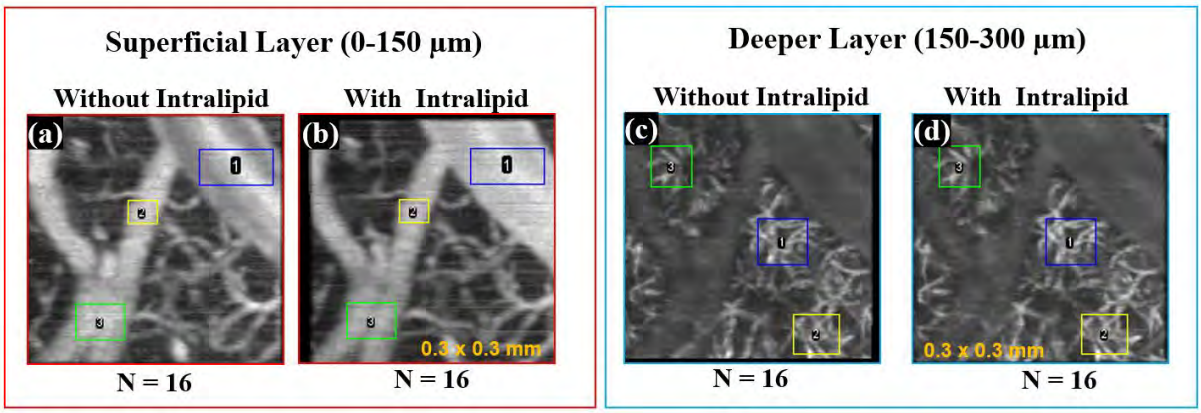

Figure 4-54 The angiography images of the mouse brain of 1300 nm Gaussian OCM for 16 averaged consecutive images (N = 16) for (a-b) without and with intralipid injection for the superficial layers, (c-d) without and with intralipid for the deeper layers.

The three different ROI's chosen for the superficial layers include largest vessel (ROI-1), the medium diameter of large vessel (ROI-2) and vessel at the junction (ROI-3) without [Figure 4-54(a)] and with intralipid injection for the superficial layers is used to estimate the mean of OCM signal in the ROI's. The mean OCM signal intralipids of the three different ROI for 16 number of averaged angiography images for large and small vessels before and after injection of intralipids is shown in Figure 4-55. This graph shows that the OCM signal intensity enhancement of the same number of averaged consecutive images before and after intralipid injection is less than only ~11 %.

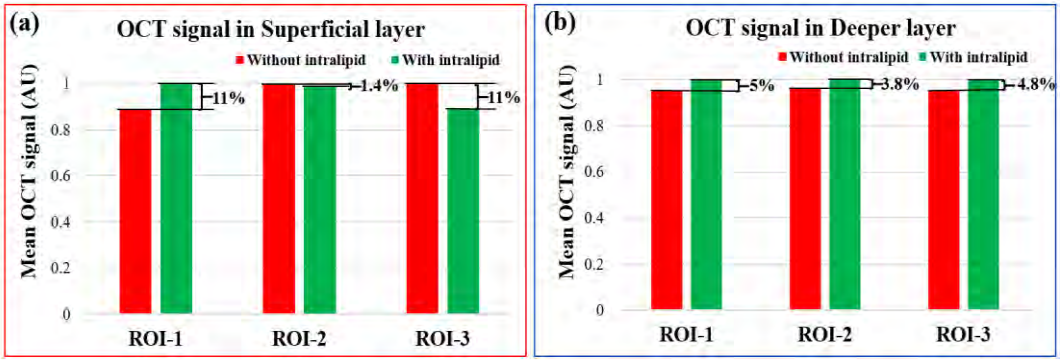

Figure 4-55 The mean OCM signal intralipids of the three different ROI for 16 number of averaged angiography images for (a-b) large and small vessels for before and after injection of intralipids obtained using 1300 nm Gaussian OCM system.

The microvascular enhancement of the superficial layer before [Figure 4-56(a)] and after [Figure 4-56(a)] injection of intralipid was observed, and the difference between them was shown in Figure 4-56(c). Similarly, for the microvascular enhancement of the deeper layer before [Figure 4-56(d)] and after [Figure 4-56(e)] injection of intralipid and the enhancement was seen as the difference between them as shown in Figure 4-56(f). The enhancement after injection of microvasculature for the larger field of view of 2.4 × 2.4 mm for single angiography images before and after injection was shown in Figure 4-56.

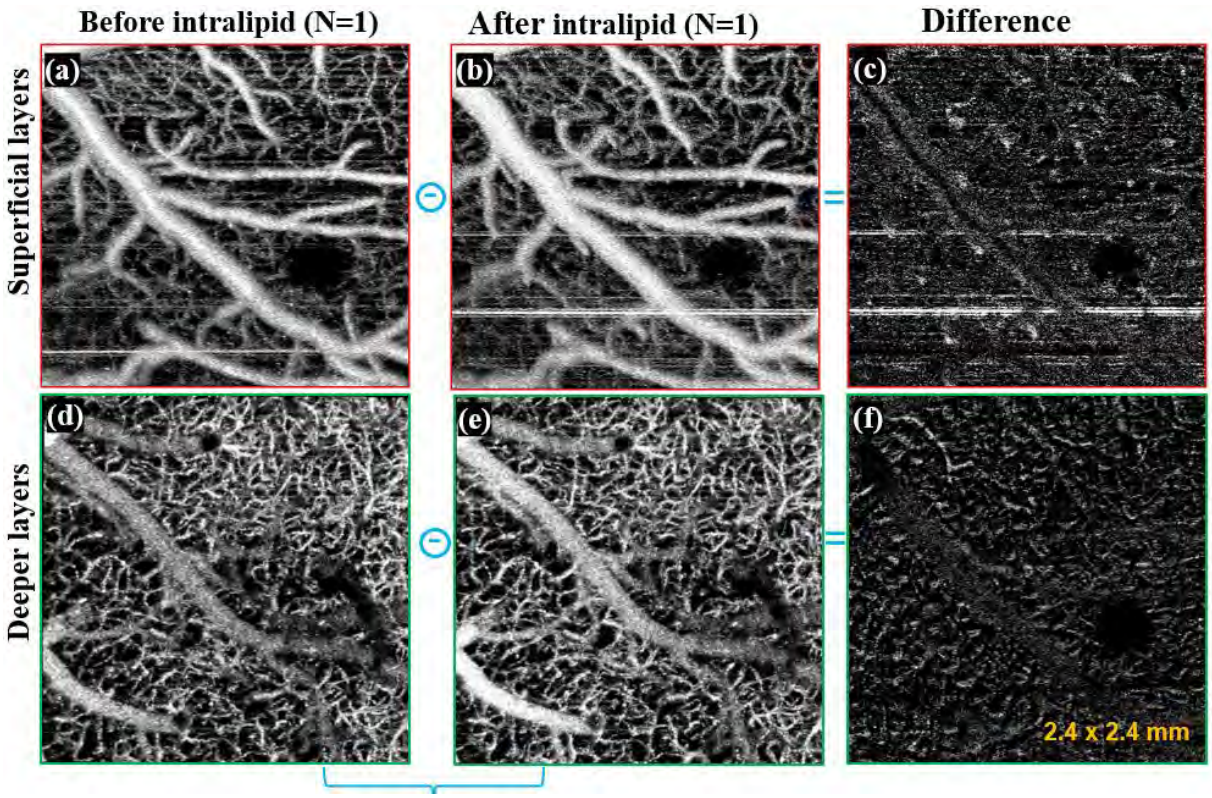

Figure 4-56 The microvascular enhancement for a larger field of view for single angiography images (a-b) superficial layer before and after injection of intralipid, (d-e) deeper layer before and after injection of intralipid, (c,f) difference in the angiography images before and after injection of intralipid for superficial and deeper layers obtained using 1300 nm Gaussian OCM syatem.

There is an enhancement in the microvasculature prominent for both superficial and deeper layers [Figure 4-56(c,f)]. However, only existing vasculature is enhanced, and averaging consecutive angiography images would achieve a similar result as intralipid injection.

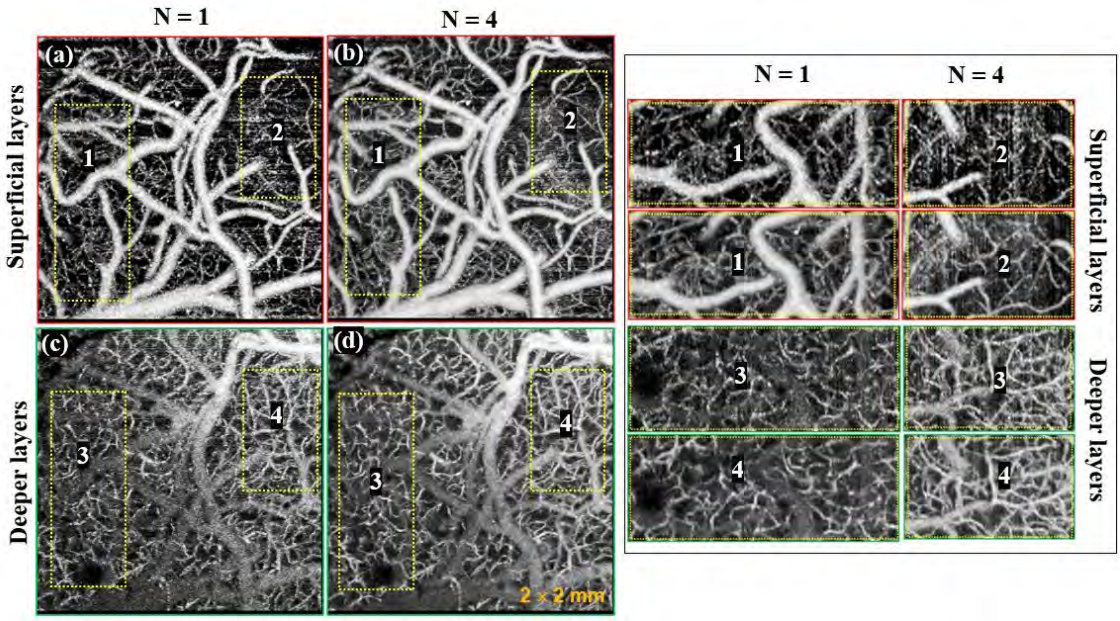

Figure 4-57 The enhancement in the angiography image of (a-b) superficial microvasculature without intralipid for averaged consecutive angiography images N = 1, 4 respectively (c-d) deeper microvasculature for averaged consecutive angiography images N = 1, 4 respectively and the inset image shows their corresponding zoom-in vasculature.

The enhancement in the microvasculature obtained from the 1300 nm OCM-A system as shown in Figure 4-57 between the single angiography image (N = 1) and averaging 4 angiography images (N = 4) the mouse brain. The averaged consecutive angiography images without intralipid for the number of averaged images N = 1, 4 for the segmented superficial microvasculature are shown in Figures 4-57(a-b), and deeper microvasculature is shown in Figure 4-57(c-d). The zoomed-in images represent the selected region to compare the difference in enhancement without and with averaging. The results clearly demostrate that the contrats of the microvasculature was hugely improved with just four number of averaged concescutive images .

The new method was described in Figure 4-45 addressed the problem to improve contrast without external contrast agents, and we provided an alternate method to improve the contrast of OCM without any contrast agents. In this regard, to support and verify our new method, the results in Figure 4-48 shows that the microfluidic channel with blood averaged for 6 consecutive scans (N = 6) and a single scan for blood with intralipid (N = 1) are similar. Figure 4-47 shows that mean OCM signal intensity is increased at different consecutive scans because of the RBC's flow slowly and discontinuously in capillaries. This gives the advantage to achieve the contrast enhancement even with a few averaging consecutive scans compared to intralipid injection. The in-vivo mouse brain was imaged with and without intralipids for the same number of averaged scans, and the resulted difference in enhancement for deeper layers using 1300 nm OCM system

is only 10-15%, as shown in Figure 4.52 and Figure 4-55. We have also verified that averaging only 4 consecutive angiography images (N = 4) would yield improvement OCM signal and microvasculature of the existing vessels in the superficial and deeper layer, as shown in Figure 4-57.

Chapter 5 Conclusions

The optical coherence microscopy (OCM) was chosen as state of the art to achieve a better trade-off between the transverse and depth resolution for in-vivo brain imaging than other imaging modalities.

We have designed and constructed both: Gaussian OCM and Bessel beam OCM systems for the cerebral imaging as described in Section 3.1.1 and Section 3.1.2, respectively. Both systems have been validated for brain vascular imaging in mice by OCM-A method. The comparison of the performance of the Bessel beam illumination over the Gaussian beam for the microvascular visibility was studied using G-OCMA and B-OCMA system in Section 4.3. Although the Bessel beam has a unique advantage because it extended depth of focus, the Bessel beam OCM construction and maintenance complexity makes it less attractive over Gaussian beam OCM. The angiomaps obtained at different segmented depths infers that even though the Bessel beam has a uniform focus for the depth segmented cerebral microvasculature, but still the overall contribution from all the regions is comparable to the angiography results of Gaussian OCMA. However, we do not advice using a trade-off between sensitivity, depth imaging, resolution, but for the longitudinal imaging and applications of biological study, it should be carefully chosen. We have chosen G-OCMA for the rest of the studies as its advantages offer practical, user-friendly, stabilization, repeatability and optimization for the longitudinal in-vivo mice brain imaging studies. Therefore, the Gaussian beam OCM system has proven to be the most preferred for longitudinal studies.

The OCM contrast enhancement using the synthetic scattered LGNRs in in-vivo mouse brain was studied for the first time. The ability of the LGNRs to enhance the infrared scattering using plasmon resonance to enable the OCM-A signal enhancement and their sensitivity for in-vivo brain imaging was demonstrated in Section 4.5. We also discussed the possibility of sensitivity and OCM signal enhancement in both superficial and deeper layers in-vivo brain imaging with dura intact to the skull using the Gaussian OCM-A system at 800 nm and 1300 nm. The results show a considerable enhancement in the vasculature for the superficial layers, but there was very little enhancement in the angiography of the deeper layer of the mouse brain microvasculature. In addition, the other factor that makes LGNRs less attractive is that the preparation of GNRs is difficult and time-consuming. The synthesized GNRs were aggregated after a few weeks to months, making it difficult for longitudinal imaging studies of diseased models. Even though the LGNRs are coated with polymer to reduce the toxicity, they would adversely affect the animal for longitudinal imaging studies. In our experiments the use of

LGNRs in brain imaging gave disappointing results due to the accumulation of nanorods in the blood vessels of the brain, resulting in stroke. All the addressed challenges and little contrast enhancement conclude that LGNRs are not a potential candidate as contrast agents, especially for in-vivo brain imaging studies.

The introduction of nontoxic scattering contrast agent intralipid to enhance the OCM-A contrast for in-vivo brain tissue imaging was demonstrated in Section 4.5.4. The OCM signal enhancement, especially in the deeper microvasculature of the brain tissue using 800 nm and 1300 nm Gaussian OCM system, was studied. We also evaluated the contrast enhancement with a 1300 SD-OCM system with high axial and transverse resolution. The application of intralipids for the brain imaging and the results shows OCM signal enhancement in both the superficial vasculature and deeper vasculature. Nevertheless, the improvement in the angio signal of the deeper microvasculature is only 10-15% and may be not sufficient for the quantification of diseased progression. Moreover, the study showed that even with a 1700 nm Gaussian OCM system, there was not a huge enhancement in the deeper microvasculature of the in-vivo mouse brain [88].

We realized that the mean OCM signal intensity corresponding to light backscattered from capillaries is increased by consecutive averaging scans (minimum N = 4) because RBC's flow discontinuously in small vessels. Therefore, an averaging would capture all the RBCs and improve the contrast. This gives the advantage to achieve the contrast enhancement even with a few averaging consecutive scans compared to intralipid injection. The results demonstrate that averaging method improved the OCM signal contrast without the use of any contrast agents. For the first time, we have quantified and evaluated the potential enhancement without intralipids using our simple averaging approach in the in-vivo mouse brain for the deeper layers of the mouse brain. The enhancement of cerebrovascular imaging for GBM tumor in the brain would provide an insight to see the possibility of the growth of the tumor and to understand the physiological, biological process of angiogenesis. The enhanced contrast without intralipids can be used to detect molecules or various biological entities better to understand biological processes or enhanced detection capability for diseases. This proposed method without contrast agents will also help enhance the OCM signal and visualize small tumor microvasculature, functional brain imaging early detection of neo-angiogenesis. The advantage of this method provides an insight in interpreting the natural biological process during biological events for growth processes like tumor, stroke and other diseased models without contrast agents and avoid serious complications in the small animal for longitudinal imaging.

We also found that post-processing methods had a positive effect and improved imaging quality. The critical hardware modules, alignment and maintenance required for the OCM setup were synchronized and characterized using LABVIEW software as described in Section 3.1.5 and Section 3.1.6. The software for acquisition of the OCM data, angio processing and data visualization are described in Section 3.1.7 - Section 3.1.9. The scanning protocols and post-processing methods described in Section 3.2 and Section 3.3 respectively enabled the high quality enhanced angiography to quantify the microvasculature for the disease progression. The animal handling procedure and guidelines are followed for the preparation of mice and rat for the experiments as described in Section 3.4. We also found that deep animal anesthesia and post-processing methods had a positive effect and improved imaging quality.

The potential and technical capability of the both OCM and OCM-A as a powertool for brain imaging was demonstrated. The system was tested for in-vivo longitudinal studies of Glioblastoma tumor development and progression in mouse brain as presented in Section 4.4. The process of neovascularization, an important feature of GBM, was observed for the first time using OCM-A. The imaging of mouse cortical vascular networks and tumour development was studied for up to 2 weeks. The new methodologies and biomarkers were developed to evaluate the tumour progression using fractal analysis as the first step towards quantitative monitoring of glioma.

The future plan is to use the G-OCMA system compatible for longitudinal pharmaceutical drug monitoring and treatment of the GBM tumour. The efficiency of the drug could be tested using the current method in a span of few weeks to months.

References

[1] S. Ackerman, Discovering the brain, (1992).
[2] C. Iadecola, Neurovascular regulation in the normal brain and in Alzheimer's disease, Nature Reviews Neuroscience 5(5) (2004) 347-360.
[3] D. Attwell, A.M. Buchan, S. Charpak, M. Lauritzen, B.A. MacVicar, E.A. Newman, Glial and neuronal control of brain blood flow, Nature 468(7321) (2010) 232-243.
[4] S. Hirsch, J. Reichold, M. Schneider, G. Székely, B. Weber, Topology and hemodynamics of the cortical cerebrovascular system, Journal of Cerebral Blood Flow & Metabolism 32(6) (2012) 952-967.
[5] S.C. Patel, S. Wagner, G. Cooper, R.L. Rodnitzky, The vasculature of the human brain, Neuroscience in Medicine, Springer2003, pp. 129-163.
[6] L.N. Sekhar, A. Chanda, A. Morita, The preservation and reconstruction of cerebral veins and sinuses, Journal of clinical neuroscience 9(4) (2002) 391-399.
[7] P. Blinder, A.Y. Shih, C. Rafie, D. Kleinfeld, Topological basis for the robust distribution of blood to rodent neocortex, Proceedings of the National Academy of Sciences 107(28) (2010) 12670-12675.
[8] J.H. Zhang, J. Badaut, J. Tang, A. Obenaus, R. Hartman, W.J. Pearce, The vascular neural network—a new paradigm in stroke pathophysiology, Nature Reviews Neurology 8(12) (2012) 711-716.
[9] P. Mergenthaler, A. Meisel, Do stroke models model stroke?, Disease models & mechanisms 5(6) (2012) 718-725.

[10] G.J. Goldey, D.K. Roumis, L.L. Glickfeld, A.M. Kerlin, R.C. Reid, V. Bonin, D.P. Schafer, M.L. Andermann, Removable cranial windows for long-term imaging in awake mice, Nature protocols 9(11) (2014) 2515.
[11] C. Heo, H. Park, Y.-T. Kim, E. Baeg, Y.H. Kim, S.-G. Kim, M. Suh, A soft, transparent, freely accessible cranial window for chronic imaging and electrophysiology, Scientific reports 6(1) (2016) 1-11.
[12] S. Augustinaite, B. Kuhn, Chronic Cranial Window for Imaging Cortical Activity in Head-Fixed Mice, STAR protocols 1(3) (2020) 100194.
[13] A. Holtmaat, T. Bonhoeffer, D.K. Chow, J. Chuckowree, V. De Paola, S.B. Hofer, M. Hübener, T. Keck, G. Knott, W.-C.A. Lee, Long-term, high-resolution imaging in the mouse neocortex through a chronic cranial window, Nature protocols 4(8) (2009) 1128.
[14] S.H. Ramirez, S. Fan, M. Zhang, A. Papugani, N. Reichenbach, H. Dykstra, A.J. Mercer, R.F. Tuma, Y. Persidsky, Inhibition of glycogen synthase kinase 3β (GSK3β) decreases inflammatory responses in brain endothelial cells, The American journal of pathology 176(2) (2010) 881-892.
[15] S.H. Ramirez, J. Haskó, A. Skuba, S. Fan, H. Dykstra, R. McCormick, N. Reichenbach, I. Krizbai, A. Mahadevan, M. Zhang, Activation of cannabinoid receptor 2 attenuates leukocyte–endothelial cell interactions and blood–brain barrier dysfunction under inflammatory conditions, Journal of Neuroscience 32(12) (2012) 4004-4016.
[16] Q.Q. Zhang, X.J. Wu, T. Tang, S.W. Zhu, Q. Yao, B.Z. Gao, X.C. Yuan, Quantitative analysis of rectal cancer by spectral domain optical coherence tomography, Phys Med Biol 57(16) (2012) 5235-44.
[17] H. Dolezyczek, M. Rapolu, P. Niedzwiedziuk, K. Karnowski, D. Borycki, J. Dzwonek, G. Wilczynski, M. Malinowska, M. Wojtkowski, Longitudinal in-vivo OCM imaging of glioblastoma development in the mouse brain, Biomedical Optics Express 11(9) (2020) 5003-5016.
[18] H. Dolezyczek, S. Tamborski, P. Majka, D.M. Sampson, M. Wojtkowski, G. Wilczynski, M. Szkulmowski, M. Malinowska, In vivo brain imaging with multimodal optical coherence microscopy in a mouse model of thromboembolic photochemical stroke, Neurophotonics 7(1) (2020) 015002.
[19] P. Shin, W. Choi, J. Joo, W.-Y. Oh, Quantitative hemodynamic analysis of cerebral blood flow and neurovascular coupling using optical coherence tomography angiography, Journal of Cerebral Blood Flow & Metabolism 39(10) (2019) 1983-1994.
[20] R. Mostany, C. Portera-Cailliau, A craniotomy surgery procedure for chronic brain imaging, Journal of visualized experiments: JoVE (12) (2008).
[21] V. Zuluaga-Ramirez, S. Rom, Y. Persidsky, Craniula: A cranial window technique for prolonged imaging of brain surface vasculature with simultaneous adjacent intracerebral injection, Fluids and Barriers of the CNS 12(1) (2015) 24.
[22] M.L. Andermann, A.M. Kerlin, C. Reid, Chronic cellular imaging of mouse visual cortex during operant behavior and passive viewing, Frontiers in cellular neuroscience 4 (2010) 3.
[23] C.J. Roome, B. Kuhn, Chronic cranial window with access port for repeated cellular manipulations, drug application, and electrophysiology, Frontiers in cellular neuroscience 8 (2014) 379.
[24] K. Kılıç, M. Desjardins, J. Tang, M. Thunemann, S. Sunil, S.E. Erdener, D.D. Postnov, D.A. Boas, A. Devor, Chronic Cranial Windows for Long Term Multimodal Brain Imaging in Mice, Frontiers in physiology 11 (2020) 1813.
[25] G. Silasi, D. Xiao, M.P. Vanni, A.C. Chen, T.H. Murphy, Intact skull chronic windows for mesoscopic wide-field imaging in awake mice, Journal of neuroscience methods 267 (2016) 141-149.
[26] D.A. Orringer, T. Chen, D.-L. Huang, W.M. Armstead, B.A. Hoff, Y.-E.L. Koo, R.F. Keep, M.A. Philbert, R. Kopelman, O. Sagher, The brain tumor window model: a combined cranial window and implanted glioma model for evaluating intraoperative contrast agents, Neurosurgery 66(4) (2010) 736-743.
[27] G. Hong, S. Diao, J. Chang, A.L. Antaris, C. Chen, B. Zhang, S. Zhao, D.N. Atochin, P.L. Huang, K.I. Andreasson, Through-skull fluorescence imaging of the brain in a new near-infrared window, Nature photonics 8(9) (2014) 723-730.
[28] H. Park, N. You, J. Lee, M. Suh, Longitudinal study of hemodynamics and dendritic membrane potential changes in the mouse cortex following a soft cranial window installation, Neurophotonics 6(1) (2019) 015006.
[29] A.Y. Shih, J.D. Driscoll, P.J. Drew, N. Nishimura, C.B. Schaffer, D. Kleinfeld, Two-photon microscopy as a tool to study blood flow and neurovascular coupling in the rodent brain, Journal of Cerebral Blood Flow & Metabolism 32(7) (2012) 1277-1309.
[30] D. Dombeck, D. Tank, Two-photon imaging of neural activity in awake mobile mice, Cold Spring Harbor Protocols 2014(7) (2014) pdb. top081810.
[31] F. Helmchen, W. Denk, Deep tissue two-photon microscopy, Nature methods 2(12) (2005) 932-940.
[32] K. Svoboda, R. Yasuda, Principles of two-photon excitation microscopy and its applications to neuroscience, Neuron 50(6) (2006) 823-839.
[33] R. Mostany, C. Portera-Cailliau, A method for 2-photon imaging of blood flow in the neocortex through a cranial window, J Vis Exp 12 (2008).

[34] M. Desjardins, K. Kılıç, M. Thunemann, C. Mateo, D. Holland, C.G. Ferri, J.A. Cremonesi, B. Li, Q. Cheng, K.L. Weldy, Awake mouse imaging: from two-photon microscopy to blood oxygen level–dependent functional magnetic resonance imaging, Biological Psychiatry: Cognitive Neuroscience and Neuroimaging 4(6) (2019) 533-542.
[35] O. Garaschuk, R.-I. Milos, A. Konnerth, Targeted bulk-loading of fluorescent indicators for two-photon brain imaging in vivo, Nature protocols 1(1) (2006) 380.
[36] C.H.T. Tran, G.R. Gordon, Acute two-photon imaging of the neurovascular unit in the cortex of active mice, Frontiers in cellular neuroscience 9 (2015) 11.
[37] T.P. Santisakultarm, C.J. Kersbergen, D.K. Bandy, D.C. Ide, S.-H. Choi, A.C. Silva, Two-photon imaging of cerebral hemodynamics and neural activity in awake and anesthetized marmosets, Journal of neuroscience methods 271 (2016) 55-64.
[38] M. Isshiki, S. Okabe, Evaluation of cranial window types for in vivo two-photon imaging of brain microstructures, Microscopy 63(1) (2014) 53-63.
[39] M.M. Koletar, A. Dorr, M.E. Brown, J. McLaurin, B. Stefanovic, Refinement of a chronic cranial window implant in the rat for longitudinal in vivo two–photon fluorescence microscopy of neurovascular function, Scientific reports 9(1) (2019) 1-12.
[40] T. Wang, D.G. Ouzounov, C. Wu, N.G. Horton, B. Zhang, C.-H. Wu, Y. Zhang, M.J. Schnitzer, C. Xu, Three-photon imaging of mouse brain structure and function through the intact skull, Nature methods 15(10) (2018) 789-792.
[41] T. Wang, C. Xu, Three-photon neuronal imaging in deep mouse brain, Optica 7(8) (2020) 947-960.
[42] R.P. Barretto, M.J. Schnitzer, In vivo optical microendoscopy for imaging cells lying deep within live tissue, Cold Spring Harbor Protocols 2012(10) (2012) pdb. top071464.
[43] K. Takasaki, R. Abbasi-Asl, J. Waters, Superficial bound of the depth limit of Two-Photon imaging in mouse brain, Eneuro 7(1) (2020).
[44] P. Theer, W. Denk, On the fundamental imaging-depth limit in two-photon microscopy, JOSA A 23(12) (2006) 3139-3149.
[45] N.G. Horton, K. Wang, D. Kobat, C.G. Clark, F.W. Wise, C.B. Schaffer, C. Xu, In vivo three-photon microscopy of subcortical structures within an intact mouse brain, Nature photonics 7(3) (2013) 205-209.
[46] D.G. Ouzounov, T. Wang, M. Wang, D.D. Feng, N.G. Horton, J.C. Cruz-Hernández, Y.-T. Cheng, J. Reimer, A.S. Tolias, N. Nishimura, In vivo three-photon imaging of activity of GCaMP6-labeled neurons deep in intact mouse brain, Nature methods 14(4) (2017) 388-390.
[47] N. Davoodzadeh, M.S. Cano-Velázquez, D.L. Halaney, C.R. Jonak, D.K. Binder, G. Aguilar, Evaluation of a transparent cranial implant as a permanent window for cerebral blood flow imaging, Biomedical optics express 9(10) (2018) 4879-4892.
[48] L. Ghanbari, R.E. Carter, M.L. Rynes, J. Dominguez, G. Chen, A. Naik, J. Hu, M.A.K. Sagar, L. Haltom, N. Mossazghi, Cortex-wide neural interfacing via transparent polymer skulls, Nature communications 10(1) (2019) 1-13.
[49] V. De Paola, A. Holtmaat, G. Knott, S. Song, L. Wilbrecht, P. Caroni, K. Svoboda, Cell type-specific structural plasticity of axonal branches and boutons in the adult neocortex, Neuron 49(6) (2006) 861-875.
[50] J.T. Trachtenberg, B.E. Chen, G.W. Knott, G. Feng, J.R. Sanes, E. Welker, K. Svoboda, Long-term in vivo imaging of experience-dependent synaptic plasticity in adult cortex, Nature 420(6917) (2002) 788-794.
[51] J.S. Schuman, M.R. Hee, A.V. Arya, T. Pedut-Kloizman, C.A. Puliafito, J.G. Fujimoto, E.A. Swanson, Optical coherence tomography: A new tool for glaucoma diagnosis, Current Opinion in Ophthalmology 6(2) (1995) 89-95.
[52] U. Baran, R.K. Wang, Review of optical coherence tomography based angiography in neuroscience, Neurophotonics 3(1) (2016) 010902.
[53] A. Wylęgała, Principles of OCTA and Applications in Clinical Neurology, Current neurology and neuroscience reports 18(12) (2018) 96.
[54] J.F. De Boer, R. Leitgeb, M. Wojtkowski, Twenty-five years of optical coherence tomography: the paradigm shift in sensitivity and speed provided by Fourier domain OCT, Biomedical optics express 8(7) (2017) 3248-3280.
[55] B. Laviña, Brain vascular imaging techniques, International journal of molecular sciences 18(1) (2017) 70.
[56] M.S. Mahmud, D.W. Cadotte, B. Vuong, C. Sun, T.W. Luk, A. Mariampillai, V.X. Yang, Review of speckle and phase variance optical coherence tomography to visualize microvascular networks, Journal of biomedical optics 18(5) (2013) 050901.
[57] S. Boppart, M. Brezinski, G. Tearney, B. Bouma, J. Fujimoto, Imaging organogenesis with optical coherence tomography, FASEB Journal 10(3) (1996) A825.
[58] S.A. Boppart, B.E. Bouma, M.E. Brezinski, G.J. Tearney, J.G. Fujimoto, Imaging developing neural morphology using optical coherence tomography, Journal of Neuroscience Methods 70(1) (1996) 65-72.
[59] O. Liba, M.D. Lew, E.D. SoRelle, R. Dutta, D. Sen, D.M. Moshfeghi, S. Chu, A. de La Zerda, Speckle-modulating optical coherence tomography in living mice and humans, Nature communications 8(1) (2017) 1-13.

[60] C. Leahy, H. Radhakrishnan, V.J. Srinivasan, Volumetric imaging and quantification of cytoarchitecture and myeloarchitecture with intrinsic scattering contrast, Biomedical optics express 4(10) (2013) 1978-1990.
[61] V.J. Srinivasan, H. Radhakrishnan, J.Y. Jiang, S. Barry, A.E. Cable, Optical coherence microscopy for deep tissue imaging of the cerebral cortex with intrinsic contrast, Optics express 20(3) (2012) 2220-2239.
[62] S. Tamborski, H.C. Lyu, H. Dolezyczek, M. Malinowska, G. Wilczynski, D. Szlag, T. Lasser, M. Wojtkowski, M. Szkulmowski, Extended-focus optical coherence microscopy for high-resolution imaging of the murine brain, Biomedical optics express 7(11) (2016) 4400-4414.
[63] U. Baran, Y. Li, R.K. Wang, Vasodynamics of pial and penetrating arterioles in relation to arteriolo-arteriolar anastomosis after focal stroke, Neurophotonics 2(2) (2015) 025006.
[64] Z. Yaqoob, J. Wu, C. Yang, Spectral domain optical coherence tomography: a better OCT imaging strategy, Biotechniques 39(6) (2005) S6-S13.
[65] J. Binding, J.B. Arous, J.-F. Léger, S. Gigan, C. Boccara, L. Bourdieu, Brain refractive index measured in vivo with high-NA defocus-corrected full-field OCT and consequences for two-photon microscopy, Optics express 19(6) (2011) 4833-4847.
[66] O. Assayag, K. Grieve, B. Devaux, F. Harms, J. Pallud, F. Chretien, C. Boccara, P. Varlet, Imaging of non-tumorous and tumorous human brain tissues with full-field optical coherence tomography, NeuroImage: clinical 2 (2013) 549-557.
[67] A. Giese, H. Böhringer, J. Leppert, S. Kantelhardt, E. Lankenau, P. Koch, R. Birngruber, G. Hüttmann, Non-invasive intraoperative optical coherence tomography of the resection cavity during surgery of intrinsic brain tumors, Photonic Therapeutics and Diagnostics II, International Society for Optics and Photonics, 2006, p. 60782Z.
[68] H. Böhringer, E. Lankenau, F. Stellmacher, E. Reusche, G. Hüttmann, A. Giese, Imaging of human brain tumor tissue by near-infrared laser coherence tomography, Acta neurochirurgica 151(5) (2009) 507-517.
[69] C. Kut, K.L. Chaichana, J. Xi, S.M. Raza, X. Ye, E.R. McVeigh, F.J. Rodriguez, A. Quiñones-Hinojosa, X. Li, Detection of human brain cancer infiltration ex vivo and in vivo using quantitative optical coherence tomography, Science translational medicine 7(292) (2015) 292ra100-292ra100.
[70] W. Yuan, C. Kut, W. Liang, X. Li, Robust and fast characterization of OCT-based optical attenuation using a novel frequency-domain algorithm for brain cancer detection, Scientific reports 7(1) (2017) 1-8.
[71] H. Böhringer, D. Boller, J. Leppert, U. Knopp, E. Lankenau, E. Reusche, G. Hüttmann, A. Giese, Time-domain and spectral-domain optical coherence tomography in the analysis of brain tumor tissue, Lasers in Surgery and Medicine: The Official Journal of the American Society for Laser Medicine and Surgery 38(6) (2006) 588-597.
[72] C. Magnain, J.C. Augustinack, M. Reuter, C. Wachinger, M.P. Frosch, T. Ragan, T. Akkin, V.J. Wedeen, D.A. Boas, B. Fischl, Blockface histology with optical coherence tomography: a comparison with Nissl staining, NeuroImage 84 (2014) 524-533.
[73] H. Wang, C. Lenglet, T. Akkin, Structure tensor analysis of serial optical coherence scanner images for mapping fiber orientations and tractography in the brain, Journal of biomedical optics 20(3) (2015) 036003.
[74] E. Min, J. Lee, A. Vavilin, S. Jung, S. Shin, J. Kim, W. Jung, Wide-field optical coherence microscopy of the mouse brain slice, Optics letters 40(19) (2015) 4420-4423.
[75] J. Lefebvre, A. Castonguay, P. Pouliot, M. Descoteaux, F. Lesage, Whole mouse brain imaging using optical coherence tomography: reconstruction, normalization, segmentation, and comparison with diffusion MRI, Neurophotonics 4(4) (2017) 041501.
[76] H. Wang, C. Magnain, S. Sakadžić, B. Fischl, D.A. Boas, Characterizing the optical properties of human brain tissue with high numerical aperture optical coherence tomography, Biomedical optics express 8(12) (2017) 5617-5636.
[77] H. Wang, C. Magnain, R. Wang, J. Dubb, A. Varjabedian, L.S. Tirrell, A. Stevens, J.C. Augustinack, E. Konukoglu, I. Aganj, as-PSOCT: Volumetric microscopic imaging of human brain architecture and connectivity, NeuroImage 165 (2018) 56-68.
[78] W. Choi, K.J. Mohler, B. Potsaid, C.D. Lu, J.J. Liu, V. Jayaraman, A.E. Cable, J.S. Duker, R. Huber, J.G. Fujimoto, Choriocapillaris and choroidal microvasculature imaging with ultrahigh speed OCT angiography, PloS one 8(12) (2013) e81499.
[79] Y. Jia, E. Wei, X. Wang, X. Zhang, J.C. Morrison, M. Parikh, L.H. Lombardi, D.M. Gattey, R.L. Armour, B. Edmunds, Optical coherence tomography angiography of optic disc perfusion in glaucoma, Ophthalmology 121(7) (2014) 1322-1332.
[80] A. Ishibazawa, T. Nagaoka, A. Takahashi, T. Omae, T. Tani, K. Sogawa, H. Yokota, A. Yoshida, Optical coherence tomography angiography in diabetic retinopathy: a prospective pilot study, American journal of ophthalmology 160(1) (2015) 35-44. e1.
[81] R.F. Spaide, Optical coherence tomography angiography signs of vascular abnormalization with antiangiogenic therapy for choroidal neovascularization, American journal of ophthalmology 160(1) (2015) 6-16.

[82] D.Y. Kim, J. Fingler, R.J. Zawadzki, S.S. Park, L.S. Morse, D.M. Schwartz, S.E. Fraser, J.S. Werner, Optical imaging of the chorioretinal vasculature in the living human eye, Proceedings of the National Academy of Sciences 110(35) (2013) 14354-14359.
[83] E. Talisa, M.A. Bonini Filho, A.T. Chin, M. Adhi, D. Ferrara, C.R. Baumal, A.J. Witkin, E. Reichel, J.S. Duker, N.K. Waheed, Spectral-domain optical coherence tomography angiography of choroidal neovascularization, Ophthalmology 122(6) (2015) 1228-1238.
[84] I. Gorczynska, J.V. Migacz, R.J. Zawadzki, A.G. Capps, J.S. Werner, Comparison of amplitude-decorrelation, speckle-variance and phase-variance OCT angiography methods for imaging the human retina and choroid, Biomedical optics express 7(3) (2016) 911-942.
[85] K. Karnowski, A. Ajduk, B. Wieloch, S. Tamborski, K. Krawiec, M. Wojtkowski, M. Szkulmowski, Optical coherence microscopy as a novel, non-invasive method for the 4D live imaging of early mammalian embryos, Scientific reports 7(1) (2017) 1-12.
[86] S. Wang, M. Singh, A.L. Lopez, C. Wu, R. Raghunathan, A. Schill, J. Li, K.V. Larin, I.V. Larina, Direct four-dimensional structural and functional imaging of cardiovascular dynamics in mouse embryos with 1.5 MHz optical coherence tomography, Optics letters 40(20) (2015) 4791-4794.
[87] I.V. Larina, K.V. Larin, M.J. Justice, M.E. Dickinson, Optical Coherence Tomography for live imaging of mammalian development, Current opinion in genetics & development 21(5) (2011) 579-584.
[88] K.S. Park, J.G. Shin, M.M. Qureshi, E. Chung, T.J. Eom, Deep brain optical coherence tomography angiography in mice: in vivo, noninvasive imaging of hippocampal formation, Scientific reports 8(1) (2018) 11614.
[89] T.-H. Tsai, C.L. Leggett, A.J. Trindade, A. Sethi, A.-F. Swager, V. Joshi, J.J. Bergman, H. Mashimo, N.S. Nishioka, E. Namati, Optical coherence tomography in gastroenterology: a review and future outlook, Journal of biomedical optics 22(12) (2017) 121716.
[90] T.-H. Tsai, H.-C. Lee, O.O. Ahsen, K. Liang, M.G. Giacomelli, B.M. Potsaid, Y.K. Tao, V. Jayaraman, M. Figueiredo, Q. Huang, Ultrahigh speed endoscopic optical coherence tomography for gastroenterology, Biomedical optics express 5(12) (2014) 4387-4404.
[91] H.-C. Lee, O.O. Ahsen, K. Liang, Z. Wang, C. Cleveland, L. Booth, B. Potsaid, V. Jayaraman, A.E. Cable, H. Mashimo, Circumferential optical coherence tomography angiography imaging of the swine esophagus using a micromotor balloon catheter, Biomedical optics express 7(8) (2016) 2927-2942.
[92] C.A. Molina, J.L. Saver, Extending reperfusion therapy for acute ischemic stroke: emerging pharmacological, mechanical, and imaging strategies, Stroke 36(10) (2005) 2311-2320.
[93] V.J. Srinivasan, J.Y. Jiang, M.A. Yaseen, H. Radhakrishnan, W. Wu, S. Barry, A.E. Cable, D.A. Boas, Rapid volumetric angiography of cortical microvasculature with optical coherence tomography, Optics letters 35(1) (2010) 43-45.
[94] P.J. Marchand, D. Szlag, J. Extermann, A. Bouwens, D. Nguyen, M. Rudin, T. Lasser, Imaging of cortical structures and microvasculature using extended-focus optical coherence tomography at 1.3 μm, Optics letters 43(8) (2018) 1782-1785.
[95] V.J. Srinivasan, D.N. Atochin, H. Radhakrishnan, J.Y. Jiang, S. Ruvinskaya, W. Wu, S. Barry, A.E. Cable, C. Ayata, P.L. Huang, Optical coherence tomography for the quantitative study of cerebrovascular physiology, Journal of Cerebral Blood Flow & Metabolism 31(6) (2011) 1339-1345.
[96] K.S. Yashin, E.B. Kiseleva, E.V. Gubarkova, A.A. Moiseev, S.S. Kuznetsov, P.A. Shilyagin, G.V. Gelikonov, I.A. Medyanik, L.Y. Kravets, A.A. Potapov, Cross-polarization optical coherence tomography for brain tumor imaging, Frontiers in oncology 9 (2019) 201.
[97] D. Yecies, O. Liba, E.D. SoRelle, R. Dutta, E. Yuan, H. Vogel, G.A. Grant, A. de la Zerda, Speckle modulation enables high-resolution wide-field human brain tumor margin detection and in vivo murine neuroimaging, Scientific reports 9(1) (2019) 1-9.
[98] B.J. Vakoc, R.M. Lanning, J.A. Tyrrell, T.P. Padera, L.A. Bartlett, T. Stylianopoulos, L.L. Munn, G.J. Tearney, D. Fukumura, R.K. Jain, B.E. Bouma, Three-dimensional microscopy of the tumor microenvironment in vivo using optical frequency domain imaging, Nat Med 15(10) (2009) 1219-23.
[99] Y. Jung, Z. Zhi, R.K. Wang, Three-dimensional optical imaging of microvascular networks within intact lymph node in vivo, Journal of biomedical optics 15(5) (2010) 050501.
[100] R.K. Wang, S.L. Jacques, Z. Ma, S. Hurst, S.R. Hanson, A. Gruber, Three dimensional optical angiography, Optics express 15(7) (2007) 4083-4097.
[101] R.K. Wang, S. Hurst, Mapping of cerebro-vascular blood perfusion in mice with skin and skull intact by Optical Micro-AngioGraphy at 1.3 μm wavelength, Optics express 15(18) (2007) 11402-11412.
[102] R.K. Wang, Optical microangiography: a label-free 3-D imaging technology to visualize and quantify blood circulations within tissue beds in vivo, IEEE Journal of Selected Topics in Quantum Electronics 16(3) (2009) 545-554.
[103] J. Zhu, C.W. Merkle, M.T. Bernucci, S.P. Chong, V.J. Srinivasan, Can OCT angiography be made a quantitative blood measurement tool?, Applied Sciences 7(7) (2017) 687.

[104] W. Choi, E.M. Moult, N.K. Waheed, M. Adhi, B. Lee, C.D. Lu, E. Talisa, V. Jayaraman, P.J. Rosenfeld, J.S. Duker, Ultrahigh-speed, swept-source optical coherence tomography angiography in nonexudative age-related macular degeneration with geographic atrophy, Ophthalmology 122(12) (2015) 2532-2544.
[105] Y. Wang, R. Wang, Autocorrelation optical coherence tomography for mapping transverse particle-flow velocity, Optics letters 35(21) (2010) 3538-3540.
[106] V.J. Srinivasan, H. Radhakrishnan, E.H. Lo, E.T. Mandeville, J.Y. Jiang, S. Barry, A.E. Cable, OCT methods for capillary velocimetry, Biomedical optics express 3(3) (2012) 612-629.
[107] B.J. Vakoc, R.M. Lanning, J.A. Tyrrell, T.P. Padera, L.A. Bartlett, T. Stylianopoulos, L.L. Munn, G.J. Tearney, D. Fukumura, R.K. Jain, Three-dimensional microscopy of the tumor microenvironment in vivo using optical frequency domain imaging, Nature medicine 15(10) (2009) 1219-1223.
[108] R.K. Wang, Q. Zhang, Y. Li, S. Song, Optical coherence tomography angiography-based capillary velocimetry, J Biomed Opt 22(6) (2017) 66008.
[109] V.J. Srinivasan, H. Radhakrishnan, Optical Coherence Tomography angiography reveals laminar microvascular hemodynamics in the rat somatosensory cortex during activation, NeuroImage 102 (2014) 393-406.
[110] J.B. Arous, J. Binding, J.-F. Léger, M. Casado, P. Topilko, L. Bourdieu, S. Gigan, A.C. Boccara, Single myelin fiber imaging in living rodents without labeling by deep optical coherence microscopy, Journal of biomedical optics 16(11) (2011) 116012.
[111] F. Li, Y. Song, A. Dryer, W. Cogguillo, Y. Berdichevsky, C. Zhou, Nondestructive evaluation of progressive neuronal changes in organotypic rat hippocampal slice cultures using ultrahigh-resolution optical coherence microscopy, Neurophotonics 1(2) (2014) 025002.
[112] C. Magnain, J.C. Augustinack, E. Konukoglu, M.P. Frosch, S. Sakadžić, A. Varjabedian, N. Garcia, V.J. Wedeen, D.A. Boas, B. Fischl, Optical coherence tomography visualizes neurons in human entorhinal cortex, Neurophotonics 2(1) (2015) 015004.
[113] H. Wang, T. Akkin, C. Magnain, R. Wang, J. Dubb, W.J. Kostis, M.A. Yaseen, A. Cramer, S. Sakadžić, D. Boas, Polarization sensitive optical coherence microscopy for brain imaging, Optics letters 41(10) (2016) 2213-2216.
[114] C.J. Liu, K.E. Williams, H.T. Orr, T. Akkin, Visualizing and mapping the cerebellum with serial optical coherence scanner, Neurophotonics 4(1) (2016) 011006.
[115] D.A. Boas, H. Wang, C. Magnain, B. Fischl, Polarization-sensitive optical coherence tomography of the human brain connectome, SPIE Newsroom 10(2.1201701) (2017) 006834.
[116] E.M. Lankenau, M. Krug, S. Oelckers, N. Schrage, T. Just, G. Hüttmann, iOCT with surgical microscopes: a new imaging during microsurgery, Advanced Optical Technologies 2(3) (2013) 233-239.
[117] M. Finke, S. Kantelhardt, A. Schlaefer, R. Bruder, E. Lankenau, A. Giese, A. Schweikard, Automatic scanning of large tissue areas in neurosurgery using optical coherence tomography, The International Journal of Medical Robotics and Computer Assisted Surgery 8(3) (2012) 327-336.
[118] B.M. Greenberg, E. Frohman, Optical coherence tomography as a potential readout in clinical trials, Therapeutic advances in neurological disorders 3(3) (2010) 153-160.
[119] S. Svetozarskiy, S. Kopishinskaya, Retinal optical coherence tomography in neurodegenerative diseases, Современные технологии в медицине 7(1 (eng)) (2015).
[120] A. Grzybowski, P. Barboni, OCT in Central Nervous System Diseases, Springer2016.
[121] C.A. Puliafito, M.R. Hee, C.P. Lin, E. Reichel, J.S. Schuman, J.S. Duker, J.A. Izatt, E.A. Swanson, J.G. Fujimoto, Imaging of macular diseases with optical coherence tomography, Ophthalmology 102(2) (1995) 217-229.
[122] E. Lankenau, D. Klinger, C. Winter, A. Malik, H.H. Müller, S. Oelckers, H.-W. Pau, T. Just, G. Hüttmann, Combining optical coherence tomography (OCT) with an operating microscope, Advances in medical engineering, Springer2007, pp. 343-348.
[123] S. Chen, Q. Liu, X. Shu, B. Soetikno, S. Tong, H.F. Zhang, Imaging hemodynamic response after ischemic stroke in mouse cortex using visible-light optical coherence tomography, Biomedical optics express 7(9) (2016) 3377-3389.
[124] X. Shu, Q. Liu, S. Chen, S. Tong, H.F. Zhang, Monitoring acute stroke in mouse model using visible-light optical coherence tomography, Optical Tomography and Spectroscopy, Optical Society of America, 2018, p. JTu3A. 59.
[125] J.-F. Zhang, S. Wiseman, M.C. Valdés-Hernández, F.N. Doubal, B. Dhillon, Y.-C. Wu, J.M. Wardlaw, The Application of Optical Coherence Tomography Angiography in Cerebral Small Vessel Disease, Ischemic Stroke, and Dementia: A Systematic Review, Frontiers in neurology 11 (2020).
[126] Z. Ding, H. Ren, Y. Zhao, J.S. Nelson, Z. Chen, High-resolution optical coherence tomography over a large depth range with an axicon lens, Optics letters 27(4) (2002) 243-245.
[127] R.F. Spaide, J.G. Fujimoto, N.K. Waheed, Optical coherence tomography angiography, Retina (Philadelphia, Pa.) 35(11) (2015) 2161.
[128] J.H. McLeod, The axicon: a new type of optical element, JOSA 44(8) (1954) 592-597.

[129] Z. Bouchal, J. Wagner, M. Chlup, Self-reconstruction of a distorted nondiffracting beam, Optics Communications 151(4-6) (1998) 207-211.
[130] V. Garcés-Chávez, D. McGloin, H. Melville, W. Sibbett, K. Dholakia, Simultaneous micromanipulation in multiple planes using a self-reconstructing light beam, Nature 419(6903) (2002) 145-147.
[131] F.O. Fahrbach, P. Simon, A. Rohrbach, Microscopy with self-reconstructing beams, Nature photonics 4(11) (2010) 780-785.
[132] C. Blatter, B. Grajciar, C.M. Eigenwillig, W. Wieser, B.R. Biedermann, R. Huber, R.A. Leitgeb, High-speed functional OCT with self-reconstructive bessel illumination at 1300nm, European Conference on Biomedical Optics, Optical Society of America, 2011, p. 809104.
[133] K.-S. Lee, J.P. Rolland, Bessel beam spectral-domain high-resolution optical coherence tomography with micro-optic axicon providing extended focusing range, Optics letters 33(15) (2008) 1696-1698.
[134] A. Curatolo, P.R. Munro, D. Lorenser, P. Sreekumar, C.C. Singe, B.F. Kennedy, D.D. Sampson, Quantifying the influence of Bessel beams on image quality in optical coherence tomography, Scientific reports 6 (2016) 23483.
[135] Y. Chen, J.T. Liu, Characterizing the beam steering and distortion of Gaussian and Bessel beams focused in tissues with microscopic heterogeneities, Biomedical optics express 6(4) (2015) 1318-1330.
[136] G.J. Lu, L.-d. Chou, D. Malounda, A.K. Patel, D.S. Welsbie, D.L. Chao, T. Ramalingam, M.G. Shapiro, Biomolecular contrast agents for optical coherence tomography, bioRxiv (2019) 595157.
[137] P. Si, D. Sen, R. Dutta, S. Yousefi, R. Dalal, Y. Winetraub, O. Liba, A. de la Zerda, Optical coherence tomography of lymphatic vessel endothelial hyaluronan receptors in vivo, Optical Coherence Tomography and Coherence Domain Optical Methods in Biomedicine XXII, International Society for Optics and Photonics, 2018, p. 1048326.
[138] O. Liba, E.D. SoRelle, D. Sen, A. de La Zerda, Contrast-enhanced optical coherence tomography with picomolar sensitivity for functional in vivo imaging, Scientific reports 6(1) (2016) 1-12.
[139] P. Si, S. Shevidi, E. Yuan, K. Yuan, Z. Lautman, S.S. Jeffrey, G.W. Sledge, A. de la Zerda, Gold nanobipyramds as optical coherence tomography contrast agents in the second near infrared window for multiplexing study of tumor lymphatic flows (Conference Presentation), Optical Coherence Tomography and Coherence Domain Optical Methods in Biomedicine XXIV, International Society for Optics and Photonics, 2020, p. 1122829.
[140] B.R. Smith, S.S. Gambhir, Nanomaterials for in vivo imaging, Chemical reviews 117(3) (2017) 901-986.
[141] P. Si, E. Yuan, O. Liba, Y. Winetraub, S. Yousefi, E.D. SoRelle, D.W. Yecies, R. Dutta, A. de la Zerda, Gold nanoprisms as optical coherence tomography contrast agents in the second near-infrared window for enhanced angiography in live animals, ACS nano 12(12) (2018) 11986-11994.
[142] P. Si, D. Sen, R. Dutta, S. Yousefi, R. Dalal, Y. Winetraub, O. Liba, A. de la Zerda, In vivo molecular optical coherence tomography of lymphatic vessel endothelial Hyaluronan receptors, Scientific reports 7(1) (2017) 1-11.
[143] V.P. Nguyen, W. Qian, Y. Li, B. Liu, M. Aaberg, J. Henry, W. Zhang, X. Wang, Y.M. Paulus, Chain-like gold nanoparticle clusters for multimodal photoacoustic microscopy and optical coherence tomography enhanced molecular imaging, Nature Communications 12(1) (2021) 1-14.
[144] E.D. SoRelle, D.W. Yecies, O. Liba, F.C. Bennett, C.M. Graef, R. Dutta, S. Mitra, L.-M. Joubert, S. Cheshier, G.A. Grant, Spatiotemporal tracking of brain-tumor-associated myeloid cells in vivo through optical coherence tomography with plasmonic labeling and speckle modulation, ACS nano 13(7) (2019) 7985-7995.
[145] R. John, R. Rezaeipoor, S.G. Adie, E.J. Chaney, A.L. Oldenburg, M. Marjanovic, J.P. Haldar, B.P. Sutton, S.A. Boppart, In vivo magnetomotive optical molecular imaging using targeted magnetic nanoprobes, Proceedings of the National Academy of Sciences 107(18) (2010) 8085-8090.
[146] Y. Jia, G. Liu, A.Y. Gordon, S.S. Gao, A.D. Pechauer, J. Stoddard, T.J. McGill, A. Jayagopal, D. Huang, Spectral fractionation detection of gold nanorod contrast agents using optical coherence tomography, Optics express 23(4) (2015) 4212-4225.
[147] A. Nahas, M. Varna, E. Fort, A.C. Boccara, Detection of plasmonic nanoparticles with full field-OCT: optical and photothermal detection, Biomedical optics express 5(10) (2014) 3541-3546.
[148] R. Dutta, O. Liba, E.D. SoRelle, Y. Winetraub, V.C. Ramani, S.S. Jeffrey, G.W. Sledge, A. de la Zerda, Real-time detection of circulating tumor cells in living animals using functionalized large gold nanorods, Nano letters 19(4) (2019) 2334-2342.
[149] A.L. Oldenburg, R.K. Chhetri, J.M. Cooper, W.-C. Wu, M.A. Troester, J.B. Tracy, Motility-, autocorrelation-, and polarization-sensitive optical coherence tomography discriminates cells and gold nanorods within 3D tissue cultures, Optics letters 38(15) (2013) 2923-2926.
[150] A. Wax, C. Yang, R.R. Dasari, M.S. Feld, Path-length-resolved dynamic light scattering: modeling the transition from single to diffusive scattering, Applied Optics 40(24) (2001) 4222-4227.
[151] M.C. Skala, M.J. Crow, A. Wax, J.A. Izatt, Photothermal optical coherence tomography of epidermal growth factor receptor in live cells using immunotargeted gold nanospheres, Nano letters 8(10) (2008) 3461-3467.
[152] T.S. Troutman, J.K. Barton, M. Romanowski, Optical coherence tomography with plasmon resonant nanorods of gold, Optics letters 32(11) (2007) 1438-1440.

[153] C. Yang, Molecular Contrast Optical Coherence Tomography: A Review¶, Photochemistry and Photobiology 81(2) (2005) 215-237.
[154] S.A. Boppart, A.L. Oldenburg, C. Xu, D.L. Marks, Optical probes and techniques for molecular contrast enhancement in coherence imaging, Journal of biomedical optics 10(4) (2005) 041208.
[155] N.N. Boustany, S.A. Boppart, V. Backman, Microscopic imaging and spectroscopy with scattered light, Annual review of biomedical engineering 12 (2010) 285-314.
[156] S. P Mattison, W. Kim, J. Park, B. E Applegate, Molecular imaging in optical coherence tomography, Current Molecular Imaging (Discontinued) 3(2) (2014) 88-105.
[157] J. Kim, W. Brown, J.R. Maher, H. Levinson, A. Wax, Functional optical coherence tomography: principles and progress, Physics in Medicine & Biology 60(10) (2015) R211.
[158] E.D. SoRelle, O. Liba, Z. Hussain, M. Gambhir, A. de la Zerda, Biofunctionalization of large gold nanorods realizes ultrahigh-sensitivity optical imaging agents, Langmuir 31(45) (2015) 12339-12347.
[159] E.D. SoRelle, D.W. Yecies, O. Liba, C.F. Bennett, C.-M. Graef, R. Dutta, S.S. Mitra, L.-M. Joubert, S.H. Cheshier, G.A. Grant, Wide-field dynamic monitoring of immune cell trafficking in murine models of glioblastoma, bioRxiv (2017) 220954.
[160] E.D. SoRelle, O. Liba, D. Sen, A. de la Zerda, Spectral contrast-enhanced optical coherence tomography for improved detection of tumor microvasculature and functional imaging of lymphatic drainage, Dynamics and Fluctuations in Biomedical Photonics XIV, International Society for Optics and Photonics, 2017, p. 100630T.
[161] J. Liu, N. Ding, Y. Yu, X. Yuan, S. Luo, J. Luan, Y. Zhao, Y. Wang, Z. Ma, Optimized depth-resolved estimation to measure optical attenuation coefficients from optical coherence tomography and its application in cerebral damage determination, Journal of biomedical optics 24(3) (2019) 035002.
[162] C.W. Merkle, J. Zhu, M.T. Bernucci, V.J. Srinivasan, Dynamic Contrast Optical Coherence Tomography reveals laminar microvascular hemodynamics in the mouse neocortex in vivo, Neuroimage 202 (2019) 116067.
[163] J. You, C. Du, N.D. Volkow, Y. Pan, Optical coherence Doppler tomography for quantitative cerebral blood flow imaging, Biomedical optics express 5(9) (2014) 3217-3230.
[164] C.W. Merkle, V.J. Srinivasan, Laminar microvascular transit time distribution in the mouse somatosensory cortex revealed by Dynamic Contrast Optical Coherence Tomography, Neuroimage 125 (2016) 350-362.
[165] Y. Pan, J. You, N.D. Volkow, K. Park, C. Du, Ultrasensitive detection of 3D cerebral microvascular network dynamics in vivo, Neuroimage 103 (2014) 492-501.
[166] J. Zhu, M.T. Bernucci, C.W. Merkle, V.J. Srinivasan, Visibility of microvessels in Optical Coherence Tomography Angiography depends on angular orientation, Journal of biophotonics 13(10) (2020) e202000090.
[167] M.T. Bernucci, C.W. Merkle, V.J. Srinivasan, Investigation of artifacts in retinal and choroidal OCT angiography with a contrast agent, Biomedical optics express 9(3) (2018) 1020-1040.
[168] X. Wen, V.V. Tuchin, Q. Luo, D. Zhu, Controling the scattering of intralipid by using optical clearing agents, Physics in Medicine & Biology 54(22) (2009) 6917.
[169] A. Dubois, K. Grieve, G. Moneron, R. Lecaque, L. Vabre, C. Boccara, Ultrahigh-resolution full-field optical coherence tomography, Applied optics 43(14) (2004) 2874-2883.
[170] R. Leitgeb, M. Villiger, A. Bachmann, L. Steinmann, T. Lasser, Extended focus depth for Fourier domain optical coherence microscopy, Optics letters 31(16) (2006) 2450-2452.
[171] A.F. Fercher, W. Drexler, C.K. Hitzenberger, T. Lasser, Optical coherence tomography-principles and applications, Reports on progress in physics 66(2) (2003) 239.
[172] B. Bouma, Handbook of optical coherence tomography, CRC Press2001.
[173] P.H. Tomlins, R.K. Wang, Theory, developments and applications of optical coherence tomography, Journal of Physics D: Applied Physics 38(15) (2005) 2519.
[174] V.J. Srinivasan, D.N. Atochin, H. Radhakrishnan, J.Y. Jiang, S. Ruvinskaya, W. Wu, S. Barry, A.E. Cable, C. Ayata, P.L. Huang, D.A. Boas, Optical coherence tomography for the quantitative study of cerebrovascular physiology, J Cereb Blood Flow Metab 31(6) (2011) 1339-45.
[175] M.E. Brezinski, Optical coherence tomography: principles and applications, Elsevier2006.
[176] M. Born, E. Wolf, Principles of optics: electromagnetic theory of propagation, interference and diffraction of light, Elsevier2013.
[177] M. Wojtkowski, High-speed optical coherence tomography: basics and applications, Applied optics 49(16) (2010) D30-D61.
[178] A.F. Fercher, C.K. Hitzenberger, G. Kamp, S.Y. El-Zaiat, Measurement of intraocular distances by backscattering spectral interferometry, Optics communications 117(1-2) (1995) 43-48.
[179] T.E. De Carlo, A. Romano, N.K. Waheed, J.S. Duker, A review of optical coherence tomography angiography (OCTA), International journal of retina and vitreous 1(1) (2015) 5.
[180] Y. Jia, S.T. Bailey, T.S. Hwang, S.M. McClintic, S.S. Gao, M.E. Pennesi, C.J. Flaxel, A.K. Lauer, D.J. Wilson, J. Hornegger, Quantitative optical coherence tomography angiography of vascular abnormalities in the living human eye, Proceedings of the National Academy of Sciences 112(18) (2015) E2395-E2402.

[181] J.K. Barton, S. Stromski, Flow measurement without phase information in optical coherence tomography images, Optics express 13(14) (2005) 5234-5239.
[182] Y. Jia, O. Tan, J. Tokayer, B. Potsaid, Y. Wang, J.J. Liu, M.F. Kraus, H. Subhash, J.G. Fujimoto, J. Hornegger, Split-spectrum amplitude-decorrelation angiography with optical coherence tomography, Optics express 20(4) (2012) 4710-4725.
[183] C. Blatter, B. Grajciar, T. Schmoll, R.A. Leitgeb, T. Klein, W. Wieser, R.J. André, R. Huber, Ultrahigh-speed non-invasive widefield angiography, Journal of biomedical optics 17(7) (2012) 070505.
[184] A. Mariampillai, B.A. Standish, E.H. Moriyama, M. Khurana, N.R. Munce, M.K. Leung, J. Jiang, A. Cable, B.C. Wilson, I.A. Vitkin, Speckle variance detection of microvasculature using swept-source optical coherence tomography, Optics letters 33(13) (2008) 1530-1532.
[185] R. Motaghiannezam, S. Fraser, Logarithmic intensity and speckle-based motion contrast methods for human retinal vasculature visualization using swept source optical coherence tomography, Biomedical optics express 3(3) (2012) 503-521.
[186] D.Y. K